IDŐJÁRÁS

QUARTERLY JOURNAL OF THE HUNGAROMET
HUNGARIAN METEOROLOGICAL SERVICE

CONTENTS

VOL. 130 * NO. 3 * JULY – SEPTEMBER 2026

IDŐJÁRÁS

Quarterly Journal of the HungaroMet Hungarian Meteorological Service

Editorial Office: Kitaibel P.u. 1, H-1024 Budapest, Hungary
P.O. Box 38, H-1525 Budapest, Hungary
E-mail: journal.idojaras@met.hu

Indexed and abstracted in Science Citation Index Expanded™ and Journal Citation Reports/Science Edition
Covered in the abstract and citation database SCOPUS®
Included in EBSCO's database

Subscription by mail:
IDŐJÁRÁS, P.O. Box 38, H-1525 Budapest, Hungary
E-mail: journal.idojaras@met.hu

DOI:10.28974/idojaras.2026.3.1

IDŐJÁRÁS

Quarterly Journal of the HungaroMet Hungarian Meteorological Service
Vol. 130, No. 3, July – September, 2026, pp. 225–243

Case studies of micro-meteorological wind simulations and turbulence analysis in Hong Kong during severe tropical storm Wutip in June 2025

Ka Wai Lo, **Kai Kwong Lai**, and **Pak Wai Chan***

Hong Kong Observatory,
134A Nathan Road, Kowloon, Hong Kong, China

**Corresponding author E-mail: pwchan@hko.gov.hk*

(Manuscript received in final form on January 8, 2026)

Abstract— Micrometeorological studies of a bridge and the urban area of Hong Kong under south to southwesterly winds associated with tropical cyclone Wutip in June 2025 were conducted using computational fluid dynamic simulation driven by a mesoscale model. For mean winds, such as 1-min or 10-min averages (as in the application to road traffic management on a bridge), the use of mesoscale meteorological models alone may be sufficient to capture the general wind trend, since the RMSEs of the mean wind speeds were comparable and mostly in the range of 1–5 m s^{-1}. However, if fluctuations in winds are considered and turbulence intensity is a concern for operation (such as the operation of drones in low-altitude economic activities), the coupling of mesoscale meteorological models with computational fluid dynamics models must be considered. However, the measured turbulence intensity could be rather high (40–50% for turbulence intensity), which may not be achieved with mesoscale coupled computational fluid dynamic models. Numerous issues remain to be resolved for this type of micro-meteorological studies, especially for studies and applications in urban meteorology. Future directions for these studies are also discussed.

Key-words: computational fluid dynamics (CFD), large eddy simulation (LES), turbulence intensity, tropical cyclone

1. *Introduction*

Microscale meteorological services that cover limited areas within a city have great application value. For instance, predicting wind speed trends and turbulence across sections of a long bridge is crucial for determining the cessation and resumption of road traffic (*Cai et al.*, 2015), particularly during tropical cyclones. Wind and turbulence measurements and forecasting in urban areas would be useful in several aspects, such as the comfort of pedestrians on the road (*Blocken* and *Carmeliet*, 2004) and the operation of drones for logistical purposes in low-altitude economy (LAE) (*Gianfelice et al.*, 2022).

Microclimatological monitoring (*Lefevre et al.*, 2024; *Liu et al*., 2022; *Oke*, 2006), such as the setup of ultrasonic anemometers on bridges and lampposts (so-called smart lampposts) on roadsides, is becoming increasingly common. More experiments are being attempted to forecast microclimates, especially wind trends and turbulence metrics, such as turbulence intensity (the standard deviation of the wind speed divided by the mean wind speed).

Simulations of wind speed trends were previously performed by *Lo et al.* (2024a) for two tropical cyclones at a bridge in Hong Kong. A case study involving the simulation of an urban area in a tropical cyclone situation was also performed by *Lo et al.* (2024b). The present study is a continuation of the previous study, that focused on the severe tropical storm tip affecting Hong Kong from 14 to 15 June 2025. The Tseung Kwan O (TKO) bridge on the eastern side of the territory was considered. Simultaneously, a study was conducted for the downtown area of Hong Kong, namely, the Tsim Sha Tsui (TST) area. This study is novel in several ways.

1. In previous tropical cyclone studies, the winds were mainly northerlies. This study examined southerly winds induced by Wutip to assess the terrain and building impacts on microclimates across varying prevailing wind directions.

2. Following the previous study, *Lo et al.* (2024b), more microclimate stations were set up in the TST. Weather stations operate in various parts of the TST and their measurements are compared with a high-resolution numerical weather prediction (NWP) model coupled with a computational fluid dynamics (CFD) model.

3. Apart from the 1-min and 10-min mean winds in the previous studies, *Lo et al.* (2024a) and *Lo et al.* (2024b), the turbulence intensity was also considered. Unfortunately, the high-frequency wind data (e.g. per-second measurements) required to calculate the eddy dissipation rate (EDR) are unavailable from the TKO bridge and TST microclimate stations, precluding a direct comparison with sub-grid-scale EDR outputs from the NWP-CFD coupled model.

2. Materials and methods

2.1. Microclimate stations

A re-cap of the anemometer setup on the TKO bridge is shown in the upper panel of *Fig.1*. Eight anemometers were present in total. CB1 and CB2 were positioned at the bridge deck level. The other six anemometers were installed on two arc-shaped structures, with the highest points at CB5 and CB6, approximately 60 m above sea level.

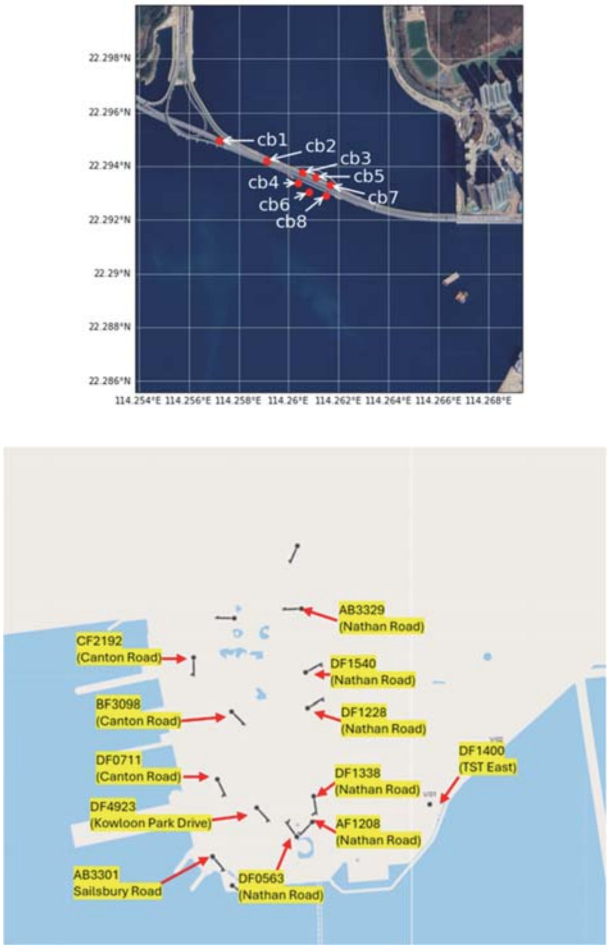

Fig.1. Location of the eight anemometers on the Tseung Kwan O bridge (upper panel) and location of the microclimate stations over the Tsim Sha Tsui area (lower panel).

The setup of the microclimate stations in the TST area is shown in the lower panel of *Fig.1*. Most of the stations were set up along the major roads in a general north-south orientation in the area, namely, Nathan Road and Canton Road. A couple of anemometers have better exposure to the seaside, namely, AB3301 near Star Pier and DF1400 on the coast of the TST East area.

2.2. Severe tropical storm Wutip

Surface isobaric charts for the mornings of June 14 and 15, 2025 are shown in the upper and lower panels of *Fig.2*, respectively. Wutip was initially located west of the Leizhou Peninsula in western Guangdong, China, over Beibu Wan. It then moved northeastward, crossing the southern part of China, and gradually weakened over land. The following morning, it was located approximately 300 km north of Hong Kong. Because of its circulation, southerly winds prevailed over Hong Kong on June 14, 2025. The wind direction gradually veered southwest. Under southerly wind situations, the TKO bridge and TST area are downstream of the mountains in Hong Kong. The terrain of the latter island may have induced turbulence in the two areas under investigation. Apart from the mean winds, the turbulence intensity was also studied in the present paper.

2.3. Numerical model setup

The mesoscale simulation employed the Regional Atmospheric Modelling System (RAMS v6.3) configured with six nested domains of progressively finer resolutions: 25 km, 5 km, 1 km, 200 m, 40 m, and 40 m. The fifth and sixth domains (both at 40 m resolution) were centered over the TKO and TST regions, respectively, to provide high-resolution wind fields for the targeted areas. These innermost domains also supplied the initial and boundary conditions for subsequent CFD simulations. The vertical grid started from a size of 75 m, with a stretching ratio of 1.08 applied to successive layers, and the maximum vertical spacing was capped at 2000 m. The turbulence closure for the innermost four domains utilized the Deardorff parameterization scheme (*Deardorff,* 1980).

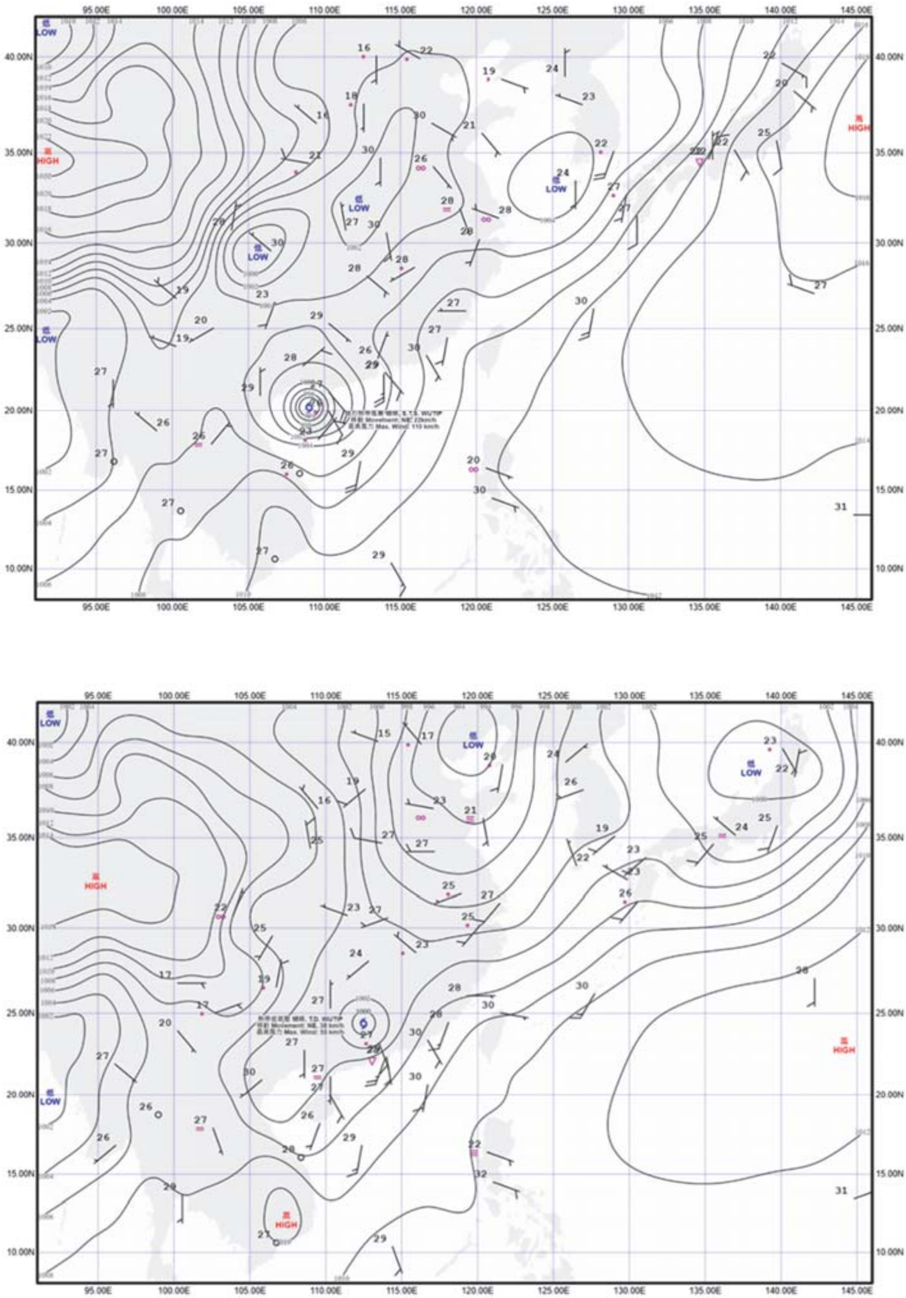

Fig.2. Surface isobaric charts at 8:00 a.m. on June 14, 2025 (upper panel) and at 8:00 a.m. on June 15, 2025 (lower panel). The local time has been followed (UTC+8).

Parallelized large-eddy simulation model PALM was used as the CFD software for this study (*Maronga et al*., 2015, 2020; *Raasch* and *Schröter*, 2001). It is a parallelized large-eddy simulation (LES) model which solves filtered, nonhydrostatic, and incompressible Navier–Stokes equations under the Boussinesq approximation. PALM explicitly resolves energy-containing eddies while modeling subgrid-scale turbulence via a 1.5-order closure scheme based on the Deardorff parameterization (*Deardorff*, 1980). For the numerical schemes, a fifth-order upwind momentum advection scheme (*Wicker* and *Skamarock*, 2002) together with a third-order Runge-Kutta time-stepping method (*Williamson*, 1980) were used. The spatial resolution was set to 2 m horizontally, while vertically, a 2 m base grid was applied up to 50 m altitude, after which a stretching ratio of 1.08 was imposed, capping the maximum vertical grid spacing at 12 m. Synthetic turbulence was generated at the inflow boundaries (*Kim et al*., 2013; *Xie* and *Castro*, 2008). The coupling between RAMS and PALM was performed using a dynamic file generated from the RAMS simulation data, which supplied the initial and boundary conditions required for the PALM simulation.

3. Results

3.1. Results for the TKO bridge

Numerical simulations generally capture trends in wind speed and wind direction changes at bridges. A snapshot of the wind distribution over the bridge is shown in the upper panel of *Fig.3*. The simulation was initialized at 12 UTC on June 14, 2025 and ran for 18 h till 06 UTC on June 15, 2025. A snapshot of the simulation results around the time of observation is shown in the lower panel of *Fig.3*. Strong south-to southwesterly winds (blue wind barbs in the lower panel of *Fig.3*.) prevailed in the bridge region. Gale force winds (red wind barbs) were simulated at isolated positions and were consistent with actual observations, particularly at the location of the two arc-shaped structures.

Fig.4. provides a general overview of the wind simulation results from the RAMS at a horizontal resolution of 40 m. The wind pattern at a height of approximately 60 m above the local terrain is shown in the upper panel of *Fig.4*. A gap prevails in the mountains of Hong Kong upstream of the island area. This gap flow results in a narrow south to southwesterly jet just over the bridge. Simultaneously, because of the terrain of Hong Kong Island, moderate to severe turbulence occurs downstream of such terrain (colored yellow to red in the lower panel of *Fig.4*, in the region of 0.3 to 0.5 $m^{2/3}s^{-1}$). This higher turbulence area only covers the sea channel and the TKO bridge is free of stronger turbulence.

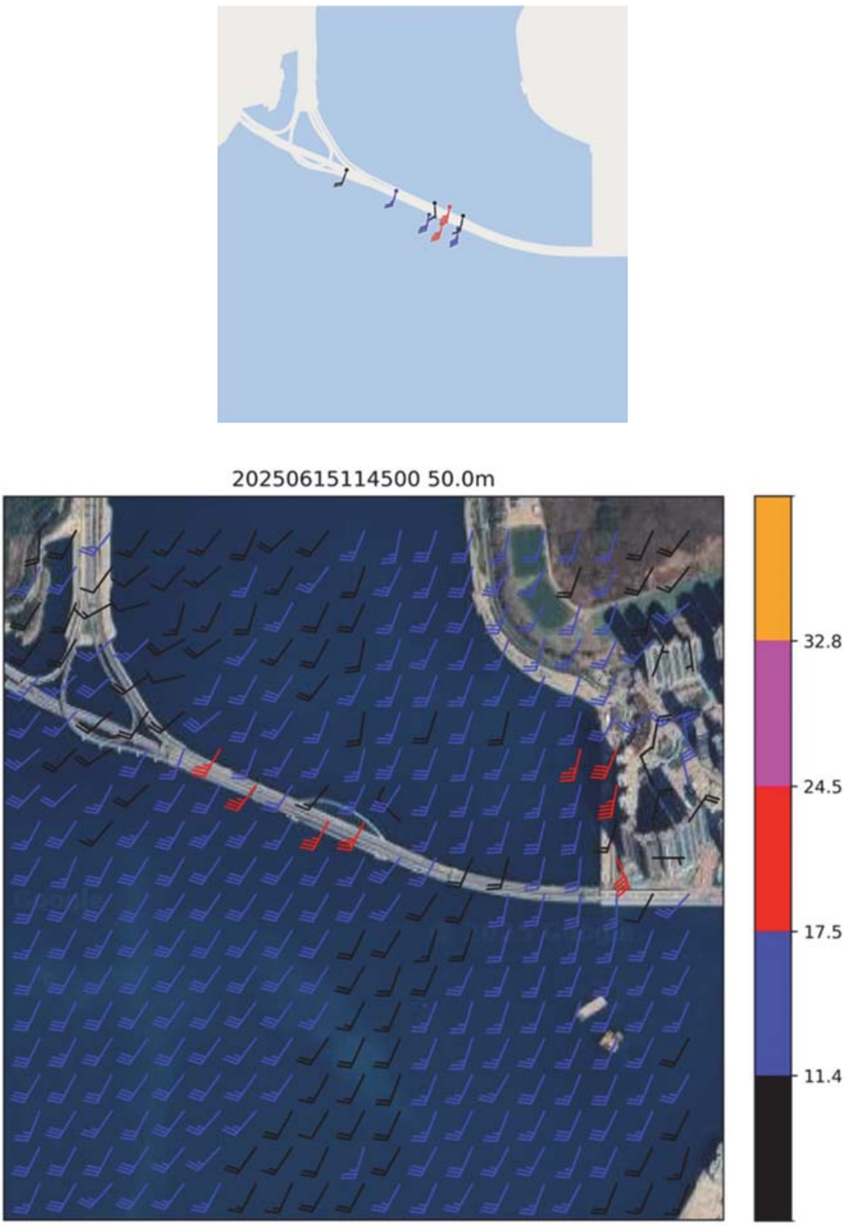

Fig. 3. Wind distributions over the TKO Bridge at 11:00 a.m. on June 15, 2025 (upper panel) and the simulated wind distribution by the PALM at 11:45 a.m. on the same day (lower panel). The local time has been followed (UTC+8).

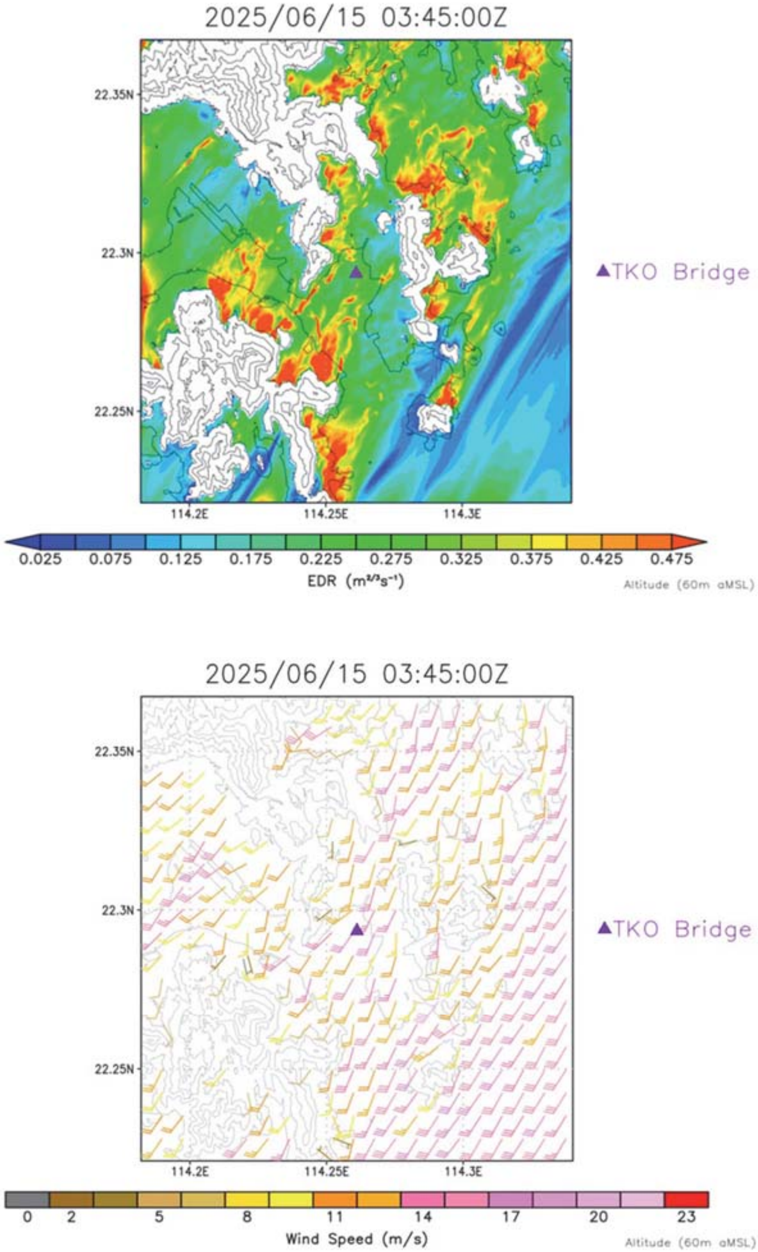

Fig.4. Winds (upper panel) and EDR (lower panel) simulation from RAMS at a height of around 60 m above local terrain at 11:45am on June 15, 2025, in local time.

The time series of the actual wind observations from the bridge are shown in *Fig.5*, where the upper panel shows the 1-min mean wind speed and the lower panel shows the 10-min mean wind direction. The simulation results were overlaid on them, with blue showing the RAMs results (at 40 m horizontal resolution) and red showing the PALM results. The following features were observed: (1) the wind speed and wind direction changes from the actual observations were generally well captured by both simulations for most anemometers, apart from isolated ones, such as CB3 and CB7; (2) the overall trend of RAMS and PALM simulation results were similar, and as such performing simulation at higher spatial resolution did not gain value in capturing finer changes in the time series of the observed wind speed and wind direction; (3) nonetheless, PALM results showed strong fluctuations, with magnitudes more comparable with the actual observations, as compared with the RAMS simulation results, and as such CFD simulation at higher spatial resolution had the value of providing more realistic fluctuations of the wind speed and wind direction, at least for 1-min averages.

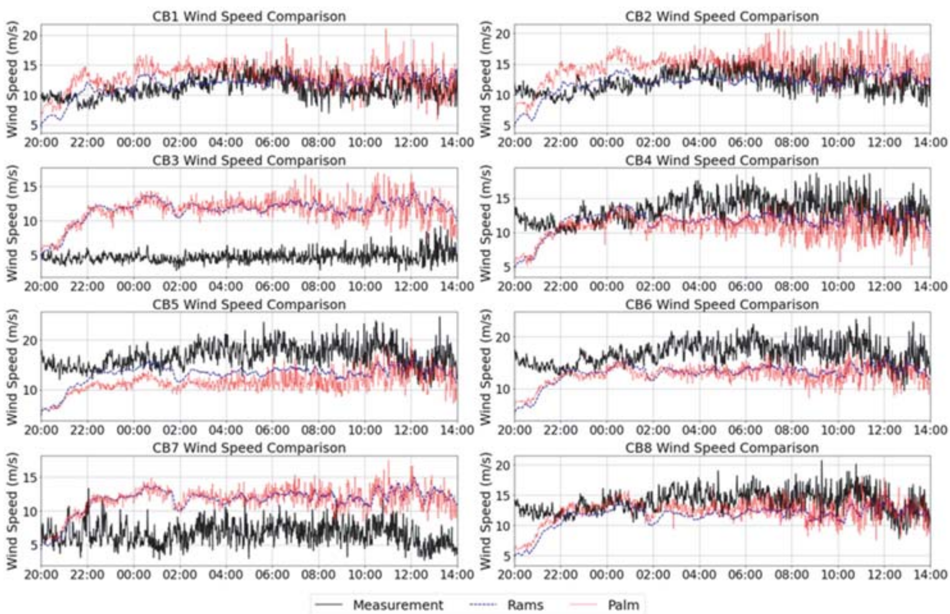

Fig. 5. Time series of the 1-min mean wind (upper panel) and 10-min wind direction (lower panel) at the eight anemometers on the TKO bridge from measurement, RAMS simulation, and PALM simulation.

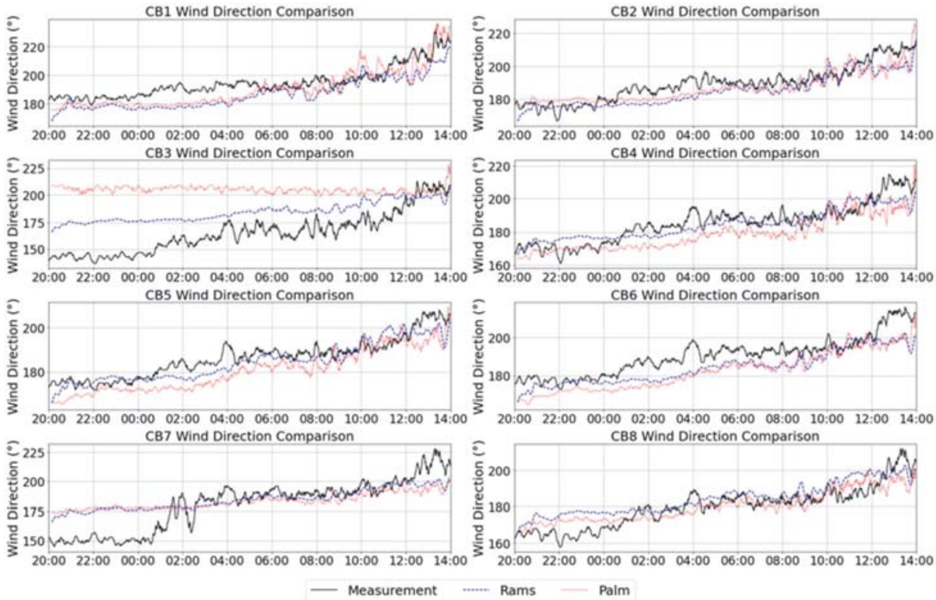

Fig.5. Continued

The quantitative comparison results are presented in *Table 1*. The period under consideration did not cover the first two hours of the simulation, allowing for spin-up of the models. The model simulations were compared directly with the anemometer measurements, and the root-mean-square errors (RMSEs) were calculated. From the perspective of RMSEs, the use of CFD simulation did not improve the forecasting results, namely, the RMSEs of RAMS alone and RAMS-CFD coupling were basically similar. However, as discussed above, RAMS-CFD captured the actual fluctuations in winds and had better application value.

Table 1. RMSE of wind speeds and direction from RAMS and PALM simulation compared to the measurement for eight anemometers over the TKO bridge

	CB1	CB2	CB3	CB4	CB5	CB6	CB7	CB8
RAMS Speed RMSE	2.04	1.85	7.42	2.45	4.04	4.08	5.86	2.80
PALM Speed RMSE	3.00	3.46	7.48	3.29	5.79	4.64	5.86	2.61
RAMS Direction RMSE	9.88	7.00	21.22	6.24	4.57	7.99	13.75	7.15
PALM Direction RMSE	8.12	6.33	41.45	9.61	7.16	9.24	15.09	6.06

As discussed previously, a new feature of the present study is the consideration of the turbulence intensity (TI). TI is calculated as the ratio of the standard deviation of wind speed to the mean wind speed over two-hour rolling window. The time series of the observed and simulated TIs is shown in *Fig. 6*. In general, from the actual observations, Tis showed an increasing trend with time.

Apart from the isolated anemometer (e.g. CB7), the trend was captured much better by the PALM simulation results than by RAMS alone. This is consistent with the previous observation that the RAMS-CFD coupled model captures the magnitude of the wind speed fluctuations, and this is reflected in forecasting the correct magnitude of the observed TIs.

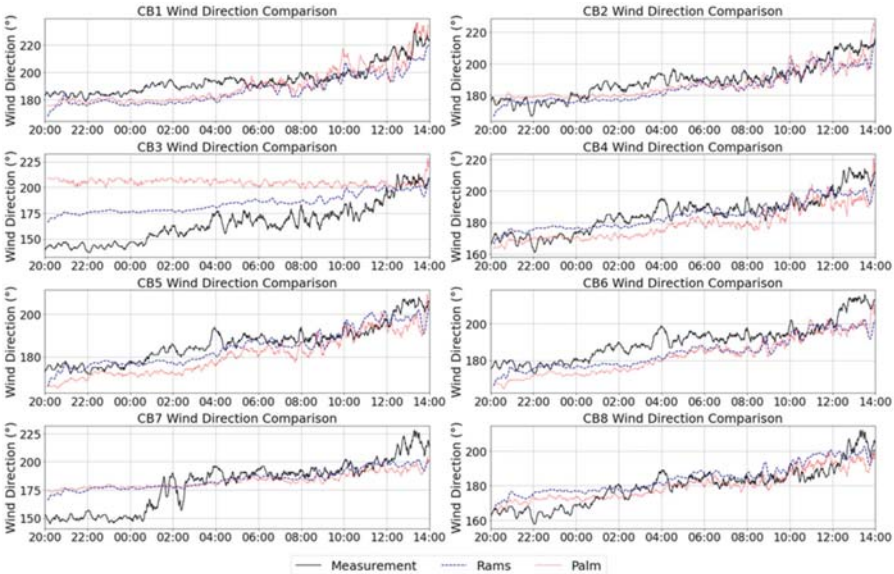

Fig. 6. Time series of turbulent intensity at the eight anemometers on the TKO bridge from measurement, RAMS simulation, and PALM simulation.

3.2. Results for the TST area

The study of the TST area is an urban meteorology issue; that is, with a highly developed area with several buildings, the value of the RAMS-CFD gain compared with the RAMS simulation alone (which considers the terrain and coastline only, without considering the buildings). A snapshot of the observations made by the microclimate station is shown in the upper panel of *Fig.7*. Two notable features exist, namely, southwestely flow at the southwestern corner of the TST area, which is more exposed in that direction toward the harbor, and a cyclonic feature observed at the southern part of Nathan Road, probably due to the interplay between terrain and buildings on the airflow. The corresponding simulation results are presented in the lower panel of *Fig.7*. This was a 15-h simulation as initialized at 12 UTC on June 14, 2025. Both features appeared well in the RAMS-CFD simulation results. In general, the available observations compared favorably with the simulation results, at least for this snapshot.

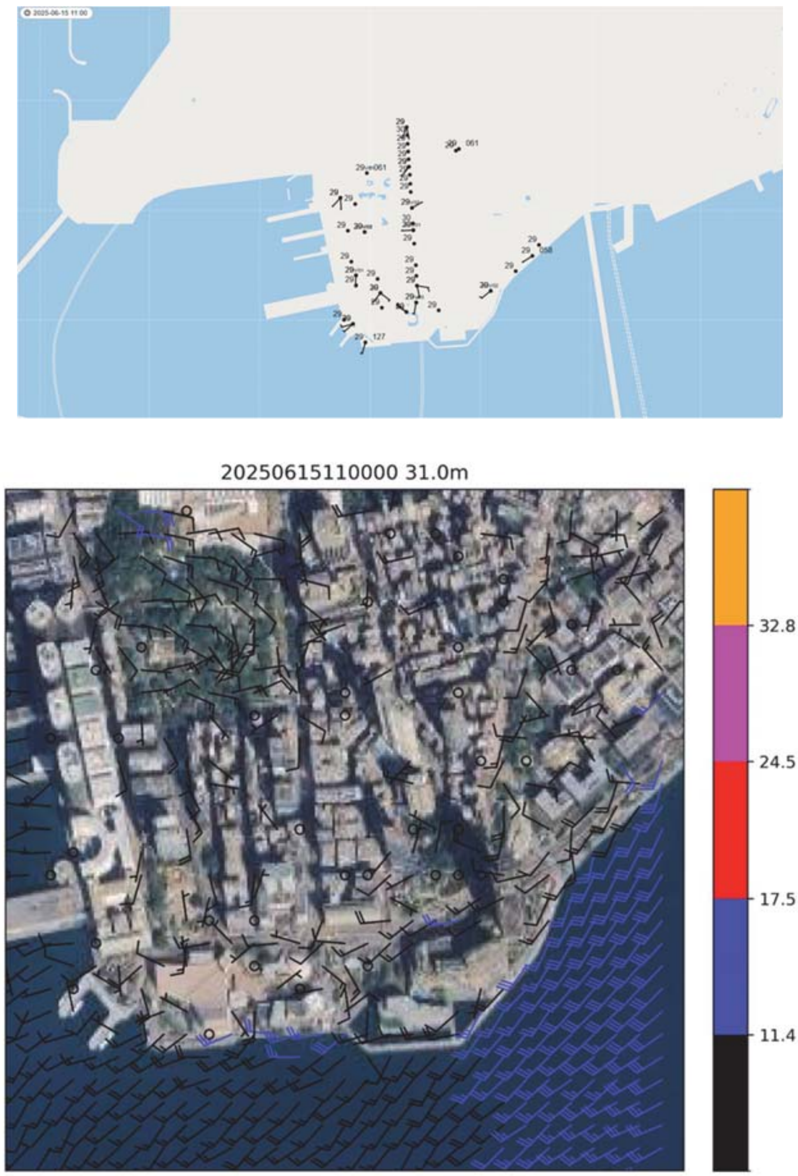

Figure 7 Wind measurement over the Tsim Sha Tsui area at 11:00 a.m. on June 15, 2025 (upper panel) and the simulated wind distribution by the PALM over the Tsim Sha Tsui area at the same time (lower panel). The local time has been followed (UTC+8).

As an indication of the flow pattern in the TST area owing to the terrain, the RAMS simulation results (for the innermost domain with a horizontal resolution of 40 m) are shown in *Fig.8*. The upper panels show the simulated wind near the surface. Owing to blockage by the terrain of Hong Kong Island, the TST area generally has lighter winds compared to, for instance, the more exposed sea area to the west in this southwesterly flow regime. Simultaneously, owing to the terrain effect, higher turbulence occurs in the TST area, as shown in the EDR distribution in the lower panel of *Fig.8*. However, no actual measurements exist to verify the EDR simulation results.

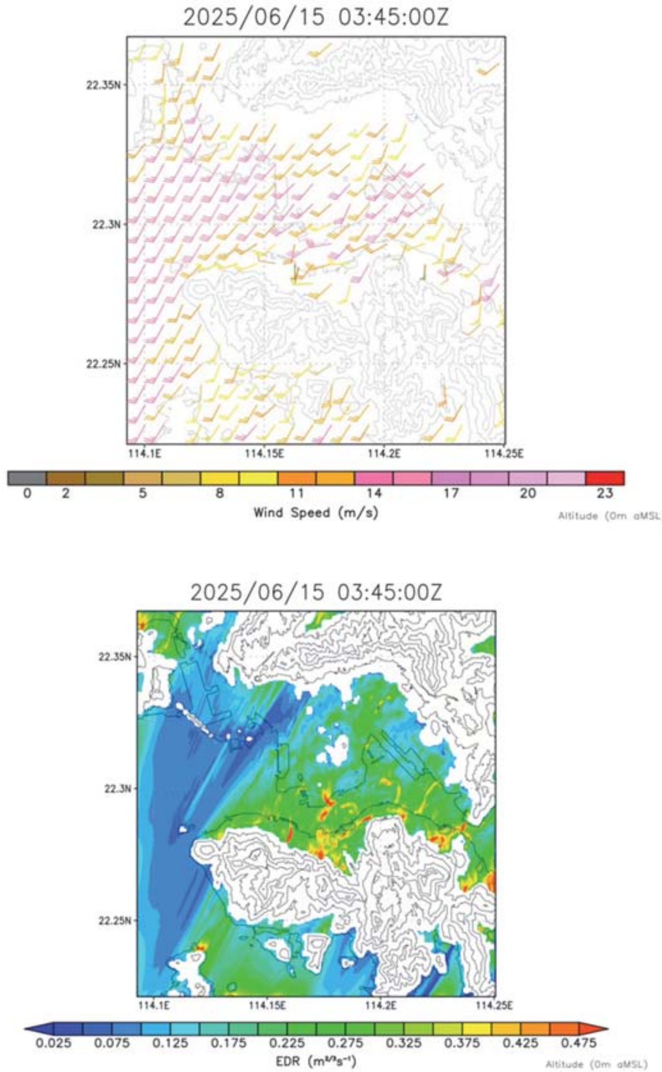

Fig. 8. Wind (upper panel) and EDR (lower panel) simulation from RAMS at 11:45 am on June 15, 2025, in local time

The time series of the observed and simulated (RAMS alone and RAMS-CFD) wind speeds and directions are shown in *Fig.9.* and *Fig.10.*, respectively. Several anemometers are present with blockage effect by the nearby buildings for this south to southwesterly flow regimes, e.g., DF1540, where the measured wind speed remains rather low compared to the RAMS simulation alone, which does not include building effect, and the measured wind direction deviates significantly from the ‘prevailing’ or ‘background’ wind direction of south to southwesterly. Similar features were also observed, for example for DF0563, which showed significant fluctuations in wind direction in the actual measurements.

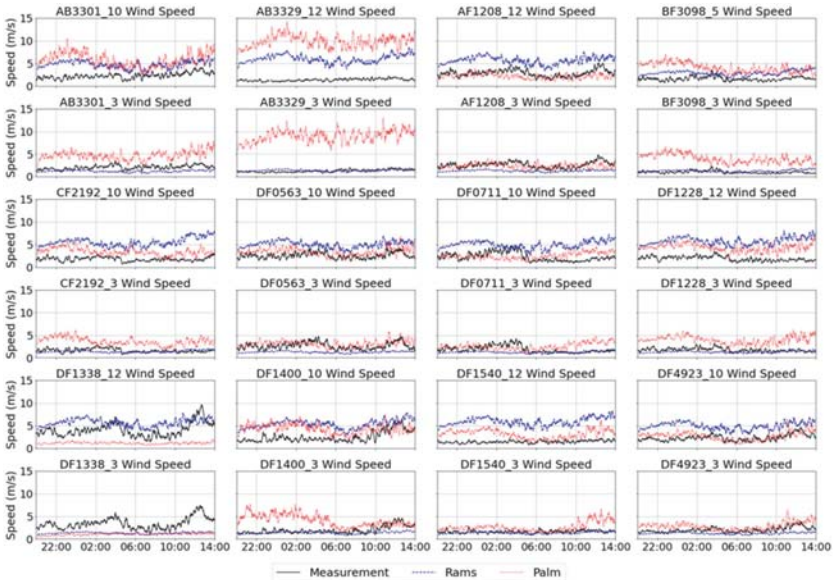

Fig. 9. Time series of the 10-min mean wind speed at the different microclimate stations over Tsim Sha Tsui from measurement, RAMS simulation, and PALM simulation.

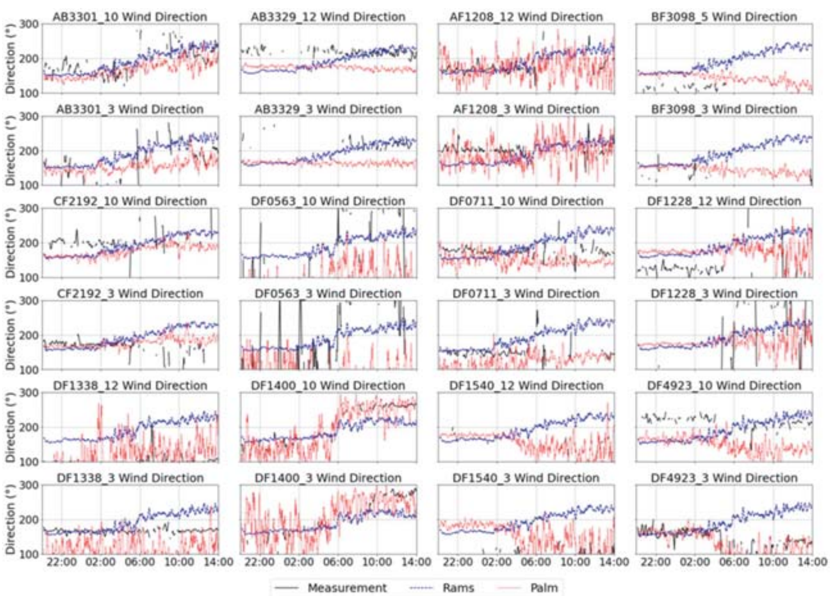

Fig.10. Time series of the 10-min mean wind direction at the different microclimate stations over Tsim Sha Tsui from measurement, RAMS simulation, and PALM simulation.

Moreover, from the perspective of RMSEs for mean winds (the mean 10-min averages are considered because they are used in the actual measurements), the addition of PALM in the simulation does not largely improve the accuracy when compared with the actual observations, as shown in Table 2. For both RAMS alone and RAMS-CFD, the RMSEs for wind speed and wind direction were similar. Sometimes, one set of results is better than the other for individual anemometers; however, in general, considering all stations, it may only be concluded that the RMSEs are comparable.

Table 2. RMSE of wind speeds and direction from RAMS and PALM simulation compared to the measurement for microclimate stations over TST

	AB3301_10	**AB3301_3**	**AB3329_12**	**AB3329_3**	**AF1208_12**	**AF1208_3**
RAMS Speed	2.81	0.97	5.23	0.40	3.54	1.30
PALM Speed	4.18	3.47	9.44	8.42	0.97	1.17
RAMS Direction	37.52	55.37	37.12	44.32	58.14	52.68
PALM Direction	49.93	63.77	46.92	64.91	65.38	57.02

	BF3098_3	**BF3098_5**	**CF2192_10**	**CF2192_3**	**DF0563_10**	**DF0563_3**
RAMS Speed	0.75	1.93	4.61	0.62	3.22	1.32
PALM Speed	2.79	2.25	1.91	2.55	2.05	1.71
RAMS Direction	126.94	136.42	80.68	100.55	99.12	113.57
PALM Direction	92.27	46.64	104.20	101.24	111.53	113.68

	DF0711_10	**DF0711_3**	**DF1228_12**	**DF1228_3**	**DF1338_12**	**DF1338_3**
RAMS Speed	3.90	0.91	4.98	0.58	2.50	2.32
PALM Speed	1.70	1.86	3.51	3.33	3.14	2.57
RAMS Direction	56.22	87.36	107.47	99.76	111.92	50.44
PALM Direction	39.27	57.82	111.19	121.08	60.56	49.71

	DF1400_10	**DF1400_3**	**DF1540_12**	**DF1540_3**	**DF4923_10**	**DF4923_3**
RAMS Speed	2.93	1.02	5.13	0.43	3.25	0.88
PALM Speed	2.08	2.26	1.77	1.65	1.14	1.63
RAMS Direction	44.37	58.32	73.88	116.93	50.30	94.34
PALM Direction	33.43	46.12	67.21	81.13	70.36	34.35

However, the inclusion of CFD has the advantage of capturing fluctuations in the wind, which is reflected in the comparison of the TI, as shown in *Fig.11*. Overall, the simulated TIs from RAMS-CFD compared much better with the actual measurements based on RAMS alone. The maximum achievable TIs from RAMS-CFD were generally higher. Notably, all anemometers show a peak TI in the middle part of the simulation, namely, around 06 Hong Kong time, on June 15, 2025 (which is around 22 UTC, June 14, 2025 with Hong Kong time = UTC + 8 h). This corresponds to the period when the wind direction is generally southerly; as such, significant blockage by the terrain of Hong Kong Island and disturbance of airflow by buildings, prevail. As a result, the terrain-induced turbulence was higher (higher value of standard deviation of the wind speed), and the wind speed just over the TST was rather low (lower value of mean wind speed), leading to a generally higher TI (expressed as the standard deviation of the wind divided by the 10-min mean wind speed). Even with the use of RAMS-PALM, the maximum TI could not be achieved (as high as 40–50%).

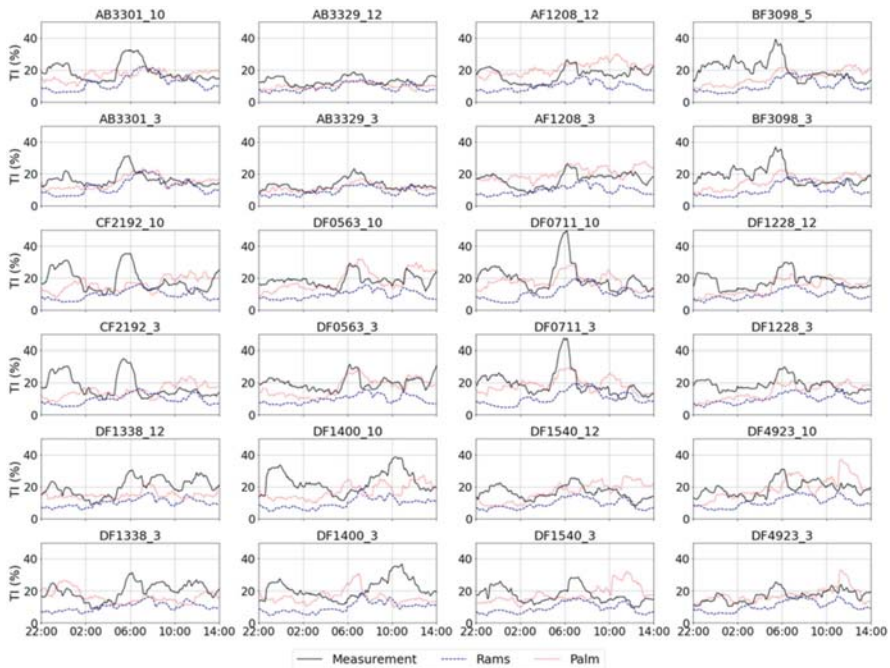

Fig. 11. Time series of turbulent intensity at the microclimate stations over Tsim Sha Tsui from measurement, RAMS simulation, and PALM simulation.

Further tuning and inclusion of more features in the simulation may be necessary to attain this extremely high level of TI. For example, refining the specification of surface roughness could be important, as turbulence can be sensitive to roughness (*Krogstadt*, 1999; *Kadivar*, 2021). Furthermore, the inclusion of trees in the model could be improve the simulation, as there are many trees along Nathan Road and Canton Road. Another aspect for further study is the consideration of EDR. The hardware and software of the smart lamppost microclimate stations would need to be modified to store second-level wind data so that the EDR can be calculated and compared with the sub-grid scale EDR from the model simulations.

4. Conclusions

This paper presents the RAMS and RAMS-CFD simulation results for a microclimate study in two regions in Hong Kong, namely, the TKO bridge (from a road traffic management perspective) and the TST area (from an urban meteorology perspective), during the strong south to southwesterly flow associated with a tropical cyclone (severe tropical storm Wutip) in June 2025. This study makes several notable observations. Firstly, although the inclusion of CFD did not improve the accuracy of the simulated mean winds (1-min or 10-min averages) based on RMSE statistics, the use of CFD helped capture the fluctuations in wind speed, as shown in the TI. Secondly, by comparing the measured data with the RAMS simulation alone and the RAMS-CFD simulation, the urban impact on the wind was clearly demonstrated, and the TIs simulated from RAMS-CFD generally had better results, although the maximum achievable TIs from actual observations remain unachieved. The results of this study suggest that, for mean wind speed in LAE applications, the use of mesoscale meteorological data alone may provide reasonable results. However, if turbulence needs to be considered, the inclusion of CFD is necessary, although sometimes the inclusion of CFD does not yet achieve the level of TI, as occasionally observed.

Turbulence is an interesting area with application value for future studies. The EDR is definitely an aspect that can be explored. If observations of EDR are available, then the impact of considering terrain alone (by mesoscale meteorological model) and both terrain and buildings (RAMS-CFD), which would provide a sufficiently accurate EDR for LAE application purposes, can be assessed. Secondly, upper-air wind measurements, for example, from ground-based Doppler LIDAR, remain unavailable. The inclusion of upper air wind data for comparison would yield more insight into the relative performance of RAMS alone and RAMS-CFD.

In addition, drone-based observations offer a promising pathway to address some of these observational gaps (*Hervo et al.*, 2023; *Inoue et al.*, 2025). Drones could provide targeted, high-resolution measurements of low-level wind profiles and turbulence-related quantities along critical corridors (e.g., bridge decks and urban street canyons), and could be used to derive turbulence metrics (including EDR proxies), where fixed stations are sparse. Such datasets would strengthen validation of both mean winds and turbulence characteristics, and could potentially support improved specification (or even assimilation) of boundary conditions for mesoscale-to-CFD coupling. These aspects — EDR observations, upper-air wind measurements, and the integration of drone-based measurements — will be the focus of our future studies.

References

Blocken, B. and *Carmeliet, J.*, 2004: Pedestrian Wind Environment around Buildings: Literature Review and Practical Examples. *Journal of Thermal Envelope and Building Science, 28(2),* 107–159. https://doi.org/10.1177/1097196304044396

Cai, C. S., Hu, J., Chen, S., Han, Y., Zhang, W., and *Kong, X.*, 2015: A coupled wind-vehicle-bridge system and its applications: a review. *Wind and Structures, 20(2),* 117–142. https://doi.org/10.12989/was.2015.20.2.117

Deardorff, J. W., 1980: Stratocumulus-capped mixed layers derived from a three-dimensional model. *Boundary-Layer Meteorology, 18(4),* 495–527. https://doi.org/10.1007/BF00119502

Gianfelice, M., Aboshosha, H., and Ghazal, T., 2022: Real-time Wind Predictions for Safe Drone Flights in Toronto. *Results in Engineering, 15, 100534.* https://doi.org/10.1016/j.rineng.2022.100534

Hervo, M., Romanens, G., Martucci, G., Weusthoff, T., and *Haefele, A.*, 2023: A. Evaluation of an Automatic Meteorological Drone Based on a 6-Month Measurement Campaign. *Atmosphere, 14, 1382.* https://doi.org/10.3390/atmos14091382

Inoue, J., Seko, H., Sato, K., and *Sakai, T.*, 2025: Operational capability of drone-based meteorological profiling in an urban area. *Journal of Geophysical Research: Atmospheres, 130, e2024JD041927.* https://doi.org/10.1029/2024JD041927

Kadivar, M., Tormey, D., and *McGranaghan, G.*, 2021: A review on turbulent flow over rough surfaces: Fundamentals and theories. *Int. J. Thermofluids 10, 100077.* https://doi.org/10.1016/j.ijft.2021.100077

Kim, Y., Castro, I. P., and *Xie, Z.-T.*, 2013: Divergence-free turbulence inflow conditions for large-eddy simulations with incompressible flow solvers. *Computers & Fluids, 84,* 56–68. https://doi.org/10.1016/j.compfluid.2013.06.001

Krogstadt, PÅ. and *Antonia, R.*, 1999: Surface roughness effects in turbulent boundary layers. *Experiments in Fluids 27,* 450–460. https://doi.org/10.1007/s003480050370

Lefevre, A., Malet-Damour, B., Boyer, H., and *Rivière, G.*, 2024: Advancing Urban Microclimate Monitoring: The Development of an Environmental Data Measurement Station Using a Low-Tech Approach. *Sustainability, 16(7), 3093.* https://doi.org/10.3390/su16073093

Liu, Z., Cheng, K. Y., He, Y., Jim, C. Y., Brown, R. D., Shi, Y., Lau, K., and *Ng, E.*, 2022: Microclimatic measurements in tropical cities: Systematic review and proposed guidelines. *Building and Environment, 222, 109411.* https://doi.org/10.1016/j.buildenv.2022.109411

Lo, K. W., Chan, P. W., Lai, K. K., Lau, S. P. W., and *Zhao, Z. H.*, 2024a: Case studies of the winds in the urban area of Hong Kong – Microclimate station observations and high resolution numerical simulations. *Heliyon, 10(18), e37865.* https://doi.org/10.1016/j.heliyon.2024.e37865

Lo, K.-W., Chan, P.-W., and *Lai, K.-K.*, 2024b: Observations and Simulations of the Winds at a Bridge in Hong Kong during Two Tropical Cyclone Events in 2023. *Applied Sciences, 14(17), 7789.* https://doi.org/10.3390/app14177789

Maronga, B., Banzhaf, S., Burmeister, C., Esch, T., Forkel, R., Fröhlich, D., Fuka, V., Gehrke, K. F., Geletič, J., Giersch, S., Gronemeier, T., Groß, G., Heldens, W., Hellsten, A., Hoffmann, F., Inagaki, A., Kadasch, E., Kanani-Sühring, F., Ketelsen, K., and *Raasch, S.*, 2020: Overview of the PALM model system 6.0. *In Geoscientific Model Development (Vol. 13, Issue 3).* https://doi.org/10.5194/gmd-13-1335-2020

Maronga, B., Gryschka, M., Heinze, R., Hoffmann, F., Kanani-Sühring, F., Keck, M., Ketelsen, K., Letzel, M. O., Sühring, M., and *Raasch, S.*, 2015: The Parallelized Large-Eddy Simulation Model (PALM) version 4.0 for atmospheric and oceanic flows: Model formulation, recent developments, and future perspectives. *Geoscientific Model Development, 8(8),* 2515–2551. https://doi.org/10.5194/gmd-8-2515-2015

Oke, T. R., 2006: Towards better scientific communication in urban climate. *Theoretical and Applied Climatology, 84(1–3),* 179–190. https://doi.org/10.1007/s00704-005-0153-0

Raasch, S. and *Schröter, M.*, 2001: PALM - A large-eddy simulation model performing on massively parallel computers. *Meteorologische Zeitschrift, 10(5),* 363–372. https://doi.org/10.1127/0941-2948/2001/0010-0363

Wicker, L. J. and *Skamarock, W. C.,* 2002: Time-Splitting Methods for Elastic Models Using Forward Time Schemes. *Monthly Weather Review, 130(8),* 2088–2097. https://doi.org/10.1175/1520-0493(2002)130<2088:TSMFEM>2.0.CO;2

Williamson, J. H., 1980: Low-storage Runge-Kutta schemes. *Journal of Computational Physics, 35(1),* 48–56. https://doi.org/10.1016/0021-9991(80)90033-9

Xie, Z.-T. and *Castro, I. P.,* 2008: Efficient Generation of Inflow Conditions for Large Eddy Simulation of Street-Scale Flows. *Flow, Turbulence and Combustion, 81(3),* 449–470. https://doi.org/10.1007/s10494-008-9151-5

DOI:10.28974/idojaras.2026.3.2

IDŐJÁRÁS

Quarterly Journal of the HungaroMet Hungarian Meteorological Service
Vol. 130, No. 3, July – September, 2026, pp. 245–271

Considerations regarding the evolution of the De Martonne Aridity Index in the eastern part of the Pannonian Plain

Mihai Dudaş[1,*] and **Vlad Dragoslav Mircov**[2]

[1] *Jimbolia Technical School*
Gheorghe Doja 14, Jimbolia 305400, Romania

[2] *"King Mihai I" University of Life Sciences*
119 Aradului Avenue, Timişoara 300645, Romania

**Corresponding author E-mail: dudasmihai@liceuljimbolia.ro*

(Manuscript received in final form on September 25, 2025)

Abstract— The phenomenon of climate aridization is becoming increasingly prominent in both scientific and popular discourses. A plethora of studies have been conducted on this subject, including studies covering the Pannonian Plain; however, comparatively fewer have focused on its eastern region. The present article aims to address this knowledge gap by exploring the potential for aridization at the local scale. We are aware that only by analyzing the evolution of the De Martonne Aridity Index it may not be possible to draw final irrevocable conclusions about the aridization of the climate in the study area, but we believe that it may be a start in this direction. The present study was conducted using data from eight meteorological stations, four from Romania and two each from Hungary and Serbia, for the 1951–2020 time period, and data from three meteorological stations, two from Hungary and one from Romania, for the 1901–2020 time period. The evolution trends of the De Martonne Aridity Index and its component parameters (temperature and precipitation) were analyzed with the help of the non-parametric Mann-Kendall test.

Key-words: De Martonne Aridity Index (DMAI), temperatures, precipitation amounts, Mann-Kendall test, Pannonian Plain

1. *Introduction*

The subject of climate change has been the focus of worldwide discussion since the late 19th century, with an increasing level of engagement observed in recent decades from both scientific and political communities. The most evident of the climate changes, at least at the local level, is the rise in temperatures. The present study will concentrate on the phenomenon of aridization, which is caused not only by a decrease in precipitation, but also by an increase in water demand, which in turn is partly caused by rising temperatures.

In order to express the level of aridization in the area under study, the De Martonne Aridity Index (DMAI) will be employed. Widely used in climatology in order to identify dry/wet climatic conditions in different regions: *Baltas* (2007), for northern Greece, *Deniz et al.* (2011), for Turkey, *Croitoru et al.* (2013), for the extra-Carpathian regions of Romania, *Nistor* (2016), for the Emilia-Romagna region in Italy, *Moral et al.* (2017), for Extremadura, in southwestern Spain, *Vlăduţ* and *Licurici* (2020), for Oltenia, in southern Romania etc., the De Martonne Aridity Index (DMAI) is an indicator that includes both temperature and precipitation and can be calculated for different time scales.

The aim of the present study is to observe the evolution over time of temperatures, precipitation, and the De Martonne Aridity Index in the eastern part of the Pannonian Plain, in an attempt to complete the image provided by the numerous studies carried out on this subject at the level of the Pannonian Plain or certain parts of it (*Gocić and Trajković*, 2012; *Hrnjak et al.*, 2014; *Toşić et al.*, 2014; *Gavrilov et al.*, 2015, 2016, 2019, 2020; *Milentijević et al.*, 2022; *Kiss et al.*, 2023), studies that do not cover the part of the plain included within the border of Romania.

2. *Materials and methodology*

2.1. Study area

The area under discussion (*Fig.1*) is located east of the river Tisza, within the territories of three states: Hungary in the north-west, Serbia in the south-west and Romania in the east. The geographical location of the area, in conjunction with the general movement of the atmosphere, is a determining factor in the existence of a moderate temperate continental climate. Small variations in the main climatic elements are observed, both in terms of temperature, which increases from north to south, and precipitation, which decreases from east to west, with increasing distance from the mountainous area (*Table 1, Table 2*).

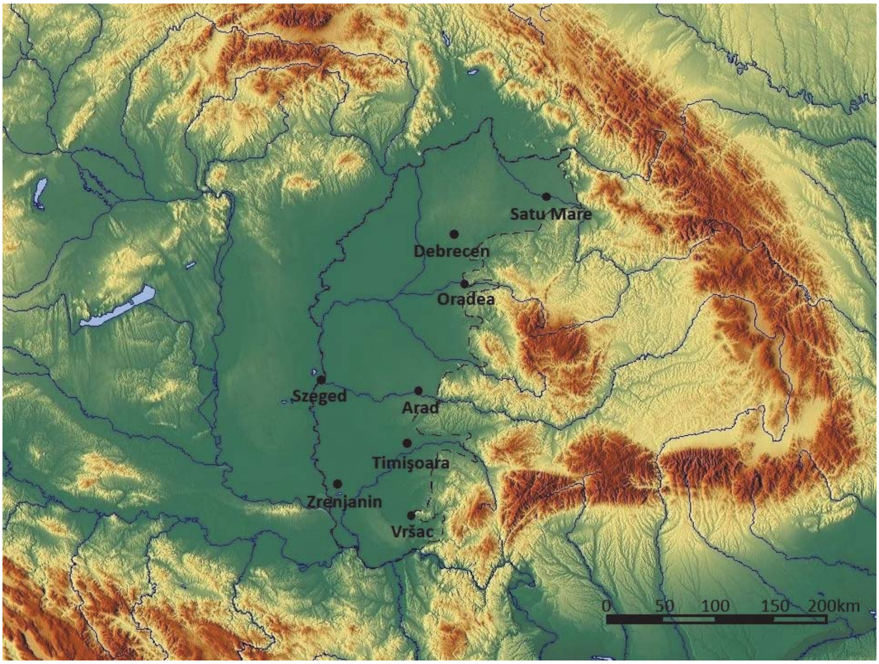

Fig.1. Location of the study area with the distribution of the main meteorological stations.

Table 1. Mean air temperatures (°C) and precipitation amounts (mm) for the 1951–2020 time period

	Station name	**Mean air temperature (°C) and precipitation amount (mm)**				
		annual	**winter**	**spring**	**summer**	**autumn**
1.	Satu Mare	9.9 620	-0.7 131	10.3 145	20.0 208	10.0 136
2.	Oradea	10.6 613	0.1 123	10.8 145	20.5 210	10.9 136
3.	Arad	10.8 588	0.3 118	11.0 145	20.8 197	11.1 128
4.	Timişoara	11.1 602	0.6 126	11.4 147	21.1 195	11.3 136
5.	Debrecen	10.4 554	-0.4 108	10.8 132	20.4 194	10.6 120
6.	Szeged	10.9 516	0.3 97	11.2 124	20.9 177	11.2 117
7.	Zrenjanin	11.4 583	1.0 120	11.7 141	21.3 190	11.8 131
8.	Vršac	11.9 655	1.8 134	11.9 157	21.3 221	12.4 144
	average	10.9 591	0.4 120	11.1 142	20.8 199	11.2 131

Table 2. Mean air temperatures (°C) and precipitation amounts (mm) for the 1901–2020 time period

	Station name	Mean air temperature (°C) and precipitation amount (mm)				
		annual	**winter**	**spring**	**summer**	**autumn**
1.	Debrecen	10.0 566	-0.7 106	10.6 135	20.1 192	10.2 133
2.	Szeged	11.0 535	0.3 100	11.3 133	21.1 172	11.3 130
3.	Timişoara	11.1 611	0.4 126	11.4 151	21.0 191	11.4 143
	average	10.7 571	0.0 111	11.1 140	20.7 185	11.0 135

2.2. Data and methodology

Although the earliest known meteorological measurements in the area under study were recorded in the late 18th century (*Réthly*, 1918; *Dudaş* and *Urdea*, 2023; *Dudaş*, 2025), and during the 19th century measurements were taken in several localities (*Réthly*, 1970, 1998), the sporadic nature of these measurements, as well as their lack of accuracy according to current standards, led us not to mention them during this work. The lack of measurements or the incomplete data strings obtained from various meteorological stations for the 20th century, in addition to the difficulty in accessing meteorological data from Romanian stations, further constrained the selection of meteorological stations to be incorporated in this study. Under the given circumstances, we aimed to achieve a certain symmetry between the stations in Romania and those in Hungary and Serbia, as well as a relatively uniform distribution of these stations, finally opting for eight stations to calculate the De Martonne Index for the 1951–2020 time period and 3 meteorological stations for the 1901–2020 time period (*Fig.1*, *Table 1*, *Table 2*).

The completion of this project necessitated the execution of several distinct stages. Initially, a small database was constructed in Excel, containing temperature and precipitation values from the meteorological stations under consideration. These data were then analyzed to avoid discrepancies. Datasets for Szeged and Debrecen can be accessed online on the website of the HungaroMet Hungarian Meteorological Service (*https://www.met.hu/*). Data for Zrenjanin and Vršac can be found in the Meteorological Yearbooks (Meteorološki godišnjak) of the Federal Hydrometeorological Institute of Yugoslavia / Republican Hydrometeorological Service of Serbia, available online on the website of the Serbian Republican Hydrometeorological Service (*http://www.hidmet.gov.rs/*), or on the www.meteologos.rs meteorological website. The data for the four meteorological stations in Romania (Satu Mare, Oradea, Arad, and Timișoara) were partly purchased from the Regional Meteorological Center Banat–Crișana (Centrul Meteorologic Regional Banat–Crişana), partly collected from meteorological reports (*Berecz E.*, 1901–1910; *Berecz O.*, 1910–1917; *Ehmann*, 1918; *Institutul Meteorologic Central al României*, 1921–1959) or Romanian Statistical Yearbooks (*Direcţia Centrală de Statistică*, 1961–1989; *Comisia Naţională pentru Statistică*, 1990–1999; *Institutul Naţional de Statistică*, 2000 – 2021).

The annual and seasonal De Martonne Aridity Index was calculated for all the meteorological stations included in the study. Widely used in applied climatology, the De Martonne Aridity Index (DMAI) is given by the equations:

$$I_{\mathrm{a}} = \frac{P_{\mathrm{a}}}{T_{\mathrm{a}}+10}, \tag{1}$$

for the annual DMAI, where P_a is the annual amount of precipitation (mm) and T_a is the mean annual surface temperature (°C), and

$$I_{\mathrm{s}} = \frac{4P_{\mathrm{s}}}{T_{\mathrm{s}}+10}, \tag{2}$$

for the seasonal DMAI, where P_s is the seasonal amount of precipitation (mm) and T_a is the mean seasonal surface temperature (°C).

The classification of the DMAI is presented in *Table 3*, with the studied area belonging to the semi-humid and humid climate types.

Table 3. The De Martonne Aridity Index (DMAI) classification (*Gavrilov et al.*, 2020)

Types of climate	**Values of DMAI**
arid	$I < 10$
semi-arid	$10 \leq I < 20$
mediterranean	$20 \leq I < 24$
semi-humid	$24 \leq I < 28$
humid	$28 \leq I < 35$
very-humid	$35 \leq I \leq 55$
extremely humid	$I > 55$

The next step in the research was to create graphs representing the evolution of this parameter over time and to obtain the trend equation using linear regression, both for annual and seasonal trends. The trend equation was calculated by Excel with the formula $y = ax+b$, where y represents the parameter in a given year, a the slope, x the time in years, and b the parameter at the beginning of the period. Easy to perform and interpret, there are three possible scenarios: if $a \geq 0$, the trend is positive, increasing, if *a* = 0, there is no trend, and if $a \leq 0$ the trend is negative, decreasing (*Gavrilov et al.*, 2016; *Dudaş* and *Urdea*, 2023).

The Mann-Kendall non-parametric test was employed to ascertain the presence of trends in both annual and seasonal values. Under MK test, two hypotheses have been tested: the null hypothesis, H_o, indicating no trend in the time series, and the alternative hypothesis, H_a, indicating that there is a significant trend in the time series for a given level of significance. The probability, *p*, has been calculated in percents to determine the level of confidence in the hypothesis. When the *p* value calculated is less than the assumed significance level a (e.g. *a*=5%), the H_o hypothesis has to be rejected (no trend) and the Ha (there is a significant trend) should be accepted. If *p* is higher than significance level *a*, the H_o hypothesis (no trend) cannot be rejected (*Gavrilov et al.*, 2016; *Dudaş* and *Urdea*, 2023). XLSTAT software (*http://www.xlstat.com/en/*) has been used to calculate the probability and hypothesis testing.

3. Results

As previously mentioned, the following discussion will attempt to illustrate the evolution trends of the DMAI in the eastern part of the Pannonian Plain. However, prior to the discussion of the DMAI itself, we consider it necessary to briefly analyze the evolution over time of the two parameters that define the DMAI: temperature and precipitation.

3.1. Temperature

The analysis of temperature data over the **1951–2020** time period reveals a consistent increase at all analyzed meteorological stations, both in terms of annual and seasonal averages. The Mann-Kendall trend test confirmed the trend of the annual, spring and summer averages for all analyzed meteorological stations. However, the test did not confirm the trend of winter temperatures, with the exception of Zrenjanin meteorological station, and the trend of autumn temperatures, with the exception of Oradea and Zrenjanin meteorological stations (*Table 4*). Considering the average temperature of the eight meteorological stations, over the 1951–2020 time period temperatures have increased both annually and seasonally, with the MK test confirming this trend only for the annual, spring and summer averages (*Fig. 2, Table 5*).

Table 4. Annual and seasonal temperature trends for the 1951–2020 time period

	Station name	**Temperature trends (1951–2020)**									
		annual		**winter**		**spring**		**summer**		**autumn**	
		p-value	Sen's slope	p-value	Sen's slope	p-value	Sen's slope	p-value	Sen's slope	p-value	Sen's slope
1.	Satu Mare	**0.001**	0.020	0.140	0.019	**0.000**	0.024	**<0.0001**	0.031	0.490	0.005
2.	Oradea	**<0.0001**	0.027	0.089	0.022	**<0.0001**	0.030	**<0.0001**	0.037	**0.049**	0.015
3.	Arad	**0.000**	0.020	0.203	0.014	**0.000**	0.022	**<0.0001**	0.031	0.402	0.007
4.	Timişoara	**<0.0001**	0.027	0.057	0.020	**<0.0001**	0.031	**<0.0001**	0.037	0.078	0.013
5.	Debrecen	**<0.0001**	0.024	0.084	0.020	**<0.0001**	0.029	**<0.0001**	0.030	0.081	0.013
6.	Szeged	**<0.0001**	0.024	0.082	0.019	**<0.0001**	0.029	**0.000**	0.027	0.103	0.012
7.	Zrenjanin	**<0.0001**	0.030	**0.022**	0.025	**<0.0001**	0.033	**<0.0001**	0.031	**0.033**	0.018
8.	Vršac	**<0.0001**	0.026	0.201	0.017	**<0.0001**	0.032	**<0.0001**	0.035	0.171	0.012

Table 5. Annual and seasonal temperature trends for the 1951–2020 time period as an average for the entire area

Variable	**Minimum**	**Maximum**	**Mean**	**Std. deviation**	**Kendall's tau**	**p-value**	**Sen's slope**
annual	9.3	12.9	10.9	0.871	0.365	**<0.0001**	0.025
winter	-5.1	4.1	0.4	1.991	0.137	0.094	0.019
spring	8.3	13.5	11.1	1.113	0.364	**<0.0001**	0.028
summer	18.5	23.5	20.8	1.170	0.371	**<0.0001**	0.032
autumn	8.5	13.9	11.2	1.137	0.133	0.106	0.013

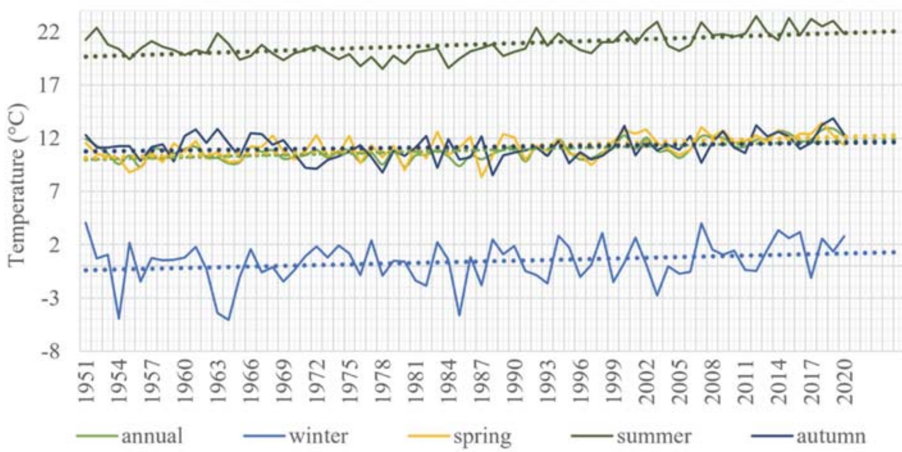

Fig. 2. Annual and seasonal temperature trends for the 1951–2020 time period as an average for the entire area. Dotted lines indicate linear trends.

For the **1901–2020** time period, temperatures have increased at all analyzed meteorological stations, either as annual or seasonal averages. The evolution trend is confirmed by the Mann-Kendall trend test for Debrecen, for both the annual and seasonal averages, and for Timişoara, only for the annual, spring and summer averages (*Table 6*). Considering the average temperature of the three meteorological stations, over the period 1901–2020 temperatures have increased both annually and seasonally, with the MK test confirming this trend only for the annual, spring and summer averages (*Fig. 3, Table 7*).

Table 6. Annual and seasonal temperature trends for the 1901–2020 time period

	Station name	Temperature trends (1901–2020)									
		annual		winter		spring		summer		autumn	
		p-value	Sen's slope	p-value	Sen's slope	p-value	Sen's slope	p-value	Sen's slope	p-value	Sen's slope
1.	Debrecen	**<0.0001**	0.015	**0.008**	0.015	**<0.0001**	0.017	**<0.0001**	0.016	**<0.0001**	0.013
2.	Szeged	0.204	0.003	0.390	0.005	0.141	0.005	0.720	0.000	0.902	0.000
3.	Timişoara	**0.020**	0.005	0.142	0.008	**0.045**	0.006	**0.011**	0.007	0.906	0.000

Table 7. Annual and seasonal temperature trends for the 1901–2020 time period as an average for the entire area

Variable	Minimum	Maximum	Mean	Std. deviation	Kendall's tau	p-value	Sen's slope
annual	8.4	12.8	10.7	0.810	0.208	**0.001**	0.007
winter	-5.3	3.7	0.0	2.012	0.101	0.104	0.010
spring	8.4	14.4	11.1	1.168	0.182	**0.003**	0.009
summer	18.5	23.3	20.7	1.055	0.172	**0.005**	0.008
autumn	7.7	13.6	11.0	1.217	0.080	0.199	0.005

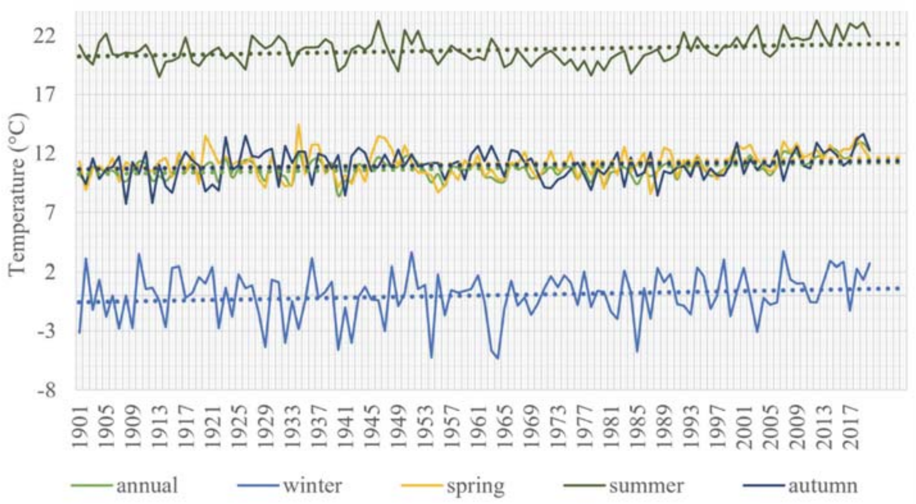

Fig. 3. Annual and seasonal temperature trends for the 1901–2020 time period as an average for the entire area. Dotted lines indicate linear trends.

3.2. *Precipitation*

For the **1951–2020** time period, an increasing trend in annual precipitation was observed for the average of the eight meteorological stations, as well as for Satu Mare, Oradea, Arad, Szeged, and Zrenjanin. Conversely, a decreasing trend was observed for Timişoara, Debrecen, and Vršac. Winter precipitation amounts are recording a decreasing trend for all meteorological stations and for their average, spring precipitation amounts are recording an increasing trend for the average and all meteorological stations, except Zrenjanin, summer precipitation amounts are recording an increasing trend for the average of the eight meteorological stations and for Oradea, Arad, Szeged, and Vršac, and a decreasing trend for Satu Mare, Timișoara, Debrecen, and Zrenjanin, and autumn precipitation amounts are recording an increasing trend for all meteorological stations and for their average (*Fig. 4*, *Table 8*, *Table 9*). The Mann-Kendal trend test confirms the trend only for the autumn precipitation amounts in Satu Mare (*Table 8*).

Table 8. Annual and seasonal precipitation trends for the 1951–2020 time period

	Station name	Precipitation trends (1951–2020)									
		annual		winter		spring		summer		autumn	
		p-value	Sen's slope	p-value	Sen's slope	p-value	Sen's slope	p-value	Sen's slope	p-value	Sen's slope
1.	Satu Mare	0.282	0.782	0.271	-0.288	0.392	0.266	0.619	-0.212	**0.002**	1.083
2.	Oradea	0.453	0.571	0.250	-0.310	0.670	0.115	0.567	0.248	0.196	0.444
3.	Arad	0.378	0.613	0.230	-0.321	0.670	0.100	0.441	0.305	0.100	0.567
4.	Timişoara	0.988	-0.019	0.086	-0.443	0.847	0.038	0.984	-0.005	0.182	0.451
5.	Debrecen	0.776	-0.256	0.061	-0.417	0.715	0.086	0.375	-0.348	0.258	0.375
6.	Szeged	0.711	0.267	0.372	-0.194	0.746	0.100	0.530	0.292	0.118	0.495
7.	Zrenjanin	0.796	0.172	0.296	-0.306	0.560	-0.217	0.883	-0.042	0.086	0.594
8.	Vršac	0.895	-0.129	0.456	-0.247	0.435	0.187	0.956	0.053	0.567	0.267

Table 9. Annual and seasonal precipitation trends for the 1951–2020 time period as an average for the entire area

Variable	**Minimum**	**Maximum**	**Mean**	**Std. deviation**	**Kendall's tau**	**p-value**	**Sen's slope**
annual	336	858	591	99.077	0.045	0.584	0.368
winter	40	217	120	38.031	-0.124	0.130	-0.305
spring	58	244	142	37.157	0.046	0.577	0.126
summer	71	327	199	56.461	0.004	0.968	0.013
autumn	28	272	131	49.586	0.147	0.074	0.540

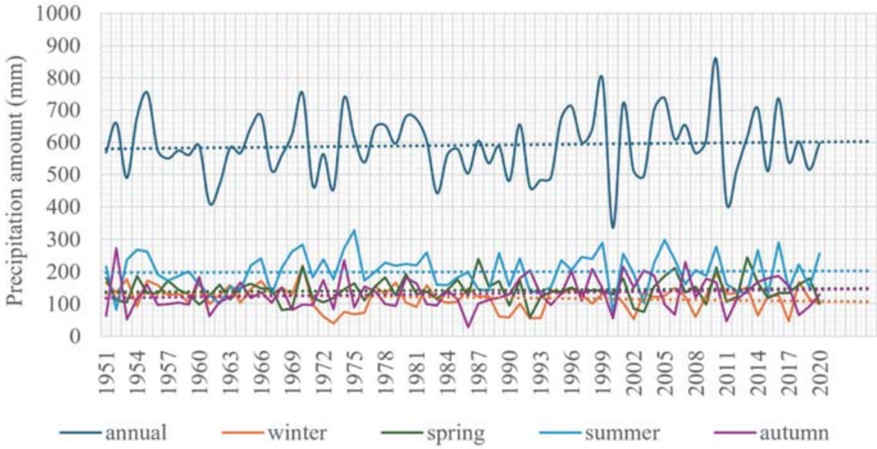

Fig. 4. Annual and seasonal precipitation trends for the 1951–2020 time period as an average for the entire area. Dotted lines indicate linear trends.

The general trend for the **1901–2020** time period is one of decrease, both for the three meteorological stations and for their averages, with the exception of the summer season. In this season, precipitation levels increased at the Timişoara and Szeged meteorological stations, as well as for the average of the three stations. The Mann-Kendal trend test does not confirm the trend for either annual or seasonal averages (*Fig. 5, Table 10, Table 11*).

Table 10. Annual and seasonal precipitation trends for the 1901–2020 time period

	Station name	Precipitation trends (1901–2020)									
		annual		winter		spring		summer		autumn	
		p-value	Sen's slope	p-value	Sen's slope	p-value	Sen's slope	p-value	Sen's slope	p-value	Sen's slope
1.	Debrecen	0.131	-0.498	0.705	-0.034	0.303	-0.108	0.980	-0.004	0.051	-0.270
2.	Szeged	0.074	-0.511	0.337	-0.104	0.051	-0.266	0.331	0.189	0.123	-0.249
3.	Timişoara	0.320	-0.291	0.380	-0.109	0.279	-0.119	0.599	0.075	0.686	-0.057

Table 11. Annual and seasonal precipitation trends for the 1901–2020 time period as an average for the entire area

Variable	Minimum	Maximum	Mean	Std. deviation	Kendall's tau	p-value	Sen's slope
annual	312	882	571	102.985	-0.096	0.121	-0.443
winter	40	214	111	36.536	-0.057	0.357	-0.094
spring	47	259	140	41.264	-0.089	0.151	-0.161
summer	70	324	185	55.494	0.040	0.515	0.098
autumn	21	257	135	49.663	-0.075	0.228	-0.178

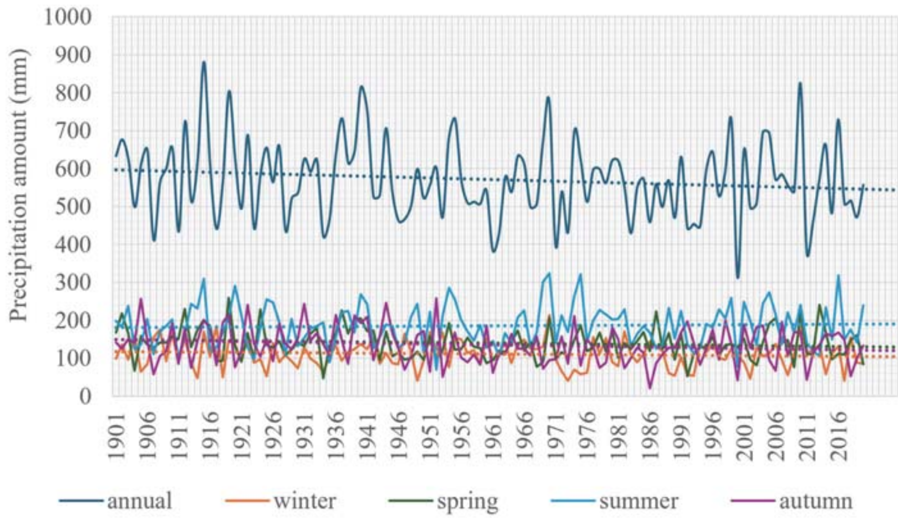

Fig. 5. Annual and seasonal precipitation trends for the 1901–2020 time period as an average for the entire area. Dotted lines indicate linear trends.

3.3. *De Martonne Aridity Index (1951–2020)*

The annual DMAI for the entire analyzed region has an average value of 28.4, with above-average values in Satu Mare, Vršac, and Oradea, close to average values in Timișoara and Arad, and below-average values in Szeged, Debrecen, and Zrenjanin (*Table 12*). The lowest average value was calculated for the year 2000 and the highest for 2010. The absolute minimum was calculated for Szeged in 2000 and the absolute maximum for Satu Mare in 2010.

Table 12. Evolution of the annual DMAI for the 1951–2020 time period analyzed by Mann-Kendall trend tests

Station name	Trend equation	Min.	Max.	Mean	Std. deviation	Kendall 's tau	p-value	Sen's slope
Satu Mare	y= 0.011x + 30.75	19.0	**49.1**	**31.1**	5.600	0.017	0.839	0.006
Oradea	y= -0.0116x+30.267	16.5	45.2	29.9	6.105	-0.032	0.700	-0.010
Arad	y= 0.0011x+28.306	11.3	40.8	28.3	5.557	-0.005	0.951	0.000
Timişoara	y= -0.0448x+30.235	13.2	43.8	28.6	5.771	-0.087	0.292	-0.029
Debrecen	y= -0.0361x+28.587	15.6	48.3	27.3	6.021	-0.104	0.205	-0.031
Szeged	y= -0.0046x+24.933	**9.1**	39.7	**24.8**	5.659	-0.020	0.808	0.000
Zrenjanin	y= -0.0231x+28.085	12.0	41.7	27.3	5.899	-0.043	0.605	-0.012
Vršac	y= -0.0286x+31.067	14.0	46.6	30.1	6.665	-0.068	0.406	-0.020
average	y= -0.0171x+29.029	15.2	40.5	28.4	5.033	-0.043	0.605	-0.010

Observing the evolution of the annual DMAI (*Fig. 6, Fig. 11, Table 12*) reveals a relative constancy for the analyzed period, with slight decreases for average and for Oradea, Timişoara, Debrecen, Szeged, Zrenjanin, and Vršac, and a very slight increase for Satu Mare and Arad. No trend is confirmed by the Mann- [illegible] 2).

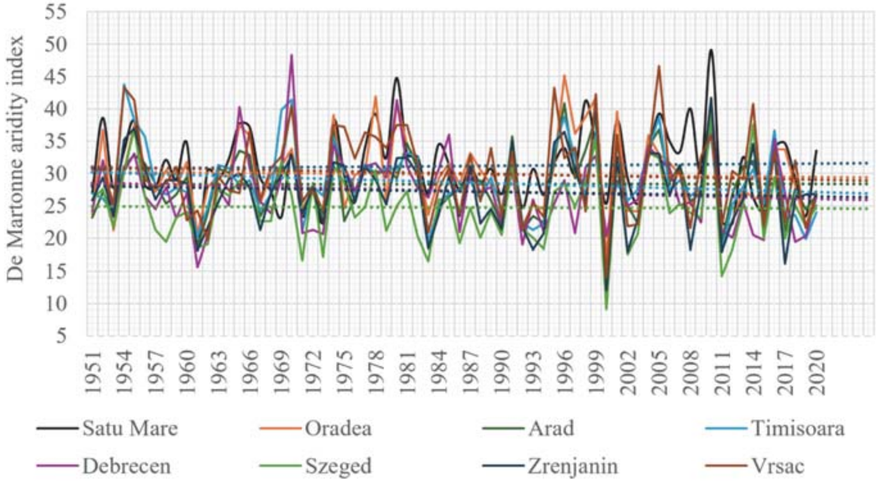

Fig. 6. Annual DMAI trends for the 1951–2020 time period. Dotted lines indicate linear trends.

The winter DMAI for the entire analyzed region has an average value of 48.6, with above-average values in Satu Mare, Oradea and Timişoara and below-average values for the other meteorological stations (*Table 13*). The lowest average value was calculated for the year 1973 and the highest for 1963. The absolute minimum was calculated for Zrenjanin in 1973 and the absolute maximum for Satu Mare in 1963.

Table 13. Evolution of the winter DMAI for the 1951–2020 time period analyzed by Mann-Kendall trend tests

Station name	Trend equation	Min.	Max.	Mean	Std. deviation	Kendall 's tau	p-value	Sen's slope
Satu Mare	y= -0.267x + 69.211	18.2	**146.7**	**59.7**	24.644	-0.125	0.128	-0.214
Oradea	y= -0.265x + 60.379	15.8	118.7	51.0	20.610	-0.193	**0.018**	-0.220
Arad	y= -0.2446x+56.454	13.5	102.6	47.8	19.644	-0.148	0.070	-0.174
Timişoara	y= -0.3562x+62.679	12.6	111.1	50.0	22.932	-0.205	**0.012**	-0.254
Debrecen	y= -0.2823x+56.997	17.0	112.5	47.0	19.080	-0.205	**0.012**	-0.221
Szeged	y= -0.1973x+46.646	10.8	95.3	**39.6**	19.092	-0.125	0.126	-0.145
Zrenjanin	y= -0.3379x+58.476	**9.5**	116.0	46.5	23.080	-0.148	0.071	-0.217
Vršac	y= -0.2449x+55.723	13.2	107.2	47.0	19.769	-0.133	0.105	-0.168
average	y= -0.2744x+58.321	14.8	113.8	48.6	19.291	-0.170	**0.038**	-0.215

Observing the evolution of the winter DMAI (*Fig. 7, Fig. 11, Table 13*) reveals a decrease for the analyzed period, either as an average for the entire region as well as for all meteorological stations. Mann-Kendal trend test confirms the evolution trend for the average and for Oradea, Timişoara, and Debrecen meteorological stations (*Table 13*).

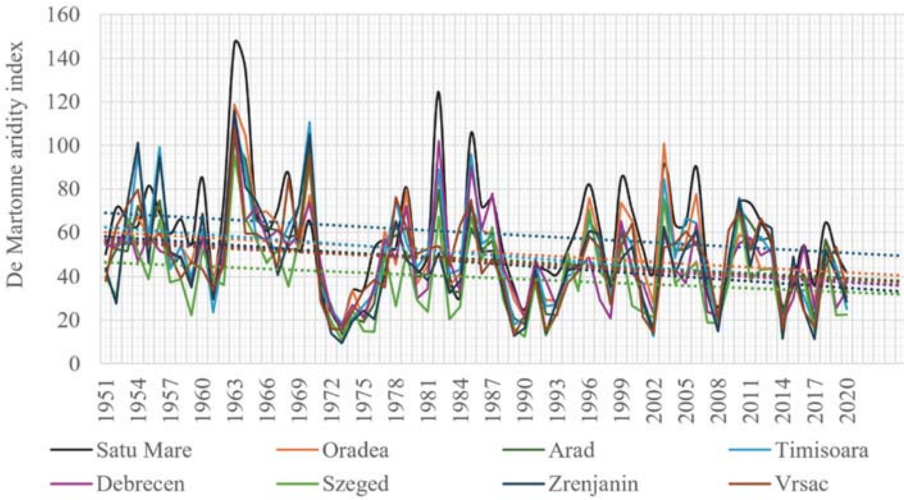

Fig. 7. Winter DMAI trends for the 1951–2020 time period. Dotted lines indicate linear trends.

The spring DMAI for the entire analyzed region has an average value of 27.1, with above-average values in Satu Mare, Oradea, Arad, Timişoara, and Vršac, and below-average values for the other meteorological stations (*Table 14*). The lowest average value was calculated for the year 1992 and the highest for 1987. The absolute minimum was calculated for Szeged in 1992 and the absolute maximum for Vršac in 1987.

Table 14. Evolution of the spring DMAI for the 1951–2020 time period analyzed by Mann-Kendall trend tests

Station name	Trend equation	Min.	Max.	Mean	Std. deviation	Kendall 's tau	p-value	Sen's slope
Satu Mare	y= 0.0271x + 27.608	11.6	57.3	28.6	10.061	0.025	0.766	0.000
Oradea	y= -0.0081x+28.306	9.8	50.2	28.0	9.055	-0.009	0.913	0.000
Arad	y= 0.0013x + 27.752	9.5	52.0	27.8	8.836	-0.024	0.773	0.000
Timişoara	y= -0.0369x+28.973	10.7	60.2	27.7	8.720	-0.057	0.487	-0.005
Debrecen	y= 0.0183x + 24.918	10.5	56.9	25.6	9.644	-0.022	0.789	0.000
Szeged	y= -0.0017x+23.678	**4.5**	42.7	**23.6**	8.555	-0.024	0.773	0.000
Zrenjanin	y= -0.0495x+28.096	8.4	57.7	26.3	9.693	-0.100	0.218	-0.056
Vršac	y= -0.0146x+29.378	8.6	**73.7**	**28.9**	9.990	-0.015	0.858	0.000
average	y= -0.008x + 27.339	10.9	52.1	27.1	7.582	-0.033	0.691	0.000

A relative constancy of the spring DMAI can be observed for the analyzed period (*Fig. 8*, *Fig. 11*, *Table 14*), with very slight decreases for average and for Oradea, Timișoara, Szeged, Zrenjanin, and Vršac meteorological stations and very slight increases for Satu Mare, Arad, and Debrecen. No trend is confirmed by the Mann-Kendal trend test (*Table 14*).

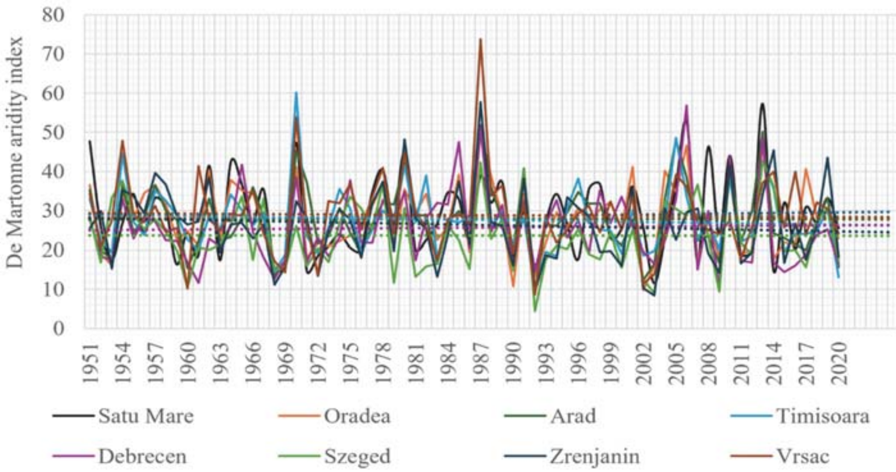

Fig. 8. Spring DMAI trends for the 1951–2020 time period. Dotted lines indicate linear trends.

The summer DMAI for the entire analyzed region has an average value of 26, with above-average values in Vršac, Satu Mare, and Oradea, close to average values in Arad and Debrecen, and below-average values for Timişoara, Zrenjanin, and Szeged (*Table 15*). The lowest average value was calculated for the year 2000 and the highest for 1975. The absolute minimum was calculated for Vršac in 2000 and the absolute maximum for Debrecen in 1970.

Table 15. Evolution of the summer DMAI for the 1951–2020 time period analyzed by Mann-Kendall trend tests

Station name	Trend equation	Min.	Max.	Mean	Std. deviation	Kendall 's tau	p-value	Sen's slope
Satu Mare	y= -0.0527x+29.725	6.9	48.1	27.9	9.826	-0.074	0.361	-0.031
Oradea	y= -0.0012x +27.718	8.9	52.8	27.7	9.365	0.001	0.992	0.000
Arad	y= 0.0204x + 25.039	4.9	44.6	25.8	8.444	0.021	0.796	0.000
Timişoara	y= -0.033x + 26.329	6.5	49.7	25.2	8.662	-0.050	0.545	-0.012
Debrecen	y= -0.0672x+28.045	7.5	**68.8**	25.7	10.463	-0.094	0.251	-0.040
Szeged	y= 0.0079x+22.873	5.4	42.4	**23.2**	9.358	0.023	0.781	0.009
Zrenjanin	y= 0.0022x+24.353	7.7	52.6	24.4	9.477	-0.037	0.655	0.000
Vršac	y= -0.0015x+28.436	**4.5**	62.0	**28.4**	12.025	-0.027	0.743	0.000
average	y= -0.0156x+26.565	8.9	43.7	26.0	7.632	-0.038	0.641	-0.004

Observing the evolution of the summer DMAI (*Fig. 9*, *Fig. 11*, *Table 15*) reveals a relative constancy for the analyzed period, with very slight decreases for the average and for Satu Mare, Oradea, Timişoara, Debrecen, and Vršac, and a very slight increase for Arad, Szeged, and Zrenjanin. No trend is confirmed by the Mann-Kendal trend test (*Table 15*).

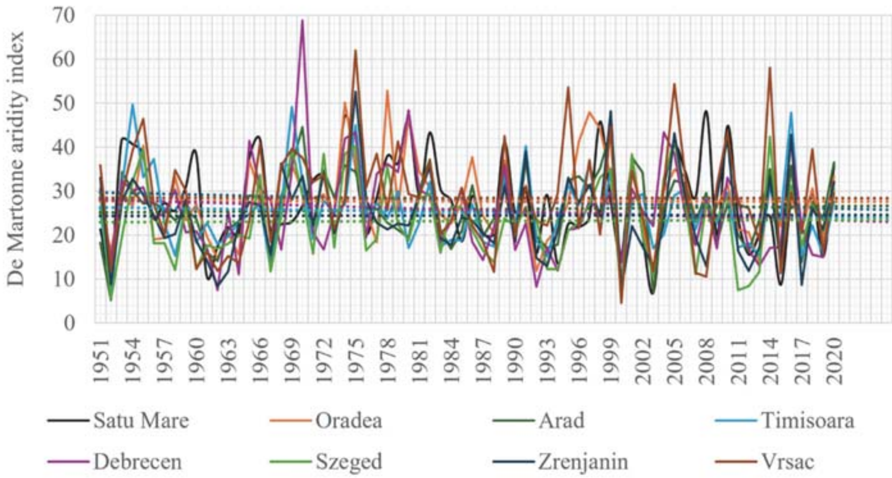

Fig. 9. Summer DMAI trends for the 1951–2020 time period. Dotted lines indicate linear trends.

The autumn DMAI for the entire analyzed region has an average value of 24.9, with above-average values in Satu Mare, Oradea, Vršac, and Timişoara and below-average values for Arad, Debrecen, Zrenjanin, and Szeged (*Table 16*). The lowest average value was calculated for the year 1986 and the highest for 1952. The absolute minimum was calculated for Szeged in 1986 and the absolute maximum for Oradea in 1952.

Table 16. Evolution of the autumn DMAI for the 1951–2020 time period analyzed by Mann-Kendall trend tests

Station name	Trend equation	Min.	Max.	Mean	Std. deviation	Kendall 's tau	p-value	Sen's slope
Satu Mare	y= 0.1696x + 21.249	8.0	64.1	**27.3**	11.793	0.232	**0.004**	0.184
Oradea	y= 0.0484x + 24.481	4.7	**66.3**	26.2	12.034	0.087	0.286	0.029
Arad	y= 0.0645x + 22.109	3.6	52.7	24.4	10.483	0.113	0.166	0.052
Timişoara	y= 0.0404x + 24.196	5.4	55.1	25.6	9.892	0.099	0.224	0.039
Debrecen	y= 0.0392x + 22.149	4.1	47.9	23.5	10.039	0.063	0.439	0.012
Szeged	y= 0.0396x + 20.887	**3.0**	60.3	**22.3**	9.877	0.114	0.163	0.057
Zrenjanin	y= 0.0731x + 21.629	7.0	52.1	24.2	10.412	0.120	0.140	0.051
Vršac	y= 0.0183x + 25.23	6.4	56.2	25.9	10.828	0.020	0.808	0.000
average	y= 0.0616x + 22.741	5.6	51.7	24.9	9.590	0.131	0.108	0.060

Observing the evolution of the autumn DMAI (*Fig. 10*, *Fig. 11*, *Table 16*) reveals a slight increase for the analyzed period, either as an average for the entire region as well as for all meteorological stations. Mann-Kendal trend test confirms only the trend for the Satu Mare meteorological station (*Table 16*).

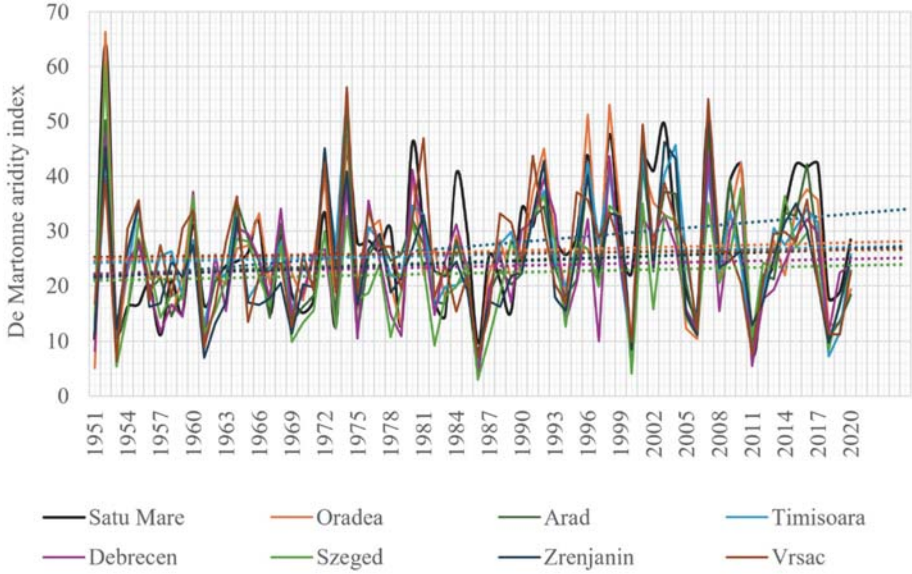

Fig. 10. Autumn DMAI trends for the 1951–2020 time period. Dotted lines indicate linear trends.

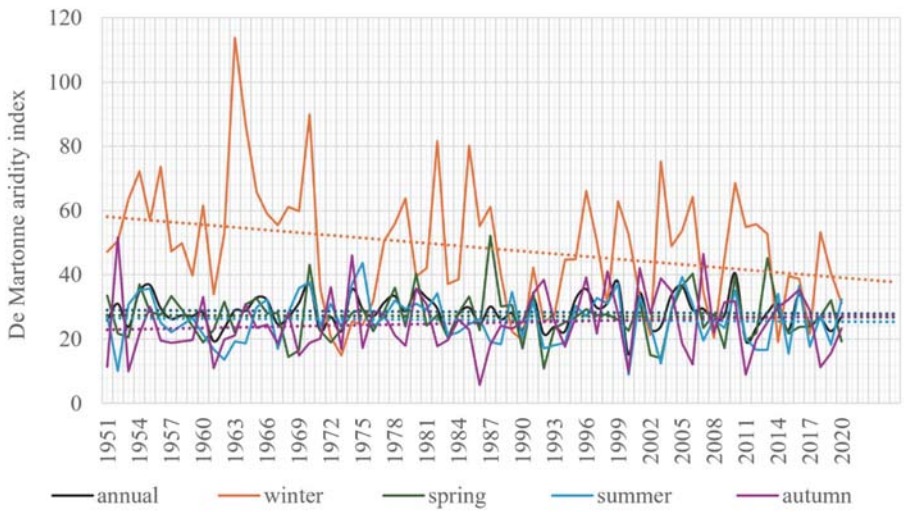

Fig. 11. Annual and seasonal DMAI trends for the 1951–2020 time period as an average for the entire area. Dotted lines indicate linear trends.

3.4. De Martonne Aridity Index (1901–2020)

The annual DMAI for the three analyzed meteorological stations has an average value of 27.7, with above-average values in Timișoara and Debrecen, and below-average values in Szeged (*Table 17*). The lowest average value was calculated for the year 2000 and the highest for 1940. The absolute minimum was calculated for Szeged in 2000 and the absolute maximum for Debrecen in 1970.

Table 17. Evolution of the annual DMAI for the 1901–2020 time period analyzed by Mann-Kendall trend tests

Station name	Trend equation	Min.	Max.	Mean	Std. deviation	Kendall's tau	p-value	Sen's slope
Debrecen	y= -0.0427x+30.987	15.6	**48.3**	28.4	6.495	-0.167	**0.007**	-0.045
Szeged	y= -0.0259x+27.136	**9.1**	45.8	**25.6**	5.890	-0.109	0.079	-0.027
Timișoara	y= -0.0264x+30.714	13.2	47.2	**29.1**	5.990	-0.094	0.129	-0.024
average	y= -0.0317x+29.612	14.2	44.3	27.7	5.439	-0.130	**0.035**	-0.032

Observing the evolution of the annual DMAI (*Fig. 12*, *Fig. 17*, *Table 17*) reveals a decrease for the analyzed period for all three meteorological stations and for their average. The Mann-Kendal trend test confirms the evolution trend only for the average and for Debrecen meteorological station (*Table 17*).

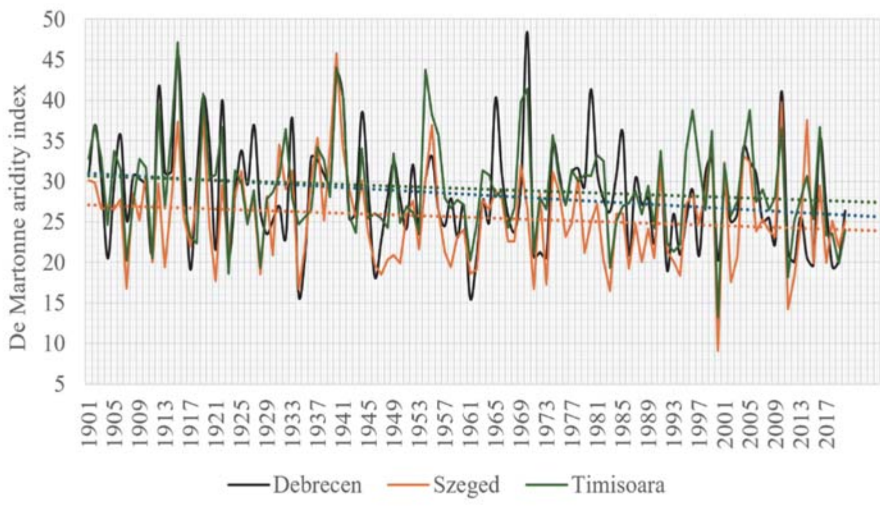

Fig. 12. Annual DMAI trends for the 1901–2020 time period. Dotted lines indicate linear trends.

The winter DMAI has an average value of 46.6, with above-average values in Timișoara and Debrecen, and below-average values in Szeged (*Table 18*). The lowest average value was calculated for the year 1973 and the highest for 1963. The absolute minimum was calculated for Szeged in 1973 and the absolute maximum for Debrecen in 1907.

Table 18. Evolution of the winter DMAI for the 1901–2020 time period analyzed by Mann-Kendall trend tests

Station name	Trend equation	Min.	Max.	Mean	Std. deviation	Kendall 's tau	p-value	Sen's slope
Debrecen	y= -0.0976x+53.761	12.2	**131.2**	47.9	21.470	-0.085	0.167	-0.067
Szeged	y= -0.0619x+44.707	**10.8**	119.7	**41.0**	19.693	-0.079	0.202	-0.059
Timişoara	y= -0.0958x+56.689	12.6	111.1	**50.9**	22.652	-0.100	0.106	-0.084
average	y= -0.0851x+51.719	15.4	106.3	46.6	19.549	-0.094	0.128	-0.073

Observing the evolution of the winter DMAI (*Fig. 13, Fig. 17, Table 18*) reveals a decrease for the analyzed period for all three meteorological stations and for their average. No trend is confirmed by the Mann-Kendal trend test (*Table 18*).

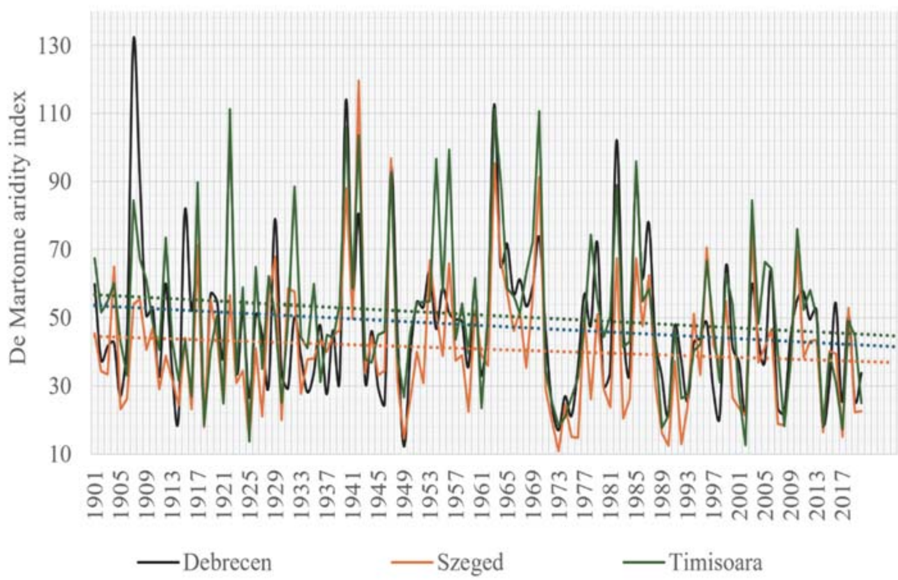

Fig. 13. Winter DMAI trends for the 1901–2020 time period. Dotted lines indicate linear trends.

The spring DMAI has an average value of 26.7, with above-average values in Timişoara and below-average values in Szeged (*Table 19*). The lowest average value was calculated for the year 1934 and the highest for 1919. The absolute minimum was calculated for Szeged in 1992 and the absolute maximum for Timişoara in 1970.

Table 19. Evolution of the spring DMAI for the 1901–2020 time period analyzed by Mann-Kendall trend tests

Station name	Trend equation	Min.	Max.	Mean	Std. deviation	Kendall 's tau	p-value	Sen's slope
Debrecen	y= -0.0348x+28.63	7.3	56.9	26.5	10.247	-0.104	0.092	-0.045
Szeged	y= -0.0527x+28.356	**4.5**	52.4	**25.2**	9.589	-0.125	**0.044**	-0.054
Timişoara	y= -0.0374x+30.725	6.1	**60.2**	**28.5**	9.560	-0.082	0.183	-0.029
average	y= -0.0416x+29.237	7.7	53.3	26.7	8.506	-0.110	0.075	-0.042

Observing the evolution of the spring DMAI (*Fig. 14*, *Fig. 17*, *Table 19*) reveals a decrease for the analyzed period for all three meteorological stations and for their average. The Mann-Kendal trend test confirms the evolution trend only for Szeged (*Table 19*).

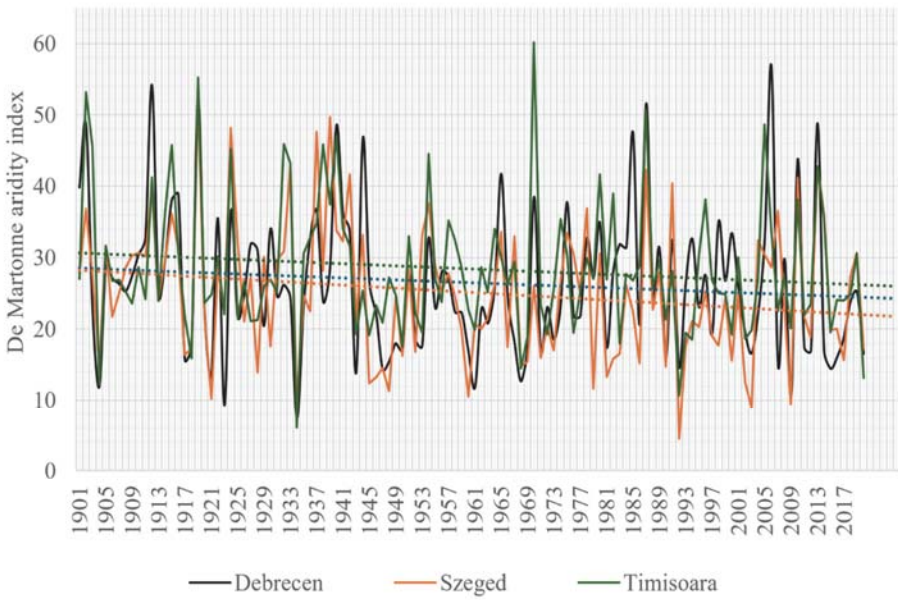

Fig. 14. Spring DMAI trends for the 1901–2020 time period. Dotted lines indicate linear trends.

The summer DMAI has an average value of 24.3, with above-average values for Debrecen and Timişoara and below-average values for Szeged (*Table 20*). The lowest average value was calculated for the year 1952 and the highest for 1970. The absolute minimum was calculated for Szeged in 1952 and the absolute maximum for Debrecen in 1970.

Table 20. Evolution of the summer DMAI for the 1901–2020 time period analyzed by Mann-Kendall trend tests

Station name	Trend equation	Min.	Max.	Mean	Std. deviation	Kendall 's tau	p-value	Sen's slope
Debrecen	y= -0.012x+26.494	7.5	**68.8**	**25.8**	10.512	-0.033	0.597	-0.011
Szeged	y= 0.0224x+20.969	**5.4**	42.4	**22.3**	8.580	0.056	0.363	0.022
Timişoara	y= -3E-05x+24.806	6.5	51.7	24.8	9.019	0.016	0.798	0.005
average	y= -0.0035x+24.09	8.7	43.4	24.3	7.650	0.017	0.787	0.005

Observing the evolution of the summer DMAI (*Fig. 15, Fig. 17, Table 20*) reveals a relative constancy for the analyzed period, with a very slight decrease for Debrecen and a very slight increase for Szeged. No trend is confirmed by the Mann-Kendal trend test (*Table 20*).

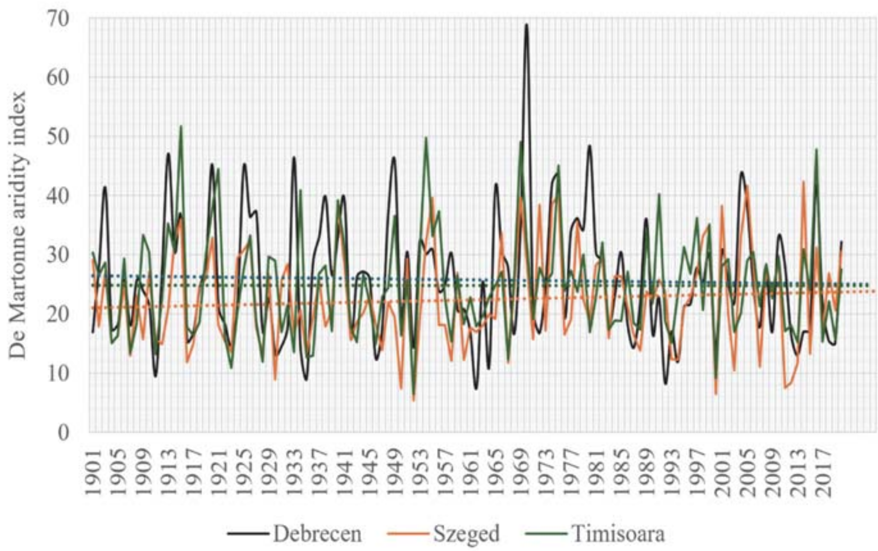

Fig. 15. Summer DMAI trends for the 1901–2020 time period. Dotted lines indicate linear trends.

The autumn DMAI has an average value of 26, with above-average values for Timişoara and Debrecen and below-average values for Szeged (*Table 21*). The lowest average value was calculated for the year 1986 and the highest for 1922. The absolute minimum was calculated for Szeged in 1986 and the absolute maximum for Timişoara in 1905.

Table 21. Evolution of the autumn DMAI for the 1901–2020 time period analyzed by Mann-Kendall trend tests

Station name	Trend equation	Min.	Max.	Mean	Std. deviation	Kendall's tau	p-value	Sen's slope
Debrecen	y= -0.0787x+31.24	4.1	60.2	26.5	4.1	-0.153	**0.014**	-0.072
Szeged	y= -0.0524x+27.636	**3.0**	60.3	**24.5**	3.0	-0.094	0.127	-0.043
Timişoara	y= -0.0278x+28.598	5.4	**62.2**	**26.9**	5.4	-0.026	0.678	-0.011
average	y= -0.053x+29.158	4.2	51.4	26.0	4.2	-0.092	0.137	-0.041

Observing the evolution of the autumn DMAI (*Fig. 16, Fig. 17*, *Table 21*) reveals a decrease for the analyzed period for all three meteorological stations. The Mann-Kendal trend test confirms the evolution trend only for Debrecen (*Table 21*).

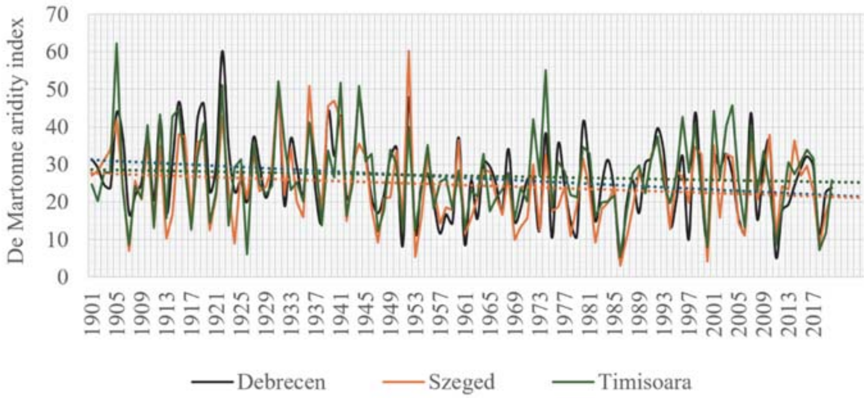

Fig. 16. Autumn DMAI trends for the 1901–2020 time period. Dotted lines indicate linear trends.

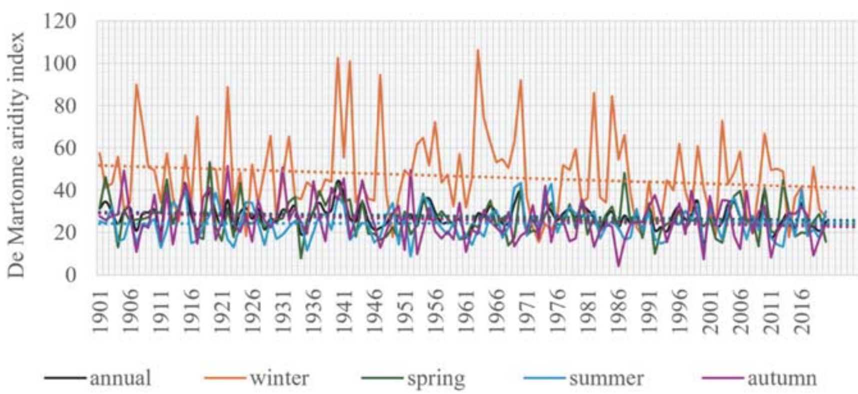

Fig. 17. Annual and seasonal DMAI trends for the 1901–2020 time period as an average for the entire area. Dotted lines indicate linear trends.

4. Conclusions

A synthesis of preceding pages leads to the conclusion that the annual values of the DMAI for the 1951–2020 time period place the studied region at the borderline of the humid and semi-humid zones. The spatial distribution of DMAI is directly related to the configuration of the Pannonian Basin, with DMAI values increasing towards the margins of the plain, as identified also by *Gavrilov et al.* (2020) in Hungary and Vojvodina, the increase of DMAI being caused by the increasing precipitation amounts. Accordingly, the meteorological stations closer to the mountainous area are classified as humid, while those at greater distances are classified as semi-humid. The temporal variability of this parameter reveals a certain constancy of the DMAI for the analyzed time period, with slight decreasing or increasing trends for certain meteorological stations not confirmed by the MK test. This consistency comes amid a clear increasing trend in temperatures and a slight increasing trend in precipitation amounts. The majority of years can be classified as humid and semi-humid, with only one arid year (2000 in Szeged) and no extremely humid years (*Table 22*). High values of the DMAI were calculated for the years 1955, 1970, 1974, 1999, 1999, 2005, and especially 2010, years with the highest amounts of precipitation and generally below-average temperatures, while low values were calculated for the years 1961, 1983, 2011, and especially 2000, dry years.

Table 22. Classification of years according to the DMAI for the 1951–2020 time period

	Station name	Number of years with:					
		$I < 10$ (arid)	$10 \leq I < 20$ (semi-arid)	$20 \leq I < 24$ (mediterranean)	$24 \leq I < 28$ (semi-humid)	$28 \leq I < 35$ (humid)	$35 \leq I < 55$ (very-humid)
1.	Satu Mare	-	1	6	15	35	13
2.	Oradea	-	2	9	18	27	14
3.	Arad	-	4	12	18	28	8
4.	Timişoara	-	4	8	25	22	11
5.	Debrecen	-	4	17	22	21	6
6.	Szeged	1	13	17	21	14	4
7.	Zrenjanin	-	8	14	16	27	5
8.	Vršac	-	2	13	14	25	16
	average	-	3	14	16	29	8

Considering a longer time period, 1901–2020, slightly higher values of the DMAI can be observed at the analyzed meteorological stations, as well as an increased proportion of semi-humid, humid and very-humid years to the detriment of semi-arid and mediterranean years and a decreasing trend of the DMAI, confirmed only for Debrecen by the MK test. The decreasing trend of the DMAI comes amid an increasing trend in temperatures and a decrease in precipitation amounts. In addition to the years mentioned in the previous paragraph, the years

1915 and 1919, with high amounts of precipitation, and especially 1940, with significantly below-average temperatures and high amounts of precipitation, are characterized by high values of the DMAI, while 1934, a dry year with above-average temperatures, is characterized by low values of the DMAI.

Table 23. Classification of years according to the DMAI for the 1901–2020 time period

	Station name	**Number of years with:**					
		I < 10 (arid)	10 ≤ I < 20 (semi-arid)	20 ≤ I < 24 (mediterranean)	24 ≤ I < 28 (semi-humid)	28 ≤ I < 35 (humid)	35 ≤ I < 55 (very-humid)
1.	Debrecen	-	7	25	30	41	17
2.	Szeged	1	21	25	34	31	8
3.	Timişoara	-	6	13	41	40	20
	average	-	4	24	26	52	14

Regarding the DMAI values for the winter months, during the 1951–2020 time period, they place the studied region in the very-humid zone, even extremely humid, if we talk about Satu Mare, with notable differences between the highest (Satu Mare) and the lowest (Szeged) values. On the background of decreasing precipitation amounts and increasing temperatures, the temporal dynamics of the DMAI reveals a decrease of this parameter for the analyzed time interval, for all the analyzed meteorological stations, the MK test only partially confirming these trends. High values of the DMAI can be observed in 1963, 1964 and 1985, years characterized by extremely cold winters, as well as in 1970, a year characterized by a particularly humid winter, and low values in 1990, 2014, and especially in 1973, the year with the driest winter of the analyzed interval.

A consideration of the 1901–2020 time period reveals that, although the graph displays a clear decrease in the DMAI values, this downward trend is not confirmed by the MK test. The analyzed stations belong to the very-humid zone, and in addition to the years listed in the previous paragraph, high values of the DMAI were calculated for the years 1940, 1942, 1947, years characterized by extremely cold winters, 1907 and 1922, and low values of the DMAI for the years 1925 and 1949, years characterized by dry winters.

The DMAI values for the spring months, for the 1951–2020 time interval, place the region in the semi-humid type, with four meteorological stations belonging to this category, three meteorological stations (Vršac, Satu Mare, Oradea) to the humid zone and one to the mediterranean zone (Szeged). The increase in temperatures for the spring season is balanced by a slight increase in precipitation amounts, so that the DMAI remains relatively constant for this period. The years 1987, a year characterized by a cold and rainy spring, 1970 and 2013, years characterized by high precipitation amounts in spring, stand out with high values of the DMAI, while the years 1992, 1968, and 2003, years with dry springs, stand out with low values.

For the 1901–2020 time period, the spring DMAI values are slightly higher, with a decreasing trend for the analyzed interval, which comes on the background of increasing temperatures and decreasing precipitation amounts; the MK test confirms this decrease only for Szeged. The analyzed meteorological stations belong to the semi-humid (Debrecen and Szeged) and humid (Timișoara) category, in addition to the years listed in the previous paragraph, standing out with high values of the DMAI the years 1902, 1919, 1940, years characterized by cold and rainy springs, 1912 and 1924, years with rainy springs, and with low values of the DMAI the years 1904, a year characterized by a dry spring, and, especially 1934, a year with a dry and particularly hot spring.

The DMAI values for the summer months, for the 1951–2020 time interval, place the region in the semi-humid type, except for the meteorological stations Vršac belonging to the humid type and Szeged to the mediterranean type. Similar to the spring months, the increase in temperatures for the summer season is compensated by a slight increase in precipitation amounts, so that the DMAI remains relatively constant for this period. High DMAI values were calculated for 1975, a year characterized by a rainy and cool summer, and low values for 2000, 1952, 1962 and 2003, years with dry summers.

Regarding the 1901-2020 time period, the picture is not significantly different, with slightly lower summer DMAI values for Timișoara and Szeged and a relatively constant trend. In addition to the years previously referenced, 1915, a year characterized by a rainy summer, stands out with a high value of the DMAI, while 1935, 1911, 1923, 1928, and 1950, years with dry summers, with low values of the DMAI.

The DMAI values for the autumn months, for the 1951–2020 time interval, place the region in the semi-humid type, except for the Szeged and Debrecen meteorological stations, which belong to the mediterranean type. On the background of the increase in both temperature and precipitation amounts, an increasing trend of the DMAI can be observed, a trend confirmed by the MK test only for Satu Mare. The years 1952, 1974, and 2007, years characterized by rainy and cold autumns, stand out with high values of the DMAI, while the years 1986, 2011, 2000, and 1953, years with dry autumns, stand out with low values.

The picture is different if we refer to the 1901-2020 time period, in the sense that all three meteorological stations belong to the semi-humid type, and the trend of the DMAI, confirmed by the MK test only for Debrecen, is decreasing, the amount of precipitation being also on a decreasing trend. In addition to the years previously referenced, the years 1922, 1931, 1905, 1941, 1944, 1936, 1915, etc., years characterized by high amounts of precipitation in autumn and generally low temperatures, stand out with high values of the DMAI, while with low values, the most notable year was 1907, a year with a dry autumn.

As a final conclusion, it can be stated that, in the area under study, although the temperatures increased during the 1951–2020 time period, this increase was compensated by a slight increase in precipitation amounts, so that we cannot talk about an aridization of the climate during the last 70 years, only, at most, an aridization of the winter months. Considering the 1901–2020 time period, we can conclude that the increase in temperature, combined with a decrease in precipitation amounts, has led to a slight aridization of the climate, a trend partly confirmed by the MK test. However, it should be noted that the small number of meteorological stations used in the study for this time period limits the consistency of these conclusions, which cannot be extended to the entire study area. In fact, the limitations of this study stem mainly from the lack of longer measurement series for meteorological stations covering the entire study area, as well as from the difficult access to meteorological measurements done in recent decades in the eastern part of the study area, a graphical representation of the spatial distribution of DMAI being difficult to achieve under these conditions. A correlation with other studies conducted in the Pannonian Plain indicates at most some minor differences, which are largely due to the slightly different time intervals covered by these studies.

References

Baltas, E., 2007: Spatial distribution of climatic indices in northern Greece. *Meteorological Applications 14*, 69–78. https://doi.org/10.1002/met.7

Berecz, E., 1901, 1902: Az orsz. m. kir. meteorológiai és földmágnességi intézet temesvár-gyárvárosi meteorológiai és zivatarmegfigyelő állomásának időjárási jelentései. *Természettudományi Füzetek. A Délmagyarországi Természettudományi Társulat Közlönye XXV, XXVI.* (in Hungarian)

Berecz, E., 1902b: Temesvár klimája. *Természettudományi Füzetek. A Délmagyarországi Természettudományi Társulat Közlönye XXVI/IV*, 121 – 127. (in Hungarian)

Berecz, E., 1903–1910: A m. kir. orsz. meleorologiai és földmágnességi intézet temesvári meteorologiai és szeizmológiai obszervatóriumának időjárási jelentései. *Természettudományi Füzetek. A Délmagyarországi Természettudományi Társulat Közlönye XXVII–XXXIV.* (in Hungarian)

Berecz, E., 1904: A m. kir. orsz. meteorológiai és földmágnességi intézet temesvári meteorológiai és szeizmológiai obszervatóriumának közleményei. *Természettudományi Füzetek. A Délmagyarországi Természettudományi Társulat Közlönye XXVIII*, 15 – 25. (in Hungarian)

Berecz, E., 1905: Temesvár időjárása az 1904. évben. *Természettudományi Füzetek. A Délmagyarországi Természettudományi Társulat Közlönye XXIX*, 76 – 88. (in Hungarian)

Berecz, E., 1906: A Temesvári meteorologiai és szeizmológiai Observatorium időjárási jelentése az 1905. évről. *Természettudományi Füzetek. A Délmagyarországi Természettudományi Társulat Közlönye XXX*, 21 – 41. (in Hungarian)

Berecz, E., 1907: A Temesvári meteorologiai és szeizmológiai Observatorium időjárási jelentése az 1906. évről. *Természettudományi Füzetek. A Délmagyarországi Természettudományi Társulat Közlönye XXXI*, 47 – 72. (in Hungarian)

Berecz, E., 1908: Temesvár időjárása az 1907. évben. *Természettudományi Füzetek. A Délmagyarországi Természettudományi Társulat Közlönye XXXII*, 30 – 52. (in Hungarian)

Berecz, E., 1909: Temesvár időjárása az 1908. évben. *Természettudományi Füzetek. A Délmagyarországi Természettudományi Társulat Közlönye XXXIII/1*, 35 – 59. (in Hungarian)

Berecz, O., 1910–1912: A m. kir. orsz. meleorologiai és földmágnességi intézet temesvári meteorologiai és szeizmológiai obszervatóriumának időjárási jelentései. *Természettudományi Füzetek. A Délmagyarországi Természettudományi Társulat Közlönye XXXIV–XXXVI.* (in Hungarian)

Berecz, O., 1911: Temesvár időjárása az 1910. évben. *Természettudományi Füzetek. A Délmagyarországi Természettudományi Társulat Közlönye XXXV,* 26 – 43. (in Hungarian)

Berecz, O., 1912: Temesvár időjárása az 1911. évben. *Természettudományi Füzetek. A Délmagyarországi Természettudományi Társulat Közlönye XXXVI,* 11 – 28. (in Hungarian)

Berecz, O., 1913: Temesvár időjárása az 1912. évben. *Természettudományi Füzetek. A Délmagyarországi Természettudományi Társulat Közlönye XXXVII,* 210 – 226. (in Hungarian)

Berecz, O., 1913–1917: Időjárási jelentések a magyar király országos meleorológiai és földmágnességi intézet temesvári meteorologiai és szeizmológiai obszervatóriumától. *Természettudományi Füzetek. A Délmagyarországi Természettudományi Társulat Közlönye XXXVII–XLI*. (in Hungarian)

Berecz, O., 1915: Temesvár időjárása az 1914. évben. *Természettudományi Füzetek. A Délmagyarországi Természettudományi Társulat Közlönye XXXIX,* 62 – 73. (in Hungarian)

Comisia Naţională pentru Statistică, 1990 – 1999: Anuarul statistic al României. (in Romanian)

Croitoru, A.E., Piticar, A., Imbroane, A.M., and *Burada, D.C.*, 2013: Spatiotemporal distribution of aridity indices based on temperature and precipitation in the extra-Carpathian regions of Romania. *Theor. Appl. Climatol. 112*, 597–607. https://doi.org/10.1007/s00704-012-0755-2

Deniz, A., Toros, H., and *Incecik, S.*, 2011: Spatial variations of climate indices in Turkey. *Int. J. Climatol. 3,* 394–403. https://doi.org/10.1002/joc.2081

Direcţia Centrală de Statistică, 1961 – 1989: Anuarul statistic al R.P.R./R.S.R. (in Romanian)

Dudaş, M., 2025: Evoluţia în timp a hazardurilor meteo-climatice şi impactul lor asupra societăţii în Câmpia Banatului. *Editura Universităţii de Vest din Timişoara*, p.444. (in Romanian)

Dudaş, M., Urdea, P., 2023: Considerations regarding the evolution of extreme temperatures in the Banat Plain in the last six decades. *Időjárás*, *127/3*, 347 – 377. https://doi.org/10.28974/idojaras.2023.3.5

Ehmann, T., 1918: Időjárási jelentések a magyar király országos meleorologiai és földmágnességi intézet temesvári meteorologiai és szeizmológiai obszervatóriumától. *Természettudományi Füzetek. A Délmagyarországi Természettudományi Társulat Közlönye XLII,* 56 – 76. (in Hunfarian)

Gavrilov, M.B., Marković, S.B., Jarad, A., and Korać, V.M., 2015: The analysis of temperature trends in Vojvodina (Serbia) from 1949 to 2006. *Thermal Sci. 19,* 339 – 350. https://doi.org/10.2298/TSCI150207062G

Gavrilov, M. B., Tosić, I., Marković, S. B., Unkasević, M., and *Petrović, P.,* 2016: The analysis of annual and seasonal temperature trends using Mann Kendall test in Vojvodina, Serbia. *Időjárás 120/2*, 183 – 198.

Gavrilov, M.B., An, W.; Xu, C., Radaković, M.G., Hao, Q., Yang, F., Guo, Z., Perić, Z., Gavrilov, G., and *Marković, S.B.*, 2019: Independent Aridity and Drought Pieces of Evidence Based on Meteorological Data and Tree Ring Data in Southeast Banat, Vojvodina, Serbia. *Atmosphere 2019*, *10*, 586. https://doi.org/10.3390/atmos10100586

Gavrilov, M.B., Radaković, M.G., Sipos, G., Mezősi, G., Gavrilov, G., Lukić, T., Basarin, B., Benyhe, B., Fiala, K., Kozák, P., Perić, Z.M., Govedarica, D., Song, Y., and *Marković, S.B.*, 2020: Aridity in the Central and Southern Pannonian Basin. *Atmosphere 2020, 11*, 1269. https://doi.org/10.3390/atmos11121269

Gocić, M. and *Trajković, S.*, 2012: Analysis of changes in meteorological variables using Mann-Kendall and Sen's slope estimator statistical tests in Serbia. *Global and Planetary Change 100,* 172 – 182. http://dx.doi.org/10.1016/j.gloplacha.2012.10.014

Hrnjak, I., Lukić, T., Gavrilov, M.B., Marković, S.B., Unkašević, M., and *Tošić, I.*, 2014: Aridity in Vojvodina, Serbia. *Theor. Appl. Climatol. 2014, 115*, 323–332. https://doi.org/10.1007/s00704-013-0893-1

Hungarian Meteorological Service (HungaroMet Magyar Meteorológiai Szolgáltató), 2022, 2025: Climate – Climate of Hungary – Climate Data Series 1901-2020 – Szeged/Debrecen – Data. https://www.met.hu/ (accessed 8 February 2022 and 7 January 2025).

Institutul Meteorologic Central al României, 1921 – 1930: *Buletinul lunar al Observaţiunilor Meteorologice din România*, Seria II, Anul I – X, No. 1 – 12, Tip. Ionescu/Copuzeanu, Bucureşti. (in Romanian)

Institutul Meteorologic Central al României, 1931 – 1947: *Buletinul lunar al observaţiunilor meteorologice din România*, Seria III, Anul I – XVII, Imprimeria Centrală / Naţională, Bucureşti. (in Romanian)
Institutul Meteorologic Central al României, 1948 – 1950: *Buletinul lunar al observaţiunilor meteorologice din R.P.R.*, Seria IV, An I – III, Intreprinderea Poligrafică, Bucureşti. (in Romanian)
Institutul Meteorologic Central al României, 1951, 1952: *Buletinul lunar al observaţiunilor meteorologice din R.P.R.*, Seria V, Anul I, II, Intreprinderea Poligrafică, Bucureşti. (in Romanian)
Institutul Meteorologic Central al României, 1953 – 1959: *Buletinul lunar al observaţiilor meteorologice din R.P.R.*, Seria VII, An I–VII, Intreprinderea Poligrafică, Bucureşti. (in Romanian)
Institutul Naţional de Statistică, 2000 – 2021: Anuarul statistic al României. (in Romanian)
Kiss, A., Szabó, P., and *Pongrácz, R.*, 2023: Spatial and temporal analysis of drought-related climate indices for Hungary for 1971–2100. *Hungarian Geographical Bulletin 72*, 223–238 https://doi.org/10.15201/hungeobull.72.3.2
Moral, F.J., Paniagua, L.L., Rebollo, F.J., and *García-Martín, A.*, 2017: Spatial analysis of the annual and seasonal aridity trends in Extremadura, southwestern Spain. *Theor. Appl. Climatol. 130,* 917–932. https://doi.org/10.1007/s00704-016-1939-y
Milentijević, N. M., Valjarević, A., Bačević, N. R., Ristić, D., Kalkan, K., Cimbaljević, M., Dragojlović, J., Savić, S., and Pantelić, M., 2022: Assessment of observed and projected climate changes in Bačka (Serbia) using trend analysis and climate modeling. *Időjárás, 126/1*, 47 – 68. https://doi.org/10.28974/idojaras.2022.1.3
Nistor, M.M., 2016: Spatial distribution of climate indices in the Emilia-Romagna region. *Meteorological Applications 23*, 304–313. https://doi.org/10.1002/met.1555
Regional Meteorological Center Banat–Crișana (Centrul Meteorologic Regional Banat–Crişana), 2022: meteorological data
Republic Hydrometeorological Service of Serbia (Republički hidrometeorološki zavod Srbije Srbije RHMZ), 1949 – 2020: *Meteorological Yearbook – Climatological Data*. http://www.hidmet.gov.rs/ (accessed 26 December 2021).
Réthly, A., 1918: Temesvár régi hőmérsékleti megfigyelései 1780. Szeptember – 1803. December, *Természettudományi Füzetek. A Délmagyarországi Természettudományi Társulat Közlönye*, *XLII*, 27 – 43. (in Hungarian)
Réthly, A., 1970: *Időjárási események és elemi csapások Magyarországon 1701-1800-ig,* Akadémiai Kiadó, Budapest. (in Hungarian)
Réthly, A., 1998: *Időjárási események és elemi csapások Magyarországon 1801-1900-ig,* Országos Meteorológiai Szolgálat, Budapest. (in Hungarian)
Tošić, I., Hrnjak, I., Gavrilov, M.B., Unkašević, M., Marković, S.B., and *Lukić, T.*, 2014: Annual and seasonal variability of precipitation in Vojvodina. *Theor. Appl. Climatol. 117*, 331–341. https://doi.org/10.1007/s00704-013-1007-9
Vlăduţ, A.Ș. and *Licurici, M.*, 2020: Aridity conditions within the region of Oltenia (Romania) from 1961 to 2015. *Theor.Appl.Climatol.140*, 589–602. https://doi.org/10.1007/s00704-020-03107-5
XLSTAT Statistical Software & Data Analysis Add-on for Excel, https://www.xlstat.com/en/ (accessed on 20 April 2025).

DOI:10.28974/idojaras.2026.3.3

IDŐJÁRÁS

Quarterly Journal of the HungaroMet Hungarian Meteorological Service
Vol. 130, No. 3, July – September, 2026, pp. 273–296

Spatiotemporal assessment of drought under historical and projected scenarios in the Himalayan region of Uttarakhand, India

Shubhika Goel*, Shivani Kothijal, and **Raj Kumar Singh**

Department of Agricultural Meteorology, Govind Ballabh Pant University
Pantnagar-263145, Uttarakhand, India

** Corresponding author Email: shubhikagl@gmail.com*

(Manuscript received in final form on December 20, 2025)

Abstract— Mountainous regions such as Uttarakhand, India, are highly vulnerable to climate change owing to their complex terrain and dependence on climate-sensitive agriculture. This study analyzes spatiotemporal variability of rainfall and agricultural droughts across Kumaon and Garhwal using historical records (1901–2022) and climate projections (2023–2100) under SSP2-4.5 and SSP5-8.5 moderate and high green-house gas emissions scenarios. Results reveal substantial intra-regional disparities: annual rainfall historically ranged from 1203 mm in rain-shadow zones (Almora, Tehri) to 1930 mm in Himalayan-facing districts (Pithoragarh, Chamoli). Projections suggest up to 20% rainfall increase in Pithoragarh and Chamoli, with little change in Almora and Tehri. Drought analysis shows late-season droughts in the historically dominant agricultural monsoon period Karif (spanning from June to October), particularly in Udham Singh (US) Nagar and Chamoli. Future projections indicate declining severe but more persistent moderate Kharif droughts (e.g., US Nagar 20.9%, Champawat 19%). Conversely, Rabi season (spanning from October to March) droughts are projected to intensify in high-altitude districts: Pithoragarh (20 years, ~11.5 weeks), Dehradun (16 years, ~13.5 weeks), threatening wheat and mustard yields with >40–50% losses. Late-season droughts also remain recurrent in Nainital (26 years) and Uttarkashi (27 years). Overall, Kumaon's vulnerability stems from persistent Kharif droughts, while Garhwal faces prolonged Rabi droughts (up to 14 weeks). These findings highlight the need for district- and season-specific adaptation strategies, focusing on climate-resilient crops and improved water management.

Key-words: agricultural drought, climate sensibility, historical data, projections

1. Introduction

Drought is a complex and multifaceted extreme weather event characterized by varying durations and severity levels, with far-reaching impacts on the environment, agriculture, economy, and society. The scientific understanding of drought—its origin, development, and eventual cessation—remains challenging due to its occurrence across all climatic zones in diverse forms, intensities, and time scales (*Mishra* and *Singh*, 2010). In India, droughts are known to cause substantial economic losses annually, significantly affecting GDP, with the extent of impact depending on the drought category (e.g., mild, moderate, or severe). Recent years have witnessed an upward trend in extreme climatic events, partly driven by anthropogenic activities. Land use changes, over-extraction of water resources, and other human interventions disrupt the hydrological cycle, contributing to the frequency and intensity of such events. The propagation of drought is influenced by a complex interplay of factors, including temperature, precipitation, evapotranspiration, humidity, climatic patterns, land use practices, and topography, making its prediction and comprehensive understanding difficult (*Wilhite* and *Glantz*, 1985). Drought is broadly categorized into four types: (1) *meteorological drought*, marked by prolonged periods of below-normal precipitation; (2) *agricultural drought*, characterized by insufficient soil moisture to support crop growth; (3) *hydrological drought*, indicated by reduced surface and subsurface water flows; and (4) *socio-economic drought*, which arises when water scarcity begins to affect human activities and the economy (*Das et al.*, 2022).

Ensuring food security in any region necessitates effective monitoring and prediction of natural disasters such as droughts, as they can significantly disrupt agricultural productivity (*CV et al.*, 2024). When meteorological drought advances into agricultural drought, it leads to reduced soil moisture and adversely impacts crop yields, potentially resulting in food shortages (*Hameed et al.*, 2020). As drought progresses from atmospheric conditions to the agricultural landscape, the competition for already limited water resources intensifies—particularly in developing nations, where agriculture is among the most vulnerable sectors. In India, drought poses a significant threat, increasing crop susceptibility to both biotic and abiotic stresses. This has made the country one of the most drought-prone regions globally. Studies estimate that drought affects approximately 68% of India's agricultural land, with 33% of this area identified as "chronically drought-prone" (*Kaur et al.*, 2022; *Goel et al.*, 2025; *Goel* and *Singh*, 2025). Among the key drivers of soil moisture stress is a deficiency in precipitation, which underscores the importance of examining the transition from meteorological to agricultural drought (*Li et al.*, 2022).

The Shared Socioeconomic Pathways (SSPs) used in climate modeling to represent different future scenarios based on socioeconomic development and emission trends. SSP2-4.5, known as the "Middle of the Road" scenario, envisions a future with moderate challenges to mitigation and adaptation, featuring stable economic growth, moderate population increase, and gradual technological progress. It assumes moderately successful emission reductions, leading to a stabilization of radiative forcing at 4.5 W/m² by 2100 and a projected global temperature rise of 2.1–3.5°C above pre-industrial levels. In contrast, SSP5-8.5, or the "Fossil-fueled Development" scenario, anticipates rapid economic growth driven primarily by fossil fuels with minimal climate mitigation, resulting in extremely high emissions. This leads to a radiative forcing of 8.5 W/m² by 2100 and a potential temperature increase of 3.3–5.7°C, posing severe risks to the global climate system due to intensified warming and associated impacts.

Uttarakhand's climate is diverse, influenced by its varied topography, with the plains experiencing a subtropical climate with hot summers (up to 40°C) and mild winters (5–15°C) and heavy monsoon rains (1000–1500 mm annually). The middle Himalayas have a temperate climate with moderate summers (15–25°C), cold winters (0–10°C) and significant monsoon rainfall (1500–2000 mm), plus occasional snowfall. In the high Himalayas, the climate ranges from alpine to tundra, with cool summers (5–15°C), very cold winters (below -10°C) and moderate rainfall (500–1000 mm) with heavy snowfall. The monsoon season from June to September brings most of the annual rainfall, critical for agriculture, while higher altitudes receive substantial winter snowfall, crucial for glaciers. However, the region faces natural challenges like floods, landslides, cloudbursts, and avalanches, impacting agriculture and local livelihoods.

The purpose of this study is to analyze both historical (1901–2022) and future (2023–2100) drought scenarios to better understand the spatial and temporal dynamics of drought in the region. By using rainfall deviation, the study aims to assess meteorological drought and examine its transition into agricultural drought during both the Kharif and Rabi seasons. Future projections are evaluated under two shared socioeconomic pathways: SSP2-4.5, representing a moderate emission scenario, and SSP5-8.5, representing a high emission scenario to assess the potential impact of climate change on drought patterns. This comprehensive assessment is intended to support strategic planning for climate-resilient agriculture and effective drought risk management.

2. Materials and methods

2.1 Study area

Uttarakhand, in northern India, spans 53,483 km², situated between the 28°43' N to 31°27' N latitudes and 77°33' E to 81°02' E longitudes. It shares borders with Tibet (China) to the north, Nepal to the east, Uttar Pradesh to the south, and Himachal Pradesh to the west. As of the 2011 Census, its population was around 10 million, with recent estimates suggesting it has grown to approximately 11 million. The state is largely rural, with about 70% of the population living in rural areas and 30% in urban areas Key cities include Almora, Dehradun (the capital and most populous city), Haldwani, Haridwar, Mussoorie, and Nainital (see *Table 1*). Uttarakhand is divided into two regions: Garhwal and Kumaon, each with distinct cultural and geographic characteristics.

Table 1. Latitude, longitude, and elevation of districts in Kumaon and Garhwal regions of Uttarakhand

	Districts	**Latitude**	**Longitude**	**Elevation**
	Kumaon region			
1	Almora	29.59	79.65	1648.8
2	Bageshwar	29.84	79.77	972.9
3	Champawat	29.34	80.09	1653.5
4	Nainital	29.39	79.45	2084.0
5	Pithoragarh	29.58	80.22	1645.0
6	US Nagar	28.96	79.52	550.0
	Garhwal region			
1	Chamoli	30.46	79.87	1062.6
2	Dehradun	30.32	78.03	652.2
3	Haridwar	29.95	78.16	249.7
4	Pauri Garhwal	29.87	78.84	886.2
5	Rudraprayag	30.29	78.98	895.0
6	Tehri Garhwal	30.38	78.47	1750.0
7	Uttarkashi	30.73	78.44	1158.0

2.2. Global climate model selection

MIROC6 (Model for Interdisciplinary Research on Climate version 6) is a global climate model developed by the Atmosphere and Ocean Research Institute, University of Tokyo, the National Institute for Environmental Studies (NIES), and the Japan Agency for Marine-Earth Science and Technology (JAMSTEC). MIROC6 operates at a spatial resolution of approximately 1.4° latitude by 1.4° longitude. This coarse resolution means that each grid cell covers an area of about 155 kilometers by 155 kilometers near the equator. The resolution varies with latitude due to the Earth's curvature. The effective climate sensitivity (ECS) of MIROC6 is estimated to be 2.6 K (*Shiomaga et al.*, 2023). MIROC6 model had been selected for futuristic meteorological data analysis, because it performed best for the Indian conditions with correlation coefficient of 0.87 to 0.97 (*Jose et al.*, 2022; *Sardar et al.*, 2023).

2.3. Softwares used

2.3.1. Weather Cock

It is a software developed by the AICRPAM Unit of CRIDA, Hyderabad for agroclimatic analysis, thus, different agroclimatic analyses, converting daily rainfall data into weekly and annual data, as well as meteorological and agricultural drought analyses are possible using this software. This particular software is based on Visual Basic (VB) and easy to operate even for beginners. Doing agroclimatic analysis with MS Excel for individual stations is drudgery and may lead to wrong results. The weathercock software reduces this drudgery and eliminates any mistakes associated with MS-Excel. Moreover, batch processing a special provision in the weathercock to facilitate analysis for hundreds of stations at a moment if input files are prepared in the said format as doing agroclimatic analysis at localized scale have hundreds / thousands of stations (*Sikdar et al.*, 2020).

2.3.2. Spyder

All preprocessing and statistical downscaling of IMD historical (rainfall and maximum/minimum temperature) and MIROC6 (CMIP6) future climate scenarios under SSP2-4.5 and SSP5-8.5 were performed in Python (v3.11) using the Spyder IDE (v5.x, Anaconda distribution) on Windows 10/Ubuntu 22.04 with ≥16 GB RAM. Spyder’s integrated workspace facilitated efficient handling of large NetCDF datasets, supported by scientific libraries such as xarray, netCDF4, dask, xclim, xesmf, scikit-learn, matplotlib, cartopy and others.

2.4. Climate data collection

2.4.1. Historical data

The historical climate data for India were obtained from the India Meteorological Department (IMD) Gridded Data Portal (https://www.imdpune.gov.in/), which provides quality-controlled, homogenized, and spatially interpolated datasets in NetCDF(.nc), Binary(.grd), and Text (.txt) formats for research and analysis. The portal offers daily gridded rainfall data at a spatial resolution of 0.25° × 0.25° covering the period 1901–2022. For this study, daily rainfall datasets corresponding to the study region (Uttarakhand) were extracted and processed for further analysis and downscaling.

2.4.2. *Future data*

The future climate projections, along with the corresponding historical simulations, were obtained from the Copernicus Climate Data Store (CDS) of the European Centre for Medium-Range Weather Forecasts (ECMWF), accessible at https://climate.copernicus.eu/. The CDS provides free, quality-controlled, and standardized climate datasets from multiple sources, including reanalysis products (e.g., ERA5), satellite observations, and climate model outputs from the Coupled Model Intercomparison Project Phase 6 (CMIP6) under various SSP scenarios. Users can access daily, monthly, and seasonal variables, such as precipitation, temperature, humidity, wind speed, and pressure, at different spatial resolutions and time periods, in NetCDF format.

For this study, daily precipitation data simulated by the MIROC6 global climate model at a horizontal resolution of 1.4° × 1.4° were downloaded for both the historical baseline period (1985–2014) and the projected future period (2015–2100) under SSP2-4.5 and SSP5-8.5 scenarios. The common observed and simulated data period (2015–2022) was used for calibration, and the performance was evaluated by calculating bias, Nash-Sutcliffe efficiency (NSE) and root mean square error (RMSE) for maximum temperature (Tmax), minimum temperature (Tmin), and rainfall. These datasets were used to evaluate the model skill in reproducing historical climate patterns over Uttarakhand and to assess projected changes for the future periods (2023–2100) in comparison with observed IMD gridded data.

2.5. *Climate data conversion and analysis*

The rainfall data, sourced from IMD (historical data spanning 1901-2022) and the Copernicus Climate Data Store (simulated data from 2015-2100), were converted from NetCDF (network common data form) files to CSV (comma separated values) format. These data were then downscaled using the Spyder software (a Python package) for the 13 districts of Uttarakhand. This process ensured the data was in a usable format for detailed analysis and application in regional climate studies.

MIROC6 model predict the meteorological data based on the shared socio-economic pathway (SSP) emission scenarios SSP2-4.5 and SSP5-8.5.

2.6. *Calibration of the meteorological data*

The accuracy of the bias-corrected monthly mean data for maximum and minimum temperatures, as well as average rainfall, across 13 districts, was assessed by comparing it with observed data from the period 2015-2022, which is consistent for both datasets. There are different measures used to verify and to have the agreement between observed and predicted value.

2.6.1. Bias

Bias indicates the average difference between the observed values and the calculated (modeled) values. It shows whether the model tends to overestimate (if the value is negative) or underestimate (if the value is positive) the observations. To obtain the average bias over a period:

$$Bias = 1/N \sum_{i=1}^{N} (Oi - Si),$$

where N is the number of observations, Oi is the observed value, and Si is the modeled value

2.6.2. Root mean square error (RMSE)

RMSE is the square root of the MSE. It provides a measure of the magnitude of the error, giving more weight to larger errors:

$$RMSE = \sqrt{1/N \sum_{i=1}^{N} (Oi - Si)^2}\,.$$

2.6.3. Nash-Sutcliffe efficiency (NSE)

The Nash-Sutcliffe efficiency is used to assess the predictive power of hydrological models, but it can be applied to other types of models as well. The NSE is defined as:

$$NSE = 1 - \frac{\sum_{i=1}^{N} (Oi - Si)^2}{\sum_{i=1}^{N} (Oi - \bar{O})^2}\,.$$

– $NSE = 1$ means perfect match between observed and predicted values,
– $0 < NSE < 1$ means acceptable model performance. The closer the NSE to 1, the better the model is,
– $NSE=0$ means that the model predictions are as accurate as the mean of the observed data, and
– $NSE<0$ means that he model is worse than using the mean of the observed data.

Table 2. Statistical parameters for monthly mean meteorological data under the two SSP scenarios of Uttarakhand

Statistical parameters	**Max. temperature (°C)**		**Min. temperature (°C)**		**Rainfall (mm)**	
	SSP 2-4.5	**SSP 5-8.5**	**SSP 2-4.5**	**SSP 5-8.5**	**SSP 2-4.5**	**SSP 5-8.5**
Bias	-1.18	-0.87	-0.06	0.00	-6.36	0.31
RMSE	1.38	1.22	0.62	0.52	17.40	17.13
NSE	0.93	0.95	0.99	0.99	0.98	0.98

The statistical evaluation of MIROC6 model outputs against observed IMD data for 13 districts of Uttarakhand during 2015–2022 indicates good model performance for monthly Tmax, Tmin, and rainfall (*Table 2*). Bias values were close to zero for Tmin and rainfall, while Tmax showed a slight underestimation (–1.18 to –0.87 °C). The RMSE values were relatively low (≤1.38 °C for temperature and ~17 mm for rainfall), suggesting small deviations from observations. High NSE values (>0.90 across all variables) further confirm the strong predictive capability of MIROC6. Overall, the model effectively captures the monthly variability of temperature and rainfall, making it suitable for climate projection studies in Uttarakhand.

2.7. Bias correction of modeled data

To mitigate the biases in the modeled data, various bias correction methods have been developed, all dependent on the quality of observational datasets used. Effective bias correction relies on robust observation data, especially crucial for correcting extreme precipitation events, necessitating long-term datasets. The Delta Change method, widely used in climate impact research, adjusts observations based on GCM or RCM projections. Rainfall adjustments typically involve calculating percentage changes: a 20% increase in modeled rainfall would mean multiplying historical data by 1.2 for future projections, with different adjustments for various seasons or months. Notably, this method does not address changes in climate variability, such as increased extreme rainfall frequency or prolonged dry spells.

In the initial phase of the study, future meteorological data on rainfall projected by MIROC6 was downscaled for 13 districts of Uttarakhand. This simulated baseline data was compared against observed baseline meteorological data from IMD gridded datasets to establish correction factors. These correction factors were then applied to the futuristic data to refine and derive the correction factors. Subsequently, the expected changes in rainfall were analyzed during the 21st century across various locations in the state.

The deviation percentage method for bias correcting rainfall involves adjusting historical rainfall data by a percentage deviation calculated from climate model projections. Here’s a step-by-step outline of how this method is typically applied:

a. *Calculate the deviation percentage*: The method determines the percentage of deviation of simulated future rainfall projections from historical observations. This is often calculated as:

$$\text{deviation percentage} = (R_{model} - R_{historical})/R_{historical}) \times 100\%,$$

where R_{model} is the rainfall projected by the climate model and $R_{historical}$ is the simulated historical rainfall data.

b. *Apply the deviation percentage:* In this step, the method adjusts the historical rainfall data by adding or subtracting the calculated deviation percentage to obtain bias-corrected future rainfall data:

For an increase in rainfall: corrected rainfall = $R_{observed} \times (1+\text{deviation }\%)$

For a decrease in rainfall: corrected rainfall = $R_{observed} \times (1-\text{deviation }\%)$

The agroclimatic analysis viz., converting daily rainfall data into weekly and annual data, meteorological and agricultural drought analysis was possible using the WeatherCock software.

2.8. Drought and its classification

Drought is a normal, recurrent climatic feature that occurs around the world causing huge loss to the farming community. Drought is universally acknowledged as a phenomenon associated with deficiency of rainfall. Droughts occur at random and there is no periodicity in its occurrence thus, it cannot be predicted in advance. In semiarid stations, the occurrence of rainfall is seasonal and is known more for its variability with respect to space and time. Drought is characterized by moisture deficit resulting either from i) below normal rainfall, ii) erratic rainfall distribution, iii) higher water need, or iv) a combination of all the three factors.

2.8.1. Meteorological drought

A period of prolonged dry weather condition due to below normal rainfall. According to the India Meteorological Department, there are two types of meteorological drought based on rainfall deficit from normal. Based on the daily rainfall data as input file in the Weathercock software, it gives the output in % deviation of rainfall of the particular year. The criteria for the meteorological drought have been presented in the *Table 3*.

Table 3. Criteria of meteorological drought condition (IMD)

Deviation (%)	Drought condition
-25 and above	no drought
-25 to -50	moderate drought
< -50	severe drought

2.8.2. Agricultural drought

Agricultural impacts due to short-term precipitation shortages, temperature anomaly causes increased evapotranspiration and soil water deficits that could adversely affect crop production. According to the National Commission on

Agriculture, 1976, at least four consecutive weeks receiving less than half of the normal rainfall during the Kharif season and six such consecutive weeks during the Rabi season is considered as agricultural drought period based on weekly rainfall as input file. Normal rainfall: Average rainfall for a location/region over a period of years (preferable 30years)
(https://www.ipcc.ch/report/ar6/syr/resources/spm-headline-statements/).

In agroclimatic analysis, meteorological and agricultural drought study is important. The frequencies of occurrence of different type of meteorological droughts (moderate and severe) over a period of year would give insight for vulnerability of a particular location/region to drought on annual basis. Agricultural drought analysis would give idea about susceptibility of a region to drought on seasonal basis, i.e., main crop growing season. India is a monsoon-dependent nation for agriculture, with most of its precipitation occurring during the south-west monsoon season.

The drought classification was carried out on the basis of standard meteorological weeks (SMWs), which represent fixed weekly intervals used in agroclimatic analyses. For the Kharif season, agricultural droughts were categorized into three critical periods based on the crop growth stages (*Gupta et al.*, 2022): early-season drought (SMW 22–28: germination to early vegetative stage), mid-season drought (SMW 29–35: active vegetative to flowering stage), and late-season drought (SMW 36–42: grain filling to maturity stage). This classification enables differentiation between drought events that impact crop establishment, vegetative growth, and yield formation phases.

For historical analysis (1901–2022), drought occurrence was evaluated for the Kharif season in all districts of the Kumaon and Garhwal regions. For future projections (2023–2100) under SSP2-4.5 and SSP5-8.5 scenarios, the drought analysis included both the Kharif season (SMW 22–42) and the Rabi season (SMW 44–60) to assess potential impacts across the region’s major cropping periods.

2.8.3. Duration of weeks

The duration of agricultural drought was calculated using the Weathercock software, wherein the standard meteorological weeks (SMWs) indicating drought occurrence were identified. Drought events for Kharif or Rabi season could last for 1, 2, 3, or 4 consecutive weeks. For each year, the range of drought weeks was determined based on the observed minimum and maximum durations. Subsequently, the average duration was computed for all 13 districts of Uttarakhand, both for the historical period and under future scenarios, using weekly rainfall data.

3. *Results*

3.1. Kumaon region of Uttarakhand

3.1.1. Historical rainfall trend

During the historical period (1901–2022), Kumaon's annual rainfall ranged from 1203 mm in Almora to nearly 1930 mm in Pithoragarh. Pithoragarh (1930 mm) and Bageshwar (around 1780 mm) consistently received the highest rainfall due to orographic uplift, ensuring adequate water availability for paddy and maize during the Kharif season. Nainital, with ~1700 mm, showed high intra-district variation linked to altitudinal gradients, often influencing apple and horticultural crop production in upper elevations versus paddy in the lower valleys. Almora (1203 mm) and Champawat (around 1260 mm), both in partial rain-shadow zones, received comparatively less rainfall, frequently causing stress in unirrigated maize and pulses. US Nagar (Tarai plains) maintained relatively stable rainfall (~1400–1500 mm), sufficient for rice–wheat cropping systems under irrigated conditions (*Fig. 1*).

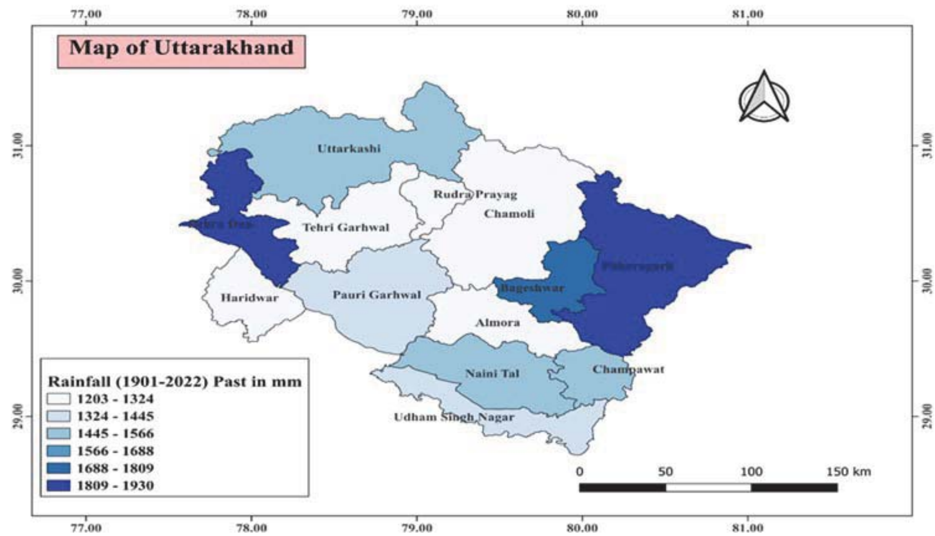

Fig. 1. The rainfall map for both the Kumaon and Garhwal region of Uttarakhand in the historical periods (1901–2022).

3.1.2. Historical drought trend

During the 1901–2022 period, Kumaon experienced several meteorological droughts, with moderate drought years dominating. US Nagar and Champawat each recorded 19 years of moderate droughts (~15.6% of total years), significantly impacting rice and maize yields. Severe droughts were rare but still notable in Almora and Pithoragarh (4 years each, ~3.3%). Almora, despite 111 no-drought years (91%), faced yield variability in rainfed maize due to its exposure to short but impactful droughts (*Table 4*; *Fig. 2*).

Table 4. Frequency and intensity of meteorological and agricultural droughts in Kumaon region of Uttarakhand for Historical periods (1901–2022)

Districts	Meteorological Drought				Agricultural Drought					
	No Drought (years)	Moderate Drought (years)	Severe Drought (years)	Total Drought (years)	Early Drought (22-28)		Mid Drought (29-35)		Late Drought (36-42)	
					Freq.#	Dur.#	Freq.	Dur.	Freq.	Dur.
Almora	111	07	04	11	15	4-7 (4.83)	10	4-8 (5.55)	35	4-9 (5.22)
Bageshwar	103	16	03	19	15	4-7 (4.56)	08	4-9 (4.83)	25	4-7 (4.83)
Champawat	99	19	04	23	13	4-10 (5.07)	06	4-7 (4.67)	40	4-9 (5.38)
Nainital	105	16	01	17	15	4-6 (4.53)	04	4-5 (4.40)	42	4-9 (5.20)
Pithoragarh	105	13	04	17	12	4-7 (4.58)	04	4-10 (5.88)	25	4-7 (4.79)
US Nagar	99	19	04	23	28	4-7 (4.90)	12	4-9 (4.86)	13	4-9 (5.32)

Freq. = Frequency of the drought in years, Dur. = Duration of the weeks in the form of range and value in parathesis represents the average number of weeks (Standard Meteorological Week no.)

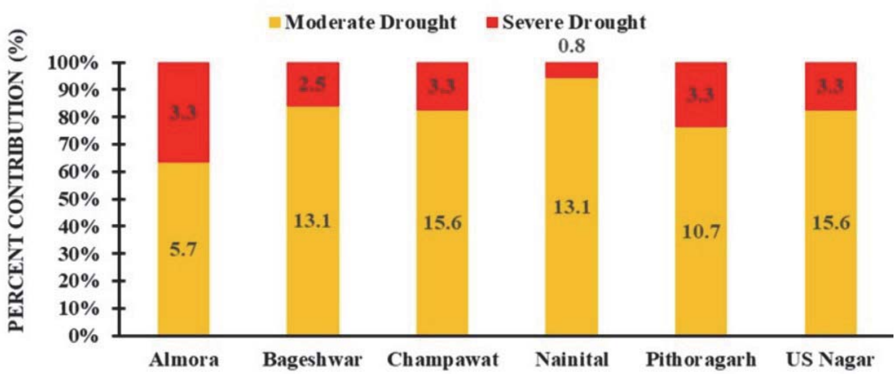

Fig. 2. Percentage share of moderate and severe meteorological droughts in Kumaon region of Uttarakhand for historical periods (1901–2022)

Agricultural droughts were most frequent during the late Kharif season (SMW 36–42). Nainital and Champawat were the worst affected with 42 and 40 late-season drought years, respectively, often coinciding with maize grain filling and rice maturity stages—critical periods for yield. US Nagar faced 28 early drought years, affecting rice transplanting and maize germination. Almora reported 15 early droughts and 10 mid-season droughts, frequently affecting rainfed pulses and millets (*Table 4; Fig. 3*).

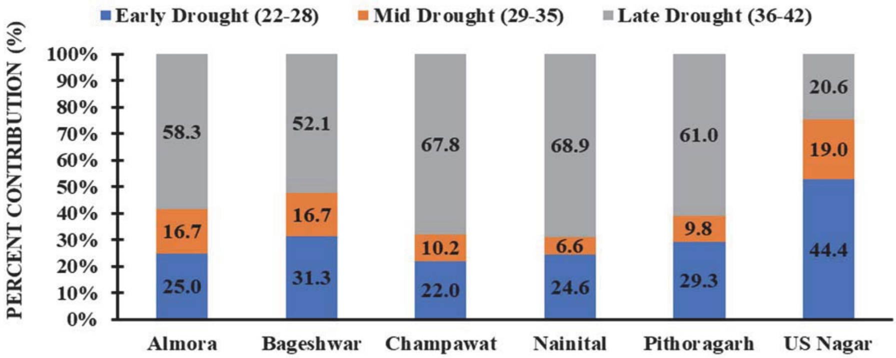

Fig. 3. Percentage share of early, mid and late monsoon season agricultural drought in Kumaon region of Uttarakhand for historical periods (1901–2022)

Drought duration in Kumaon ranged between 4–10 weeks. On average, early-season droughts lasted ~4.5 weeks, mid-season droughts ~5 weeks, and late-season droughts stretched up to ~5.5 weeks, often extending into September. These longer late-season droughts coincided with the reproductive phases of maize and rice, leading to significant yield losses in unirrigated fields. For instance, yield losses of 20–30% were reported in drought-prone upland maize areas of Almora and Champawat during prolonged late-season dry spells (*Table 4; Fig. 4*).

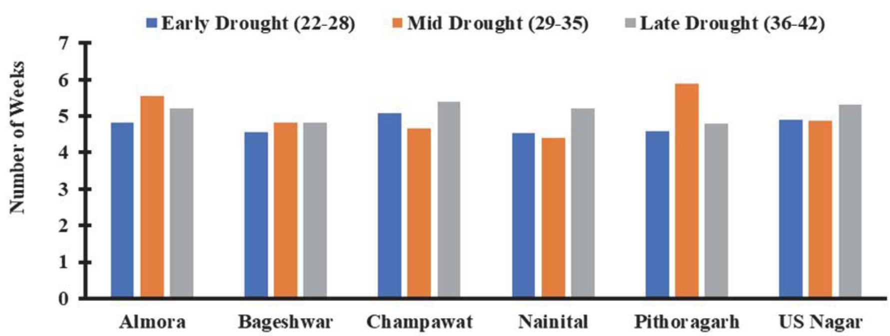

Fig. 4. Duration of early, mid and late monsoon season agricultural drought in Kumaon region of Uttarakhand for historical periods (1901–2022)

3.1.3. Future rainfall trend

Under SSP 2-4.5, rainfall in Kumaon increases significantly, with Pithoragarh projected at ~2382 mm (+23% increase from baseline). Bageshwar and Nainital also show increases of ~15–20%, improving prospects for paddy and maize but raising risks of excess rainfall and lodging. Almora and Champawat show modest gains (~8–10%). Under SSP 5-8.5, wetter conditions intensify, with US Nagar expected to reach ~2241 mm, which may benefit double-cropping but also increase flooding in the Tarai plains (*Figs. 5* and *6*).

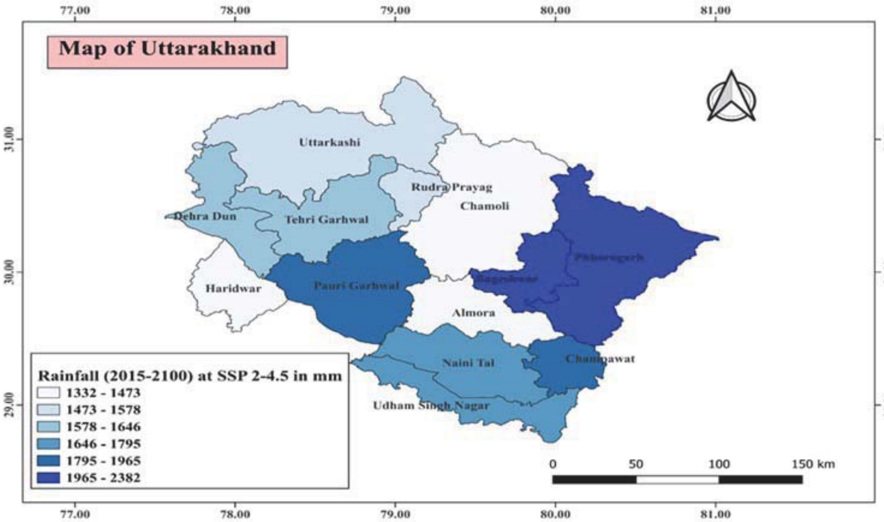

Fig. 5. The rainfall map for both the Kumaon and Garhwal region of Uttarakhand in the future periods (2023–2100) at SSP 2-4.5

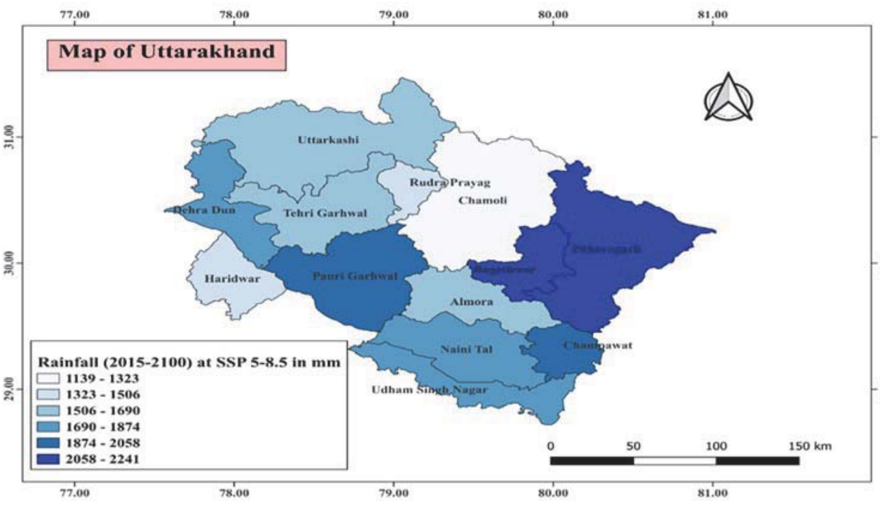

Fig. 6. The rainfall map for both the Kumaon and Garhwal region of Uttarakhand in the future periods (2023–2100) at SSP 5-8.5

3.1.4. *Future drought trend*

Future projections (2023–2100) show zero severe drought years across Kumaon districts, suggesting improved resilience. However, moderate droughts persist, especially in US Nagar and Champawat (16 years each, ~19% of total years), which may intermittently reduce Kharif crop productivity despite overall wetter conditions (*Table 5*; *Fig. 7*).

Table 5. Frequency and intensity of meteorological and agricultural drought in Kumaon region of Uttarakhand for Future Scenarios (2023–2100)

Districts	Meteorological Drought				Agricultural Drought							
					Kharif Drought						Rabi Drought	
	No Drought (years)	Moderate Drought (years)	Severe Drought (years)	Total Drought (years)	Early Drought (22-28)		Mid Drought (29-35)		Late Drought (36-42)			
					Freq.#	Dur.#	Freq.	Dur.	Freq.	Dur.	Freq.	Dur.
Almora	74	04	0	04	11	4-5 (4.45)	04	4-6 (5.25)	21	4-6 (4.82)	-	-
Bageshwar	62	14	2	16	12	4-7 (5.64)	05	4-8 (6.25)	13	4-7 (5.23)	11	6-17 (8.67)
Champawat	62	16	0	16	10	4-5 (4.25)	05	4-5 (4.57)	20	4-6 (4.75)	-	-
Nainital	66	12	0	12	11	4-6 (4.91)	03	8(8)	26	4-8 (5.18)	-	-
Pithoragarh	65	13	0	13	05	5-7 (6.20)	10	4-9 (6.69)	11	4-7 (5.05)	20	6-21 (11.45)
US Nagar	62	16	0	16	10	4-6 (4.73)	04	4(4)	20	4-8 (5.22)	-	-

Freq. = Frequency of the Drought in years, Dur. = Duration of the weeks in the form of range and value in parathesis represents the average number of weeks (Standard Meteorological Week no.)

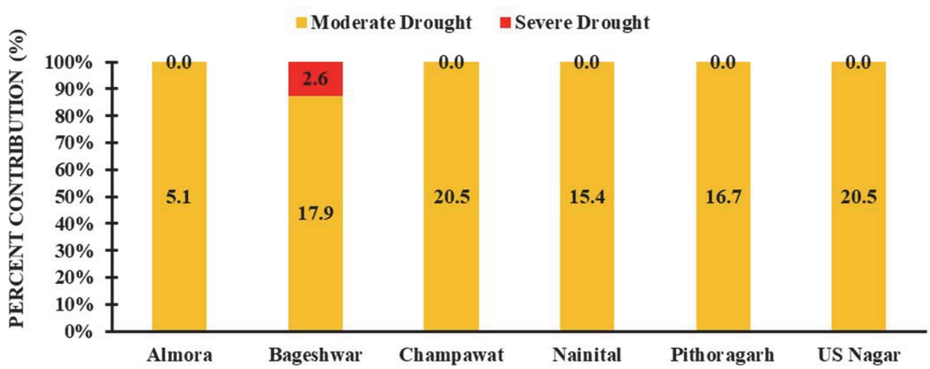

Fig. 7. Percentage share of moderate and severe meteorological droughts in Kumaon region of Uttarakhand for future scenarios (2023–2100)

Agricultural droughts remain concentrated in the late Kharif season, with Nainital projected for 26 late-season drought years (~30% of study years) and Champawat for 20 years. Such droughts directly coincide with rice maturity and maize cob formation. Importantly, Rabi droughts emerge in the future, particularly in Pithoragarh (20 years, avg. duration 11.5 weeks) and Bageshwar (11 years), potentially threatening wheat and mustard yields (*Table 5; Fig. 8*).

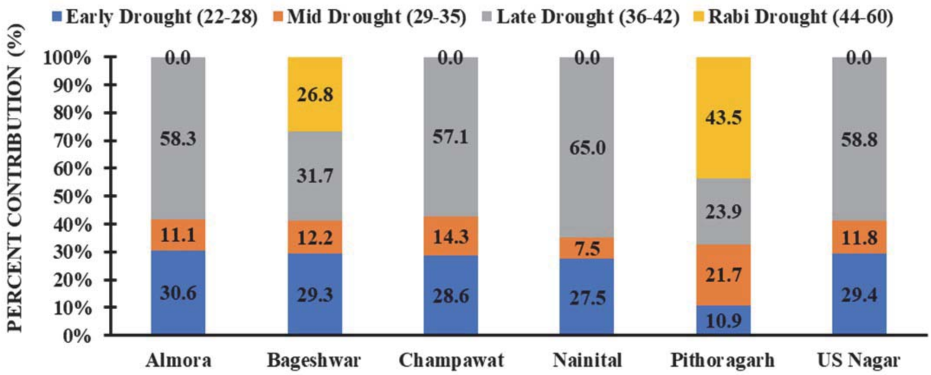

Fig. 8. Percentage share of early, mid, late monsoon and Rabi season agricultural drought in Kumaon region of Uttarakhand for future scenarios (2023–2100)

Future drought durations vary widely from 4–21 weeks. Kharif droughts remain moderate in length (4–8 weeks), but Rabi droughts extend much longer. Pithoragarh reports an average Rabi drought length of ~11.5 weeks, long enough to disrupt the entire wheat growth cycle, potentially reducing yields by >40% in unirrigated areas (*Table 5; Fig. 9*).

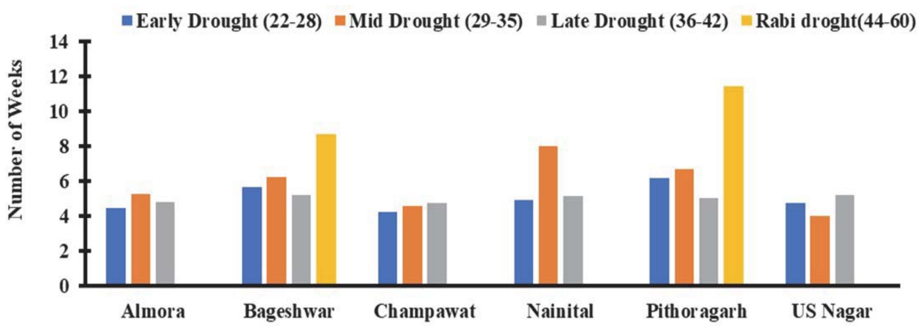

Fig. 9. Duration of early, mid, late monsoon and Rabi season agricultural drought in Kumaon region of Uttarakhand for future scenarios (2023–2100)

3.2. Gharwal region of Uttarakhand

3.2.1. Historical rainfall trend

Garhwal's rainfall during 1901–2022 varied from 1203 mm (Tehri) to 1930 mm (Chamoli, Uttarkashi). Chamoli and Uttarkashi, with their high-altitude locations, benefitted from heavy monsoonal rains, ensuring sufficient water for paddy and finger millet. Dehradun (~1500 mm) and Haridwar (~1450 mm) maintained stable rainfall for rice–wheat systems. Tehri and Pauri Garhwal, with <1300 mm, frequently faced dry spells, often reducing maize and pulse yields in upland regions (*Fig. 1*).

3.2.2. Historical drought trend

Rudraprayag reported the highest meteorological drought frequency (16 years, 13.1%), while Chamoli had the lowest (9 years, 7.4%). Severe droughts were rare, with Pauri Garhwal reporting the maximum (5 years, 4.1%), often coinciding with maize tasseling and paddy reproductive stages, leading to substantial yield deficits (*Table 6; Fig. 10*).

Table 6 Frequency and intensity of meteorological and agricultural drought in Garhwal region of Uttarakhand for Historical periods (1901–2022)

Districts	Meteorological Drought				Agricultural Drought					
	No Drought (years)	Moderate Drought (years)	Severe Drought (years)	Total Drought (years)	Early Drought (22-28)		Mid Drought (29-35)		Late Drought (36-42)	
					Freq.#	Dur.#	Freq.	Dur.	Freq.	Dur.
Chamoli	113	09	0	09	11	4-6 (4.57)	03	4-7 (5.75)	39	4-8 (5.00)
Dehradun	103	17	02	19	16	4-7 (4.44)	09	4-5 (4.33)	33	4-9 (5.16)
Haridwar	107	15	0	15	24	4-7 (4.62)	04	4-5 (4.25)	27	4-8 (5.11)
Pauri Garhwal	101	16	05	21	18	4-8 (5.06)	09	4-6 (4.60)	34	4-8 (5.36)
Rudraprayag	106	14	02	16	23	4-7 (4.76)	04	4-9 (5.18)	38	4-9 (5.29)
Tehri Garhwal	103	15	04	19	15	4-7 (4.74)	09	4-9 (5.33)	37	4-9 (5.30)
Uttarkashi	103	17	02	19	09	4-7 (4.71)	10	4-7(4.75)	32	4-7 (5.13)

Freq. = Frequency of the Drought in years, Dur. = Duration of the weeks in the form of range and value in parathesis represents the average number of weeks (Standard Meteorological Week no.)

Agricultural droughts were heavily late-season dominated. Chamoli, Tehri, and Rudraprayag reported 39, 37, and 38 late-season drought years, respectively, affecting maize and rice at maturity. Early droughts were frequent in Haridwar (24 years) and Rudraprayag (23 years), often disrupting rice transplanting. Such frequent early droughts in Haridwar forced farmers to delay rice sowing, reducing yields by 15–20% (*Table 6; Fig. 11*). Droughts lasted 4–9 weeks, with late-season droughts averaging ~5.3 weeks. Early and mid-season droughts were shorter (~4–6 weeks). The shorter but frequent early droughts coincided with germination and transplanting, leading to crop failure in rainfed maize fields (*Table 6; Fig. 12*).

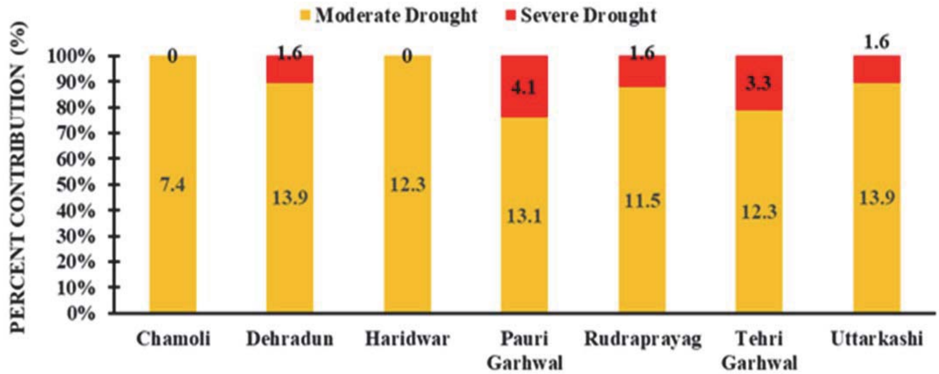

Fig. 10. Percentage share of moderate and severe meteorological droughts in Garhwal region of Uttarakhand for historical periods (1901–2022).

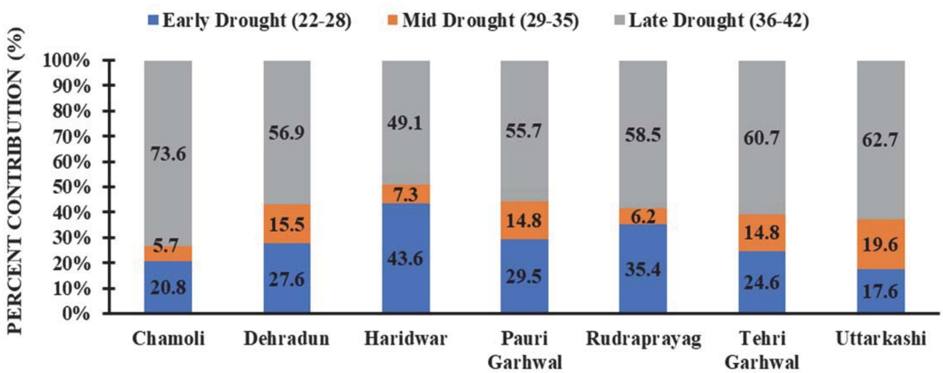

Fig. 11. Percentage share of early, mid and late monsoon season agricultural drought in Garhwal region of Uttarakhand for historical periods (1901–2022).

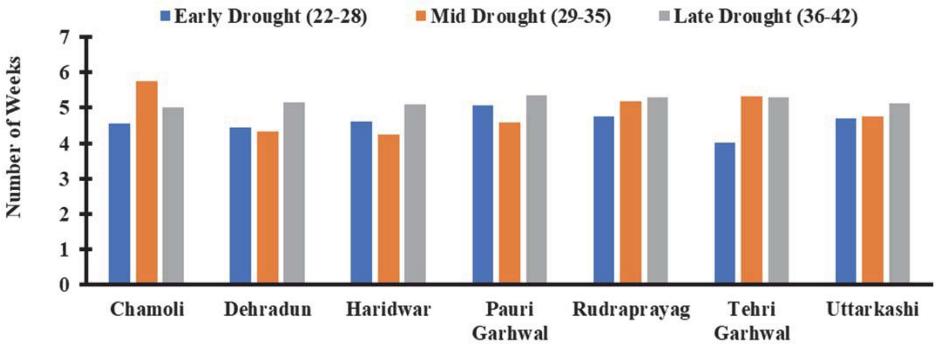

Fig. 12. Duration of early, mid and late monsoon season agricultural drought in Garhwal region of Uttarakhand for historical periods (1901–2022).

3.2.3. Future rainfall trend

Projections under SSP 2-4.5 indicate rainfall increases across Garhwal, with Chamoli projected to exceed 2200 mm (+15%). Rudraprayag also shows gains, supporting maize–paddy systems. Dehradun and Haridwar show ~10% increases, beneficial for rice–wheat cropping. However, Tehri and Pauri continue to lag behind with smaller increments, leaving some areas vulnerable to moisture stress. Under SSP 5-8.5, rainfall intensifies, particularly in Chamoli, Uttarkashi, and Dehradun, raising risks of localized flooding during Kharif (*Figs. 5* and *6*).

3.2.4. Future drought trend

Severe droughts nearly disappear, except in Uttarkashi (3 years, ~3.5%). Moderate droughts persist, especially in Haridwar (13 years, ~15%) and Tehri Garhwal (10 years). These may disrupt rice transplanting and reduce maize yields intermittently (*Table 7; Fig. 13*). Late-season droughts remain the most prominent, with Uttarkashi (27 years) and Tehri Garhwal (24 years) showing the highest frequency. Early and mid-season droughts are less common but notable in Chamoli and Rudraprayag. Importantly, Rabi droughts emerge in Dehradun (16 years, ~19%) and Uttarkashi (6 years), directly threatening wheat and mustard production (*Table 7; Fig. 14*). Future droughts last 4–15 weeks. Kharif droughts average 4–7 weeks, while Rabi droughts extend much longer—Dehradun (~13.5 weeks) and Uttarkashi (~14 weeks). Such prolonged dry spells overlap with critical wheat growth phases (tillering–grain filling), risking >50% yield loss in unirrigated regions (*Table 7; Fig. 15*).

Table 7. Frequency and intensity of meteorological and agricultural drought in Garhwal region of Uttarakhand for Future Scenarios (2023–2100)

Districts	Meteorological Drought				Agricultural Drought							
					Kharif Drought						Rabi Drought	
	No Drought (years)	Moderate Drought (years)	Severe Drought (years)	Total Drought (years)	Early Drought (22-28)		Mid Drought (29-35)		Late Drought (36-42)			
					Freq.#	Dur.#	Freq.	Dur.	Freq.	Dur.	Freq.	Dur.
Chamoli	75	03	0	03	13	4-5 (4.36)	03	6(6)	21	4-7 (4.82)	-	-
Dehradun	73	05	0	05	05	4-5 (4.56)	04	5(5)	18	4-7 (4.82)	16	6-15 (13.45)
Haridwar	65	13	0	13	12	4-5 (4.55)	03	5(5)	24	4-7 (4.91)	-	-
Pauri Garhwal	69	09	0	09	12	4-7 (4.67)	09	4-5 (4.43)	19	4-7 (5.29)	-	-
Rudraprayag	69	09	0	09	12	4-6 (4.50)	08	4-6 (4.40)	20	4-7 (5.06)	-	-
Tehri Garhwal	68	10	0	10	11	4-5 (4.27)	06	4-5 (4.50)	24	4-7 (5.06)	-	-
Uttarkashi	73	02	03	05	04	4-6 (4.85)	11	4-6 (5.00)	27	4-7 (4.86)	06	14(14)

Freq. = Frequency of the Drought in years, Dur. = Duration of the weeks in the form of range and value in parathesis represents the average number of weeks (Standard Meteorological Week no.)

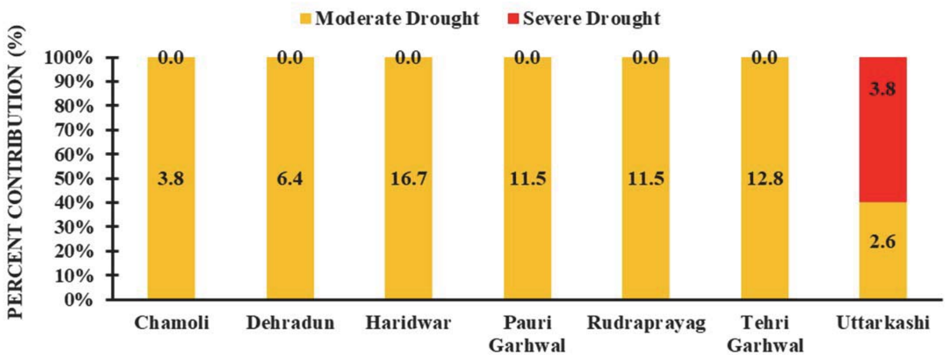

Fig. 13. Percentage share of moderate and severe meteorological droughts in Garhwal region of Uttarakhand for future scenarios (2023–2100).

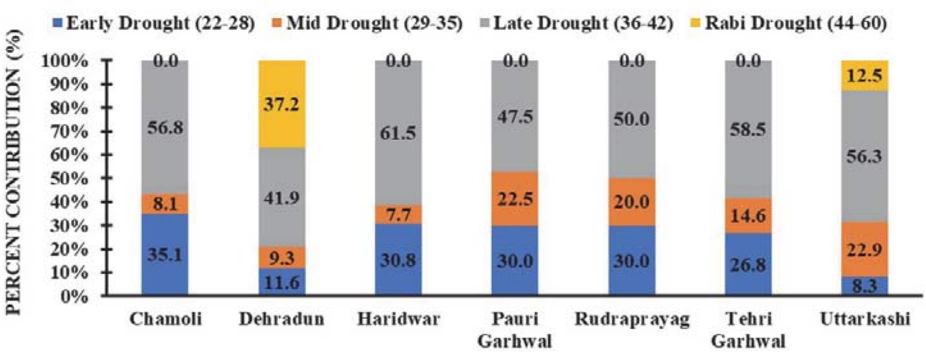

Fig. 14. Percentage share of early, mid, late monsoon and Rabi season agricultural drought in Garhwal region of Uttarakhand for future scenarios (2023–2100).

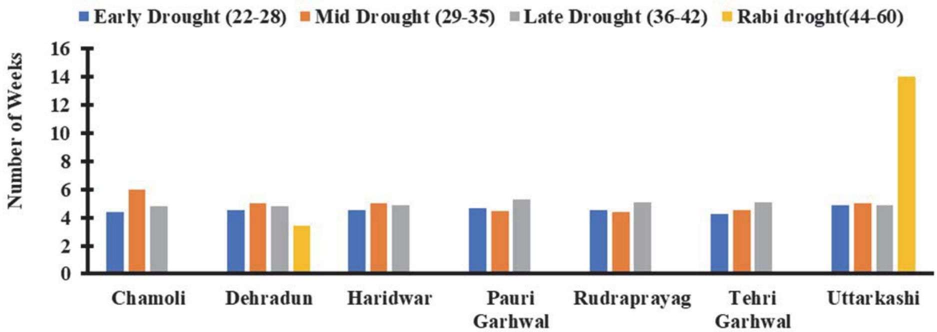

Fig. 15. Duration of early, mid, late monsoon and Rabi season agricultural drought in Garhwal region of Uttarakhand for future scenarios (2023–2100).

3.3. A comparative analysis from historical and future perspective of drought in Kumaon and Gharwal regions

3.3.1. Historical perspective

Historically, Kumaon had fewer no-drought years compared to Garhwal. Almora and Bageshwar reported 91.0% and 84.4% no-drought years, whereas Chamoli and Haridwar recorded 92.6% and 87.7%, respectively. Severe droughts were more frequent in Pauri Garhwal (4.1%), whereas Kumaon districts rarely exceeded 3%. Agricultural droughts were consistently late-season dominated in both regions, but Garhwal had higher frequency and persistence. For example, Chamoli had 39 late-season droughts vs. Nainital's 42, yet also suffered more early droughts (11) compared to Nainital (15), amplifying stress on maize and rice systems. Overall, Garhwal displayed slightly greater vulnerability due to multi-season drought exposure (*Tables 4* and *6*).

3.3.2. Future perspective

In the future, severe droughts decline significantly, with Kumaon reporting none and Garhwal only Uttarkashi at 3.5%. However, moderate droughts persist, more in Kumaon (US Nagar 20.9%, Bageshwar 19.8%) than Garhwal (Chamoli 3.5%, Uttarkashi 3.5%). The emergence of Rabi droughts is a key shift, more severe in Garhwal (Dehradun 16 years, Uttarkashi 6 years) than Kumaon (Pithoragarh 20 years, Bageshwar 11 years), threatening wheat-based systems. Duration of droughts is projected to be longer in Garhwal (up to 14 weeks) than Kumaon (up to 11.5 weeks), raising risks of prolonged stress during crop critical stages. This suggests that Kumaon will face moderate drought persistence in Kharif crops, while Garhwal will be more vulnerable in Rabi crops, requiring region-specific adaptation strategies for rice–maize and wheat–mustard systems (*Tables 5* and *7*; *Figs. 9* and *15*).

4. *Discussion*

This spatiotemporal assessment of rainfall and drought patterns across Kumaon and Garhwal (1901–2022 historical; 2015–2100 projected) reveals distinct climatic trends and regional contrasts. Historically, annual rainfall varied from 1203 mm in Almora to 1930 mm in Pithoragarh, driven largely by orographic effects. Himalayan-facing districts like Pithoragarh, Bageshwar, Chamoli, and Uttarkashi consistently received higher precipitation, whereas interior and leeward districts such as Almora, Champawat, Tehri Garhwal, and Pauri Garhwal faced rain-shadow effects. Under future climate scenarios (SSP 2-4.5 and SSP 5-8.5), rainfall is expected to increase across most districts up to 15–20% in high-altitude regions such as Pithoragarh and Chamoli—signaling intensified monsoonal activity. However, this increase will not be uniform; marginal gains of only 5–8% are projected for Almora, Tehri Garhwal, and Champawat, indicating that spatial heterogeneity in rainfall will persist. The study on meteorological and agricultural drought conditions and their dynamic relationships during the pre-monsoon season (March–May) in northwest Bangladesh was conducted by *Al Shoumik et al.* (2023). A similar study was carried out by *Verma et al.* (2023), which examined the severity and frequency of meteorological drought under two climate change scenarios—Shared Socioeconomic Pathway (SSP2-4.5 and SSP5-8.5) over Indian conditions. *Sivan* and *Pramada* (2024) investigated the spatiotemporal characteristics of historic and future droughts over a monsoon-dominated humid region (Kerala) in India. *Gupta et al.* (2022) carried out a block-level characterization of agricultural and meteorological drought in Hazaribagh district using 35 years (1983–2017) of daily rainfall data based on IMD criteria. The study revealed considerable spatial variability in the intensity and frequency of drought across different blocks of the district. The drought trends in the state give similar results where the results reveal a historical predominance of late-season Kharif droughts (SMW 36–42), especially in US Nagar, Nainital, Rudraprayag, and Chamoli. Between 1901 and 2022, these districts experienced 10–15 years of severe or moderate late-season droughts. Future projections indicate a decline in the frequency of severe drought years (from an average of 7–10 per district in the 20th century to 2–4 in the 21st century), with a corresponding rise in moderate drought episodes. Meanwhile, Rabi season droughts historically negligible are projected to increase, particularly in high-altitude districts like Pithoragarh and Uttarkashi, where 6–9 Rabi drought years are anticipated under SSP 5-8.5. This emerging seasonal shift poses a challenge to conventional crop calendars and water allocation practices. The aim is to provide actionable advisories to farmers regarding optimal sowing dates and cropping patterns in response to projected climate variability.

5. Conclusion

Historically, Kumaon and Garhwal have shown distinct spatial and temporal rainfall–drought dynamics. Orographically favored districts such as Pithoragarh, Bageshwar, Chamoli, and Uttarkashi consistently received higher precipitation, while in leeward districts like Almora, Champawat, Tehri, and Pauri, the rainfall-deficit persisted. Droughts were predominantly late in the Kharif season in both regions, adversely affecting maize and rice at reproductive stages, with Garhwal displaying slightly greater vulnerability due to its exposure to multi-season droughts. Moderate droughts occurred frequently in US Nagar, Champawat, and Rudraprayag, while severe droughts, though infrequent, occasionally disrupted agricultural productivity in rainfed areas. Future projections indicate an overall increase in rainfall, more pronounced in Himalayan-facing districts (15–20%) compared to modest increments in rain-shadow areas (5–10%). Severe droughts are projected to decline; however, moderate droughts will continue to occur, particularly in Kumaon's US Nagar and Champawat. Importantly, the historically negligible Rabi droughts are expected to emerge, with Garhwal (Dehradun, Uttarkashi) facing longer and more severe episodes than Kumaon (Pithoragarh, Bageshwar). Extended drought durations, up to 14 weeks in Garhwal and 11.5 weeks in Kumaon, will pose significant threats to wheat–mustard and rice–maize systems. Consequently, Kumaon is likely to remain more vulnerable during the Kharif season, while Garhwal may face heightened risks in the Rabi season, necessitating region-specific adaptation strategies in crop planning, irrigation scheduling, and water resource management.

Acknowledgements: The authors would like to express their deep and sincere gratitude to the Department of Agrometeorology, GB Pant University of Agriculture & Technology, Pantnagar for extending their guidance, technical assistance and University Fellowship during the study in conducting this research work.

Conflict of Interests: The authors declare that there is no conflict of interest related to this article.

References

Al Shoumik, B. A., Khan, M. Z., and Islam, M. S., 2023: Spatiotemporal characteristics of meteorological and agricultural drought indices and their dynamic relationships during the pre-monsoon season in drought-prone region of Bangladesh. *Environmental Challenges, 11,* 100695. https://doi.org/10.1016/j.envc.2023.100695

CV, A., Pachore, A., and *Remesan, R.,* 2024: Agricultural drought response to meteorological drought over different agroclimatic zones of the Ganga River basin. *Journal of Water and Climate Change, 15(3),* 998-1017. https://doi.org/10.2166/wcc.2024.437

Das, S., Das, J., and *Umamahesh, N.V.,* 2022: Investigating the propagation of droughts under the influence of large-scale climate indices in India. *Journal of Hydrology, 610,*.127900. https://doi.org/10.1016/j.jhydrol.2022.127900
Goel, S., Kothiyal, S., and *Singh, R.K.,* 2025. Variability and trends of rainfall in past and future in Kumaon region of Uttarakhand. *Journal of Agrometeorology, 27(1),* 121-124 https://doi.org/10.54386/jam.v27i1.2855.
Goel, S. and *Singh, R.,* 2025. Assessment of Rainfall Variability and the Impact of Drought on Crop Growth in the Plain and Hill Zones of Uttarakhand, India. *Archives of Current Research International, 25(4),*.170-183. https://doi.org/10.9734/acri/2025/v25i41147
Gupta, C. K., Wadood, A., Kumar, R., Kumari, P., Prasad, S. M., and *Gupta, D. K.,* 2022: Characteristics of Meteorological and Agricultural Drought of Hazaribagh District, Jharkhand. *Journal of Agricultural Physics 22(2),* 284-290.
Hameed, M., Ahmadalipour, A., and *Moradkhani, H.,* 2020: Drought and food security in the middle east: An analytical framework. *Agricultural and Forest Meteorology 281,*.107816. https://doi.org/10.1016/j.agrformet.2019.107816
Jose, D.M. and *Dwarakish, G.S.,* 2022: Ranking of downscaled CMIP5 and CMIP6 GCMs at a basin scale: case study of a tropical river basin on the South West coast of India. *Arabian Journal of Geosciences 15(1),* 120. https://doi.org/10.1007/s12517-021-09289-0
Kaur, L., Rishi, M.S., and *Chaudhary, B.S.,* 2022: Assessment of meteorological and agricultural droughts using remote sensing and their impact on groundwater in an agriculturally productive part of Northwest India. *Agricultural Water Management 274,* 107956. https://doi.org/10.1016/j.agwat.2022.107956
Li, C., Zhang, X., Yin, G., Xu, Y.. and *Hao, F.,* 2022: Evaluation of drought propagation characteristics and influencing factors in an arid region of Northeast Asia (ARNA). *Remote Sensing 14(14),* 3307. https://doi.org/10.3390/rs14143307
Mishra, A.K. and *Singh, V.P.,* 2010: A review of drought concepts. *Journal of hydrology 391(1-2),* 202-216. https://doi.org/10.1016/j.jhydrol.2010.07.012
Sardar, P. and *Samadder, S.R.,* 2023: Long-term ecological vulnerability assessment of Indian Sundarban region under present and future climatic conditions under CMIP6 model. *Ecological Informatics 76,* 102140. https://doi.org/10.1016/j.ecoinf.2023.102140
Shiogama, H., Tatebe, H., Hayashi, M., Abe, M., Arai, M., Koyama, H., Imada, Y., Kosaka, Y., Ogura, T., and *Watanabe, M.,* 2023: MIROC6 Large Ensemble (MIROC6-LE): experimental design and initial analyses. *Earth System Dynamics 14*, 1107–1124
Sikdar, N. K., Patel, S.R., and *Chakraborty, P.P.,* 2020: Studies on rainfall pattern and length of growing period of Raipur district of Chhattisgarh plain agroclimatic zone. *International Journal of Chemical Studies, 8(5),* 1673-1679 https://doi.org/10.22271/chemi.2020.v8.i5w.10538.
Sivan, S. D. and *Pramada, S. K.,* 2024: Spatiotemporal analysis of historic and future drought characteristics over a monsoon dominated humid region (Kerala) in India. *Environment, Development and Sustainability 28*, 473–497 . https://doi.org/10.1007/s10668-024-05004-7
Verma, A., Vishwakarma, A., Bist, S., Kumar, S., and *Bhatla, R.,* 2023: A long-term drought assessment over India using CMIP6 framework: present and future perspectives. *Mausam, 74(4),* 963-972. https://doi.org/10.54302/mausam.v74i4.6198
Wilhite, D. A. and *Glantz, M. H.,* 1985: Understanding: the drought phenomenon: the role of definitions. *Water International 10(3),* 111-120. https://doi.org/10.1080/02508068508686328

DOI:10.28974/idojaras.2026.3.4

IDŐJÁRÁS

Quarterly Journal of the HungaroMet Hungarian Meteorological Service
Vol. 130, No. 3, July – September, 2026, pp. 297–315

Some novel observations of terrain-disrupted airflow at the Hong Kong International Airport based on range-height indicator and plan position indicator scans of the LIDAR and their numerical simulations

Yu Ting Leung, Pak Wai Chan, Man Lok Chong, Chun Kit Ho, Kai Kwong Lai, Ping Cheung, and **Yan Yu Leung**

Hong Kong Observatory,
134A Nathan Road, Kowloon, Hong Kong, China

**Corresponding author E-mail: pwchan@hko.gov.hk*

(Manuscript received in final form on March 18, 2026)

Abstract— Range-height indicator (RHI) scans from the Doppler Light Detection And Ranging (LIDAR) systems at the Hong Kong International Airport (HKIA) reveal vortices associated with Kelvin-Helmholtz (KH) instability, jump-like features and mountain waves associated with lower kills and a gap on Lantau Island nearby HKIA. These novel features of terrain-disrupted airflow at HKIA that has not been documented before. This paper analyzes such flow features by considering some parameters of the airflow based on the upper air sounding in Hong Kong, such as Richardson number, Scorer parameter, and Froude number. An attempt has also been made to simulate these novel flow phenomena at HKIA using a high resolution mesoscale numerical weather prediction (NWP) model. The modeling results are found to be a mixed success. Some features, such as mountain waves and jump-like feature, are readily reproduced. However, vortices associated with KH instability are difficult to reproduce, and the vortex shedding simulation does not fully reproduce the observational data based on the Doppler LIDARs. The results in this paper are considered to be useful for the study of mountain meteorology in Hong Kong and elsewhere in the world.

Key-words: terrain-disrupted airflow, LIDAR, Hong Kong International Airport

1. *Introduction*

HKIA is located just to the northwest of the mountainous Lantau Island, which has peaks as high as 1000 m above sea level and valleys as low as 300 m in between. In stable boundary layer, various kinds of terrain-disrupted airflow features may occur over the airport area, which may be hazardous to the arriving and departing aircraft due to the creation of low-level windshear and turbulence. The terrain-disrupted airflow features are best captured by the LIDAR systems. Since 2002, LIDARs have been gradually introduced to HKIA to capture the terrain-induced airflow disturbances.

With the deployment of more LIDAR units at the airport, different scanning strategies could be implemented to these instruments and recently both plan position indicator (PPI) and range height indicator (RHI) scans of the LIDARs are available every several minutes, in addition to the glide path scans that are primarily used to build up the headwind profiles to be encountered by the aircraft and to alert low-level windshear. In this paper, some novel LIDAR observations of wind features, including vortices associated with KH instability, would be presented, analyzed, and discussed, through depiction of the corresponding LIDAR velocity scans and calculation of atmospheric parameters such as Richardson number based on profiling data. Moreover, an attempt is made to simulate these features using a high resolution mesoscale numerical weather prediction model at large eddy simulation mode, with a spatial resolution as small as 40 metres.

This paper are believed to be useful for studying mountain meteorology in Hong Kong and elsewhere in the world, through documentation of the LIDAR observation, analysis of atmospheric profile, and discussion of numerical simulation. As such, the results in the paper are of academic interest. At the same time, though no windshear or turbulence reports are obtained in these cases, the novel flow features are also considered to be of practical importance as they may lead to fluctuations of the airflow to be encountered by the aircrafts in an operating airport.

2. *Materials and methods*

2.1. Meteorological instrumentation

The major meteorological instrument considered in this paper is the Doppler LIDAR. There is runway specific LIDAR installation at HKIA, i.e., one LIDAR is installed near the centre of each of the three parallel runways of the airport. In this paper, the scans from the LIDAR at the second runway, i.e., HKG2 LIDAR, and the LIDAR at the third (or north) runway, i.e., HKG3S LIDAR, would be considered. The LIDARs are so-called long-range units, providing spatial coverage up to 10 to 15 km from the equipment itself. They work with laser beams with wavelengths of about 1.5 microns, and measure the line-of-sight velocities by tracking the movement of the aerosols in the air. The accuracy of wind measurement is in the order of 1 m/s or less.

These LIDARs provide plan position indicator (PPI) scans at a number of elevation angles in order to give an overview of the wind distribution inside and around the airport. They also make a number of range height indicator (RHI) scans at selected azimuth angles from the north to capture the vertical structure of the airflow, e.g. along the runway glide paths, or in the planes perpendicular to the major mountain features of Lantau Island, such as downstream of the hills and the valleys. The PPI and RHI scans are updated every few minutes. Only the Doppler velocity images would be considered, which provide the line-of-sight velocities for monitoring low-level jets, waves and jump-like features in the RHI scans, and vortices in both RHI and PPI scans.

The background meteorological conditions are provided by the radiosonde ascent data at King's Park, which is located at about 60 km to the east of the airport. Inside HKIA itself, vertical profiles of the wind are also provided every 10 minutes by the radar wind profiler running at 1290 MHz radar waves, and vertical profiles of temperature and humidity are provided hourly by the ground-based microwave radiometer at the airport, which works with 7 oxygen channels and 7 water vapour channels. Compared with radiosonde, wind profilers and radiometers have coarser vertical resolutions, but much higher temporal resolutions. These vertical profiles are used to calculate the various parameters such as Richardson number, Froude number, Scorer parameter, etc.

2.2. Numerical model

The mesoscale model in use is the Regional Atmospheric Modeling System (RAMS) version 6.3. Its initial and boundary conditions are provided by the re-analysis of European Centre for Medium Range Weather Forecast (ECMWF) at a spatial resolution of 25 km and a temporal resolution of every hour. The spatial resolution of the RAMS simulation is increased by a factor of five, namely, 25 km, 5km, 1 km, 200 m, and 40 m. The coarse domain has a timestep of 10 seconds, with a timestep ratio of 10. The first model level is about 30 m above sea surface. There is then stretching ratio of 1.08 (i.e., the ratio of the model level heights between the adjacent model levels). The simulation is essentially a large eddy simulation (LES) of terrain-disrupted airflow at HKIA.

Of particular importance is the choice of turbulence parameterization schemes. The Smagorinsky scheme (*Smagorinsky*, 1963) is employed for the first two nests, and the Deardorff scheme (*Deardorff*, 1980) for the remaining three nests. The sensitivity of the simulation results to the choice of turbulence parameterization schemes would be considered in a follow-up study. The existing combination is found to produce reasonable results in the past studies of terrain-induced windshear at HKIA. The other physical settings could be found in *Chan et al.* (2021).

3. Results

3.1. Kelvin-Helmholtz (KH) instability

Synoptically, a ridge of high pressure over southeastern coast of China brought easterly winds to the coast of Guangdong on that day (not shown). For the RHI scan of HKG2 LIDAR to the west-southwest, outbound easterly flow was measured within the atmospheric boundary layer. However, the easterly winds were not static and waves could be identified at various heights (*Fig. 1*).

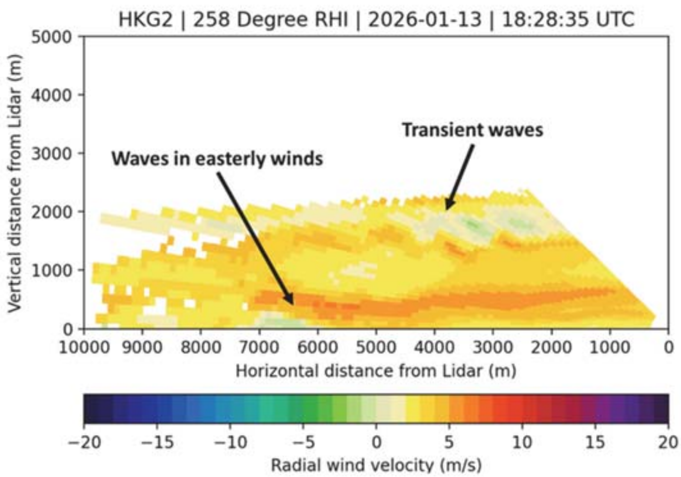

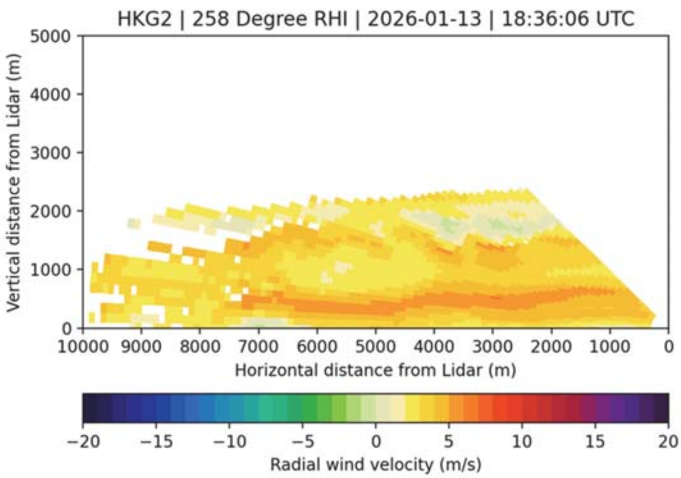

Fig. 1. RHI scans of Doppler velocity of HKG2 LIDAR, showing the vortices associated with KH instability at two time instances (a) and (b).

A number of waves was found in the easterly wind between the ground and about 1000 m above ground. At higher altitudes, between about 1000 m and 2000 m above ground, not only transient waves occurred, some inbound flow could be identified above the waves, so that there was a number of vertical circulating flow with a size of about several hundred metres. This is the first documented observation of waves associated with KH instability in the RHI scans of the Doppler LIDARs at HKIA. Such waves related to KH instability occurred for a few minutes only in the RHI scans and disappeared afterwards.

To study the KH instability further, the wind data from the radar wind profiler and the temperature profiles from the ground-based microwave radiometer at the airport are analyzed in detail with the calculation of Richardson number (*Ri*). Hourly *Ri* is determined from the following equation:

$$Ri = \frac{N^2}{\left(\frac{\partial u^2}{\partial z}\right)+\left(\frac{\partial v^2}{\partial z}\right)} \tag{1}$$

where *N* is the Brunt-Vaisala frequency, *u* and *v* are the horizontal components of the wind, and *z* is the height. It is a ratio of the buoyancy term and the shear force team. The vertical wind profile from the high mode of the wind profiler (with a nominal measurement height of 6 km above ground) is considered.

The vertical profiles of the Richardson number at 18 UTC and 19 UTC of January 13, 2026 are considered, as shown in *Fig. 2(a)*. In this period, *Ri* decreased from 0.82 to 0.18 at a height of about 1500 m above ground. Further analysis of the two terms (*Figs 2(b)* and *2(c)*) shows that, while there was a 7% decrease of the buoyancy term, there was a 320% decrease of the shear force term. As a result, *Ri* is less than 0.25 for a short while, which is consistent with the occurrence of KH instability as in the RHI scan of the LIDAR.

To study the significant drop of shear force term in detail, the time-height cross section of the wind as measured by the radar wind profiler is shown in *Fig. 3*. At 18 UTC, the 10-minute wind direction/wind speed at 1400 m is 120 degrees / 5.3 m/s, and at 1500m is 127 degrees / 6.1 m/s. At 19 UTC, the 10-minute wind direction/wind speed at 1400 m is 133 degrees / 4.8 m/s, and at 1500 m is 160 degrees / 4.4 m/s. The wind direction angle difference between 1400 m and 1500 m changes from 7 degrees to 27 degrees. The 320% increase of shear force term is related to a quite small angle difference from 18 UTC to 19 UTC. It is shown in *Fig.3* that such a change happens for a short while, which is consistent with the observed transiency of the occurrence of KH instability wave in the RHI scans of the LIDAR. The slight change of the wind direction angle difference is believed to be correct.

An attempt is made to simulate the waves associated with the KH instability, namely, initialized at 17 UTC of January 13, 2026, running up to January 20, 2026. Within the generally outbound flow below a height of about 2500 m above ground, some isolated areas of inbound flow could be simulated (*Fig.4*), which seems to be consistent with the actual LIDAR observation (*Fig.1*). However, the wave features are not apparent in the simulation. Similar to the actual RHI scans of the LIDAR, such inbound flow regions are transient and occurs for a few minutes only (not shown).

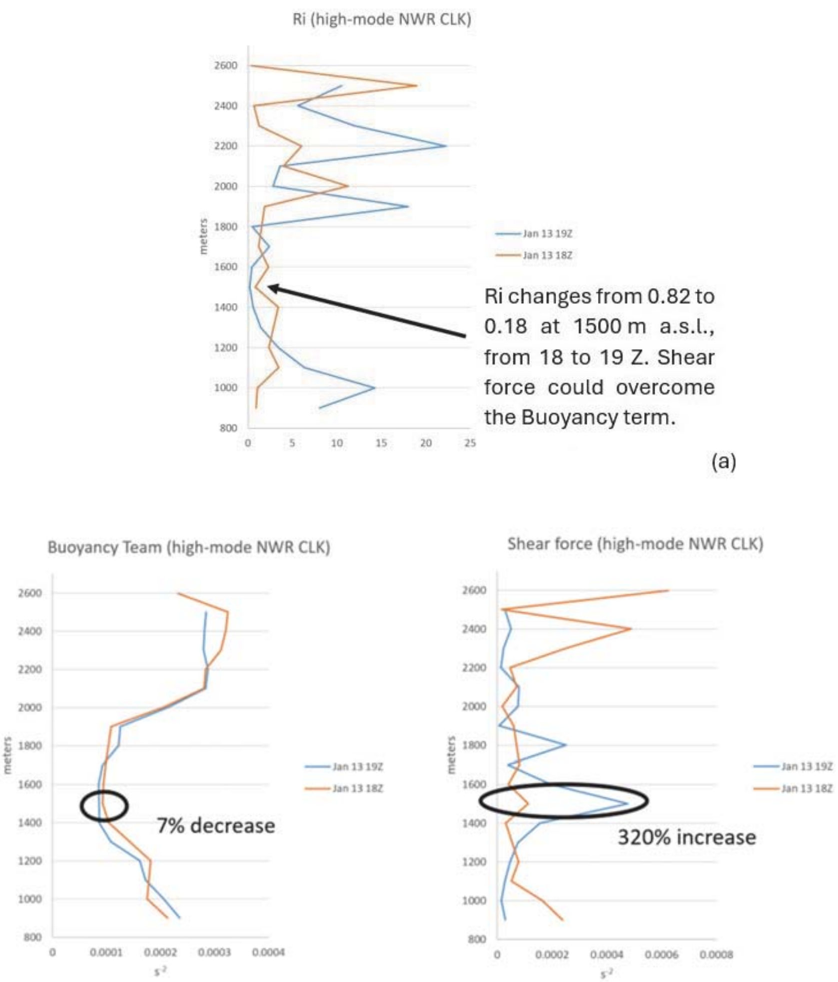

(b) (c)

Fig. 2. Vertical profile of Richardson number (a), and the vertical profiles of buoyancy term (b) and shear force term (c).

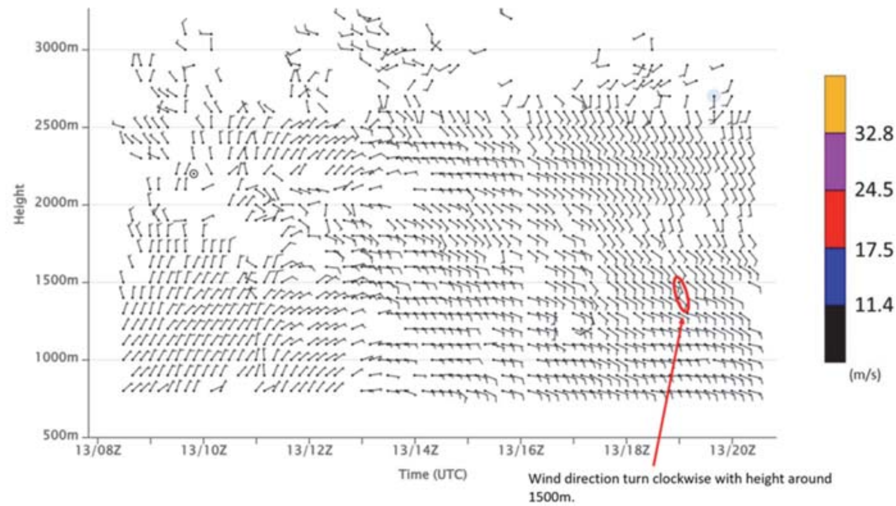

Fig.3. Time-height cross section of horizontal winds from the wind profiler at the airport.

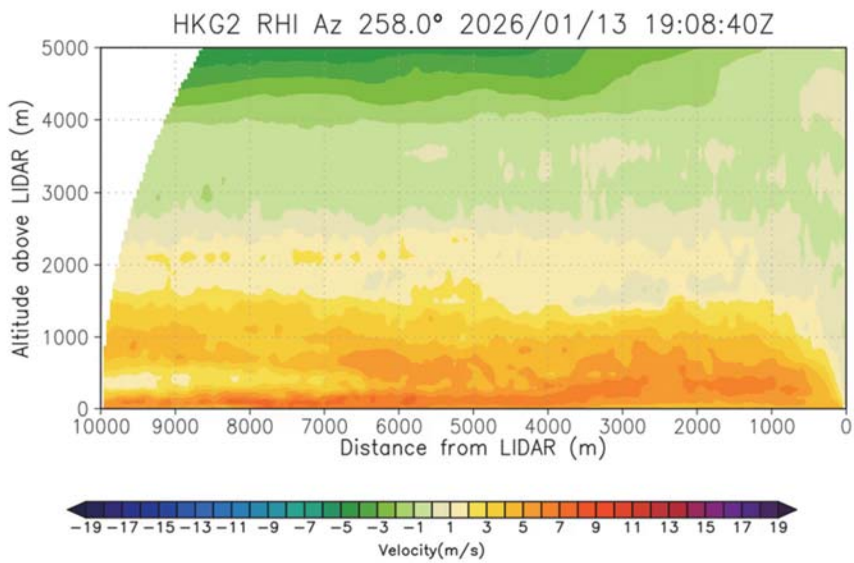

Fig. 4. Simulated RHI scan of Doppler velocity of HKG2 LIDAR.

3.2. *Vortex-shedding*

As shown by the PPI scans of the LIDAR, fresh to strong east to southeasterly winds prevailed over the airport region at the night time of December 21, 2025. To the southwest of the airport, the east-southeasterly flow was disrupted by the mountains of Lantau Island, leading to the occurrence of shedding vortices from the terrain. Such vortices appear as inbound flow (coloured green) in the LIDAR's PPI scan. A sequence of the event is shown in *Fig. 5*, with the vortex appearing to detach from the mountain first (*Fig.5(a)*), travelling downstream (*Fig.5(b)*), getting to the maximum range of the LIDAR (*Fig.5(c)*) and dissipating gradually, with the occurrence of another shedding vortex from the mountain (*Fig.5(d)*). The whole process takes about 20 minutes.

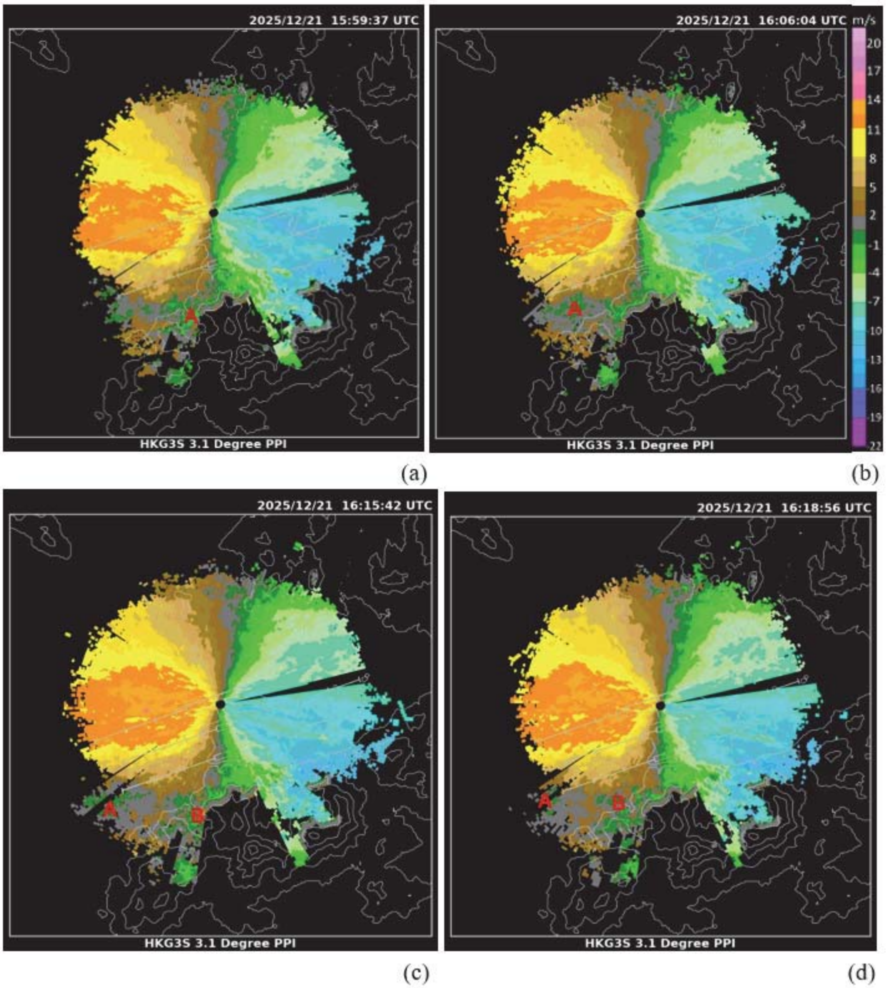

Fig.5. PPI scan of Doppler velocity of HKG3S LIDAR, showing shedding of vorices.

In order to study the period of shedding vortices, the associated with direction changes as measured by the anemometer at the western end of the south runway (R1W anemometer) have been analyzed using Fourier transform. The period from 18 UTC of December 21, 2025 to 05 UTC of December 22, 2025 is analyzed, and the wind data are considered in a number of half-an-hour time intervals. Within each half an hour, the 1-minute mean wind direction from R1W anemometer updated every minute is used to build up the time series, which is analyzed through Fourier transform. A typical frequency spectrum is shown in *Fig. 6(a)*. There are a number of peaks identified in the spectrum, and the most prominent peak has been selected to plot the time series of the most prominent periods of fluctuations of wind direction as shown in *Fig. 6(b)*. The major periods are around 20 minutes at 18 UTC of December 21, 2025, 24 minutes at around 22 UTC of that day, and 17 minutes at around 02 UTC of December 22, 2025.

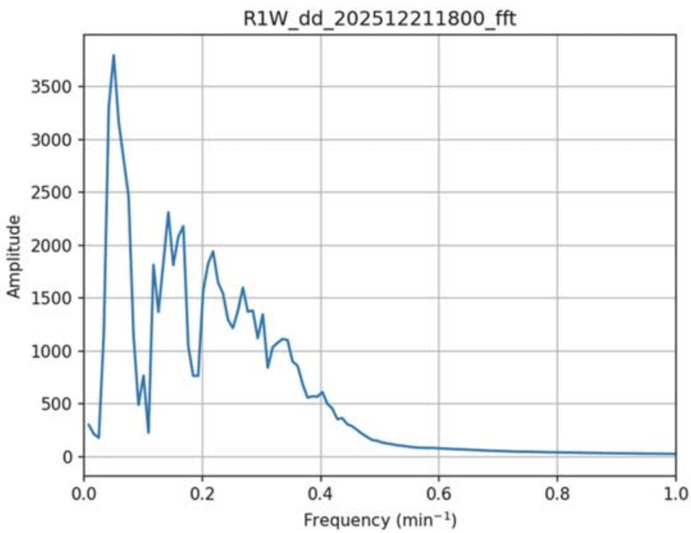

(a)

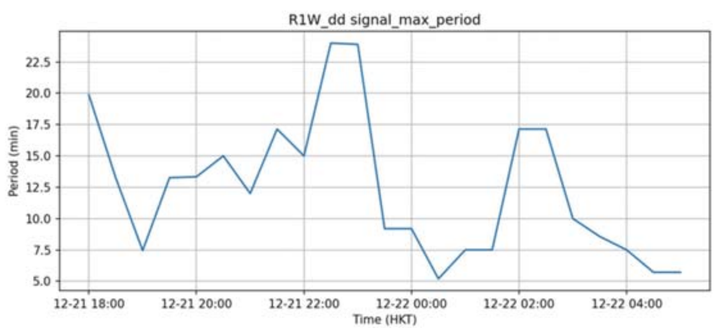

(b)

Fig.6. A sample frequency spectrum of R1W wind direction (a) and the time series of the most prominent period through spectral analysis (b).

When winds blow along a mechanical obstacle such as mountains, oscillatory flow could be observed downstream in the form of vortex shedding when the boundary layer profile is sufficiently stable. According to *Atkinson* (1981), the shedding period T (s) could be expressed in terms of the Strouhal number (S_t) and the horizontal dimension D of the obstacle:

$$T = \frac{D}{S_t U_0}, \tag{2}$$

where U_0 is the background wind speed (m/s) at Nei Lak Shan (747m above sea level), D would be taken as 4000m for Nei Lak Shan as an estimated width of the obstacle for the interest of this study. Based on the above discussion, T ranges about 17 minutes and 24 minutes. U_0 in the order of 8 m/s. As such, S_t is about 0.49 and 0.34. *Atkinson* (1981) suggested that the range of value of S_t would fall within 0.15 to 0.32, which is generally consistent with the observed results.

Vosper (2000) mentioned that the vortex shedding would occur when Froude number (F_h) is less than or equal to 0.4, F_h is defined by:

$$F_h = \frac{U}{Nh} \tag{3}$$

where N is the Brunt–Väisälä frequency (s^{-1}) and h is the height of mountain. U is taken to be about 8 m/s and N is taken to be about the square root of 0.0003 based on radiosonde ascent at King's Park at 13 UTC of December 21, 2025. As such, F_h is found to be about 0.6.

Another formulation of Froude number is based on *White* (1999). The Froude number (Fr) is take to be:

$$Fr = \frac{\langle U \rangle_h}{\sqrt{g_r h}} \tag{4}$$

where $\langle X \rangle$ indicates a vertical/depth average over the extent of X, U is the wind speed, and g_r the reduced gravity, and

$$g_r = \frac{g(\theta_T - \langle \theta \rangle_h)}{\langle \theta \rangle_h} \tag{5}$$

where g is the gravitational constant, θ_T the free troposphere potential temperature, and θ the potential temperature. Based on the radiosonde data at 13 UTC of December 21, 2025, θ_T is about 301 K, and $\langle \theta \rangle_h$ is about 292 K. The wind speed U is about 8 m/s at the mountain top. As such, the Froude number is 0.52.

From the above results, both formulations of Froude number give comparable values. The calculated Froude numbers are generally consistent with the result in *Vosper* (2000).

Numerical simulation has been performed between 14 and 17 UTC of December 21, 2025. A sample sequence of simulated LIDAR PPI scans of Doppler velocity is shown in *Fig. 7*. Vortex shedding has been simulated successfully, and the shedding period is also found to be in the order of around 20 minutes, consistent with the actual observations from the LIDAR.

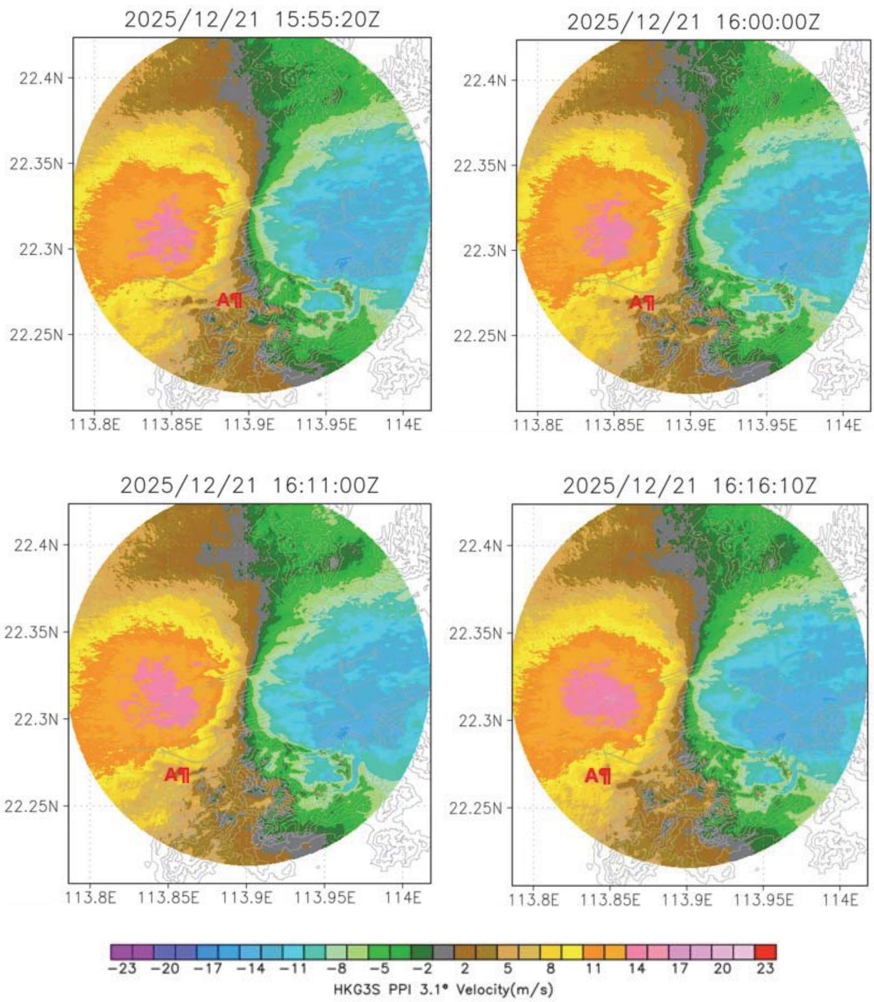

Fig. 7. Simulated PPI scans of Doppler velocity of HKG3S LIDAR, showing the vortex.

3.3. *Hydraulic jump and mountain wave*

Jump-like feature has been observed in easterly winds flowing over Lo Fu Tau, a hill of about 460 m above sea level at the northeastern part of Lantau Island, as shown in the RHI scan of HKG2 LIDAR with an azimuth angle of 95 degrees (*Fig. 8(a)*). Recirculating flow (inbound flow) has been observed both below and above the easterly jet (coloured dark blue and green), which is a typical feature of jump-like feature.

The jump-like structure is studied further using a two-layer model. The depth of the atmospheric boundary layer, h, can be of the order of the terrain elevation, i.e., 460 m, and the nature of the flow depends upon the Froude number (Fr) in Eq. (4). Based on the radiosonde data at 00 UTC of January 25, 2026, θ_T is about 293 K, and $\langle\theta\rangle_h$ is about 288 K. The wind speed U is about 10 m/s at the mountain top. As such, the Froude number is more than 1, i.e., it is supercritical, and this supports the occurrence of the jump-like feature.

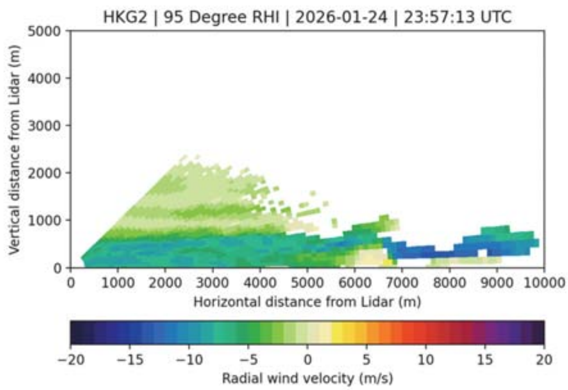

(a)

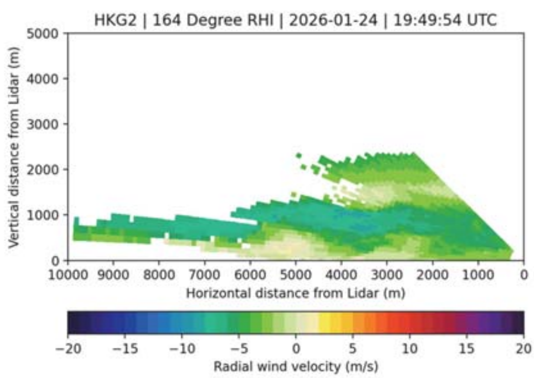

(b)

Fig. 8. RHI scans of HKG2 LIDAR, showing jump-like feature (a) and mountain wave (b).

At the same time, across the Tung Chung gap (a gap of about 300 m above sea level at the middle of Lantau Island), some transient waves have been observed in the RHI scan of HKG2 LIDAR with an azimuth angle of 164 degrees. An example is shown in *Fig. 8(b)*. Recirculating (inbound) flow has been observed below the jet associated with the wave. The wave is transient and occurs for a couple of scans only separated by a few minutes, and disappears afterwards.

In order to study the wave, the Scorer parameter is calculated (*Scorer,* 1949) based on the radiosonde data at 00 UTC of January 25, 2026, as shown in *Fig. 9*:

$$l^2 = (N(z) / U(z))^2 - U_{zz}/U, \quad (6)$$

where N is the Brunt-Vaisala frequency, $U(z)$ is the cross-mountain wind speed profile and U_{zz} is the second derivative of U with height z. The Scorer parameter does not show decreasing trend from ground up to a height of about 700 m above ground. As such, the background atmosphere does not seem to support stationary mountain wave, which is consistent with the rather transient nature of the wave as observed in the 164-degree RHI scan of the LIDAR.

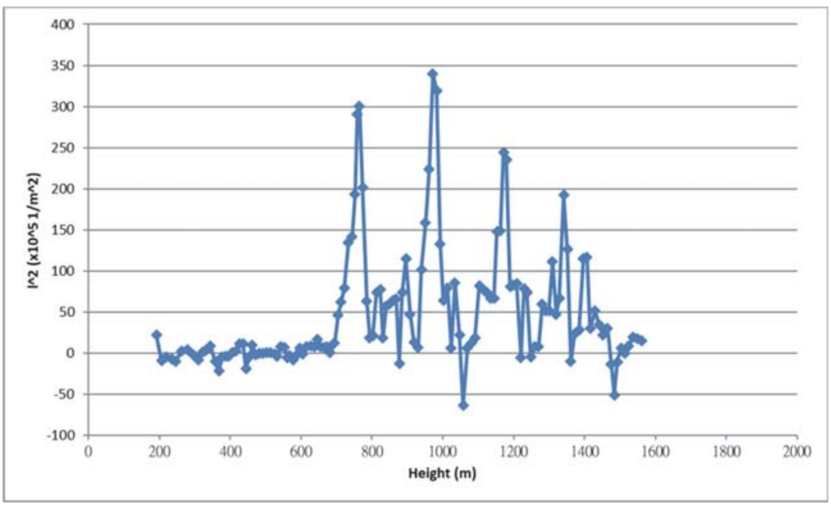

Fig.9. Scorer parameter profile based on radiosonde data for the case of *Fig. 8*.

Numerical simulation has been performed between 18 UTC of January 24, 2026 up to 01 UTC of January 25, 2026. It is very hard to look for jump-like feature at Lo Fu Tau and wave like feature at Tung Chung gap with recirculating flow. A couple of sample simulated RHI scans showing similar features could be found in *Figs 10(a)* and *10(b)*, respectively. In *Fig. 10(a)*, there is a bit of jump-like feature downstream of Lo Fu Tau, with recirculating flow above and below the jet, but the feature lasts for a few minutes only. Similar transiency in wave-like feature is also found in Tung Chung gap in *Figure 10(b)*, with the occurrence of inbound flow below the wave for a short while.

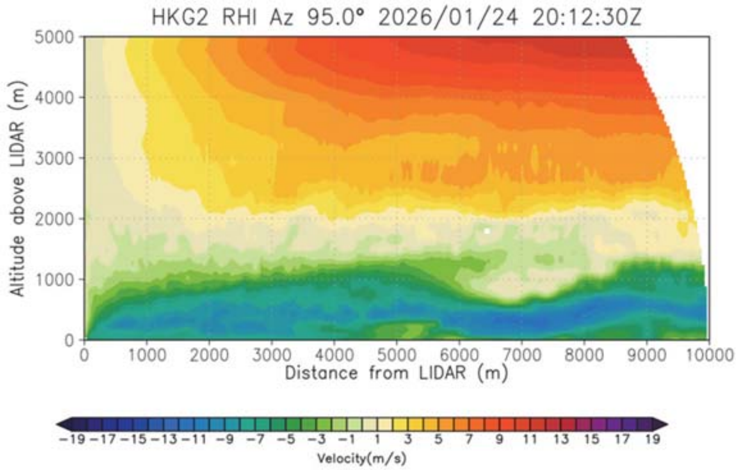

(a)

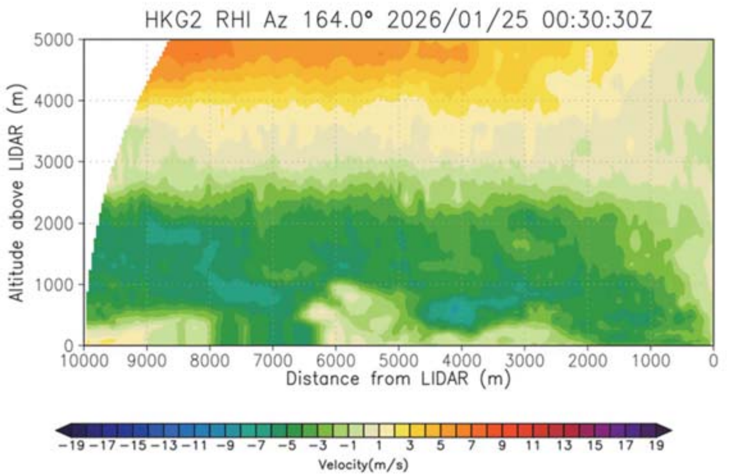

(b)

Fig.10. Simulated RHI scans of HKG2 LIDAR for jump-like feature (a) and mountain wave (b).

3.4. Mountain wave

Rather stationary mountain waves are occasionally observed downstream of Lo Fu Tau in easterly winds. An example is shown in *Fig. 11(a)* with a wavelength of about 3000 m. At the same time, a wave could be identified downstream of Tung Chung gap near the airport, as shown in *Fig. 11(b)*. Such features normally occur in stable boundary layer, when mountain wake is observed downstream of the mountains of Lantau Island, as shown in the LIDAR PPI scan in *Fig. 12*. There is a west-northwest to east-southeast oriented and elongated flow of inbound velocity (green color) to the west of Lantau Island and southwest of the airport.

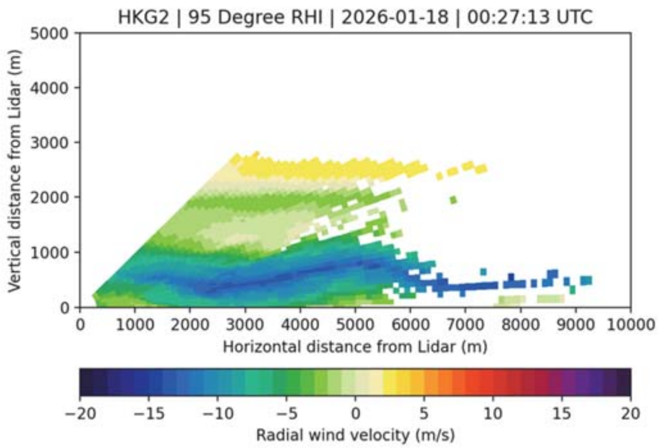

(a)

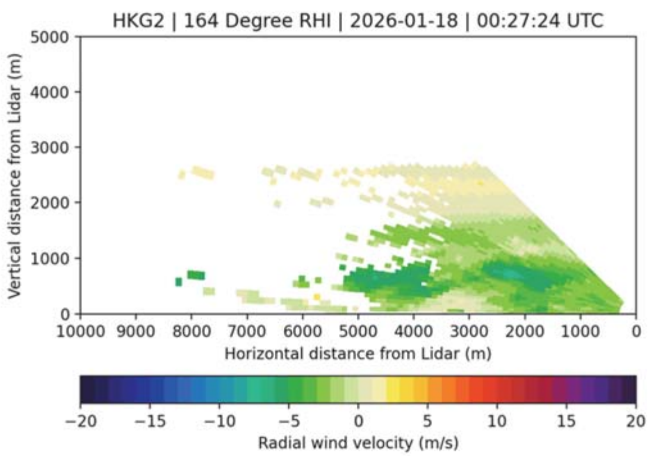

(b)

Fig.11. RHI scans of HKG2 LIDAR showing mountain waves at Lo Fu Tau (a) and the Tung Chung gap (b).

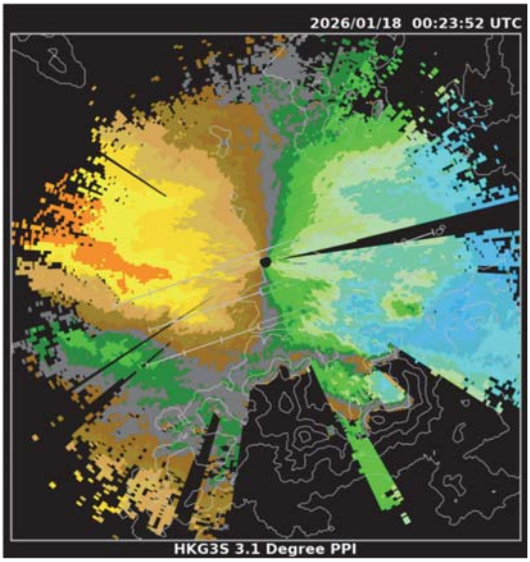

Fig. 12. PPI scan of the LIDAR from HKG3S LIDAR.

Following Eq.(6), the Scorer parameter is calculated based on radiosonde data at King Park at 00 UTC of January 18, 2026. The result is shown in *Fig. 13(a)*. There is a drop of Scorer parameter from a height of about 100 m to about 500 m, which is consistent with the observed mountain wave across Tung Chung gap. On the other hand, the drop of Scorer parameter from 500 m to 800 m is not very clear. From the vertical profile of potential temperature (*Fig. 13(b)*), there is a rather significant temperature inversion at a height of about 600 m above sea level. This strong inversion is favourable to the occurrence of mountain wave. It is consistent with the observed occurrence of stationary mountain wave downstream of Lo Fu Tau with a height of about 460 m above sea level.

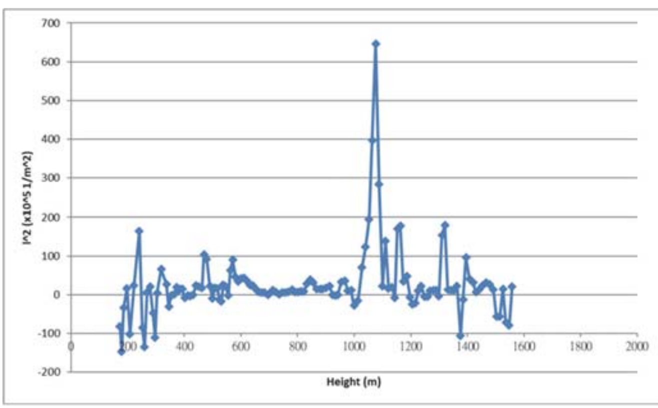

(a)

Fig. 13. Scorer parameter profile (a) and potential temperature profile (b) based on radiosonde data for Lo Fu Tau and the Tung Chung gap.

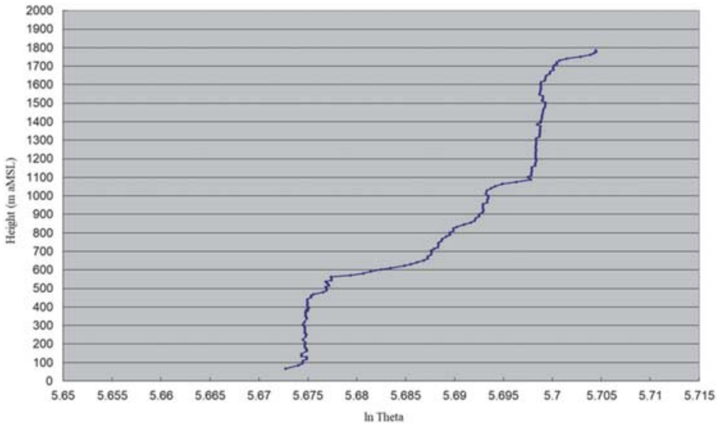

(b)

Fig. 13.(ctd.) Scorer parameter profile (a) and potential temperature profile (b) based on radiosonde data for Lo Fu Tau and the Tung Chung gap.

Simulation has been performed between 21 UTC of January 17, 2026 and 01 UTC of January 18, 2026. In the simulated RHI scans of the LIDAR, mountain waves are clearly observed downstream of Lo Fu Tau (*Fig. 14(a)*) and Tung Chung gap (*Fig. 14(b)*). There is also an extensive area of inbound flow downstream of the mountains of Lantau Island in the simulated PPI scan of the LIDAR (*Fig. 15*). The major features of the LIDAR Doppler velocity scans are reproduced successfully.

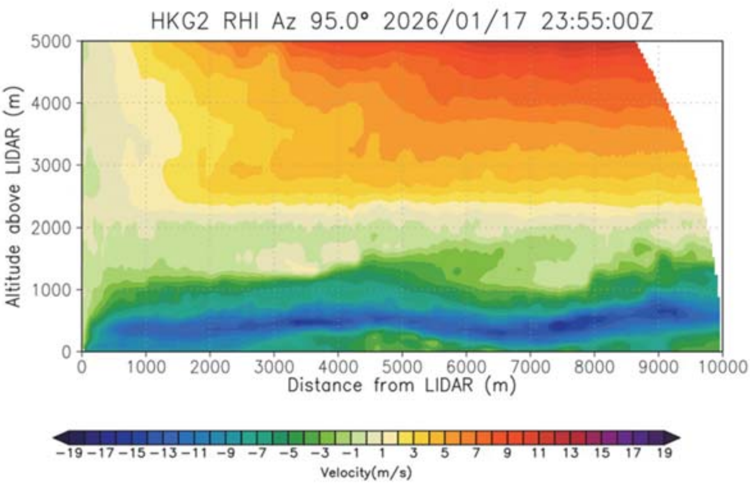

(a)

Fig. 14 Simulated mountain waves at Lo Fu Tau (a) and the Tung Chung gap (b).

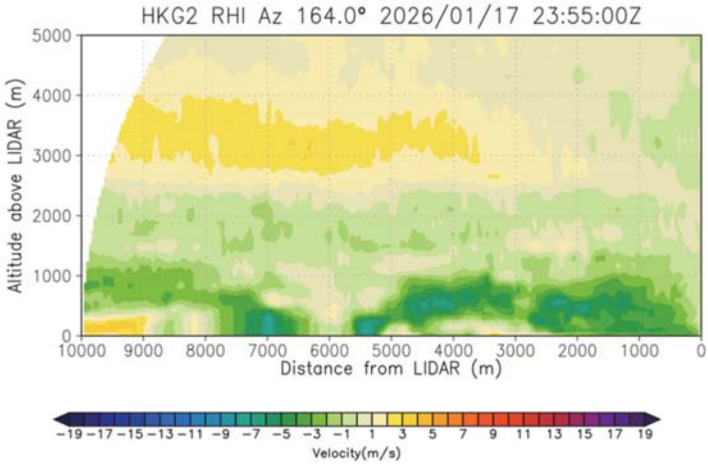

(b)

Fig. 14. (ctd.) Simulated mountain waves at Lo Fu Tau (a) and the Tung Chung gap (b).

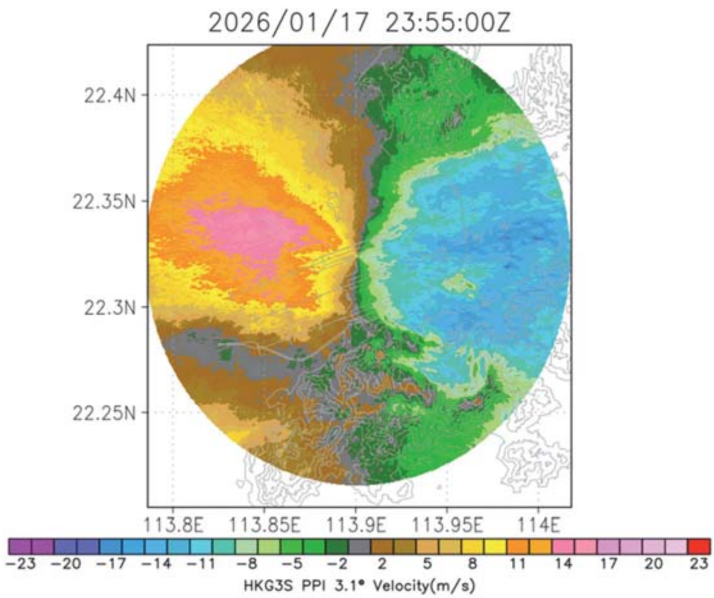

Fig. 15. Simulated PPI scan of HKG3S LIDAR.

4. Conclusion

This paper documents a number of interesting features of terrain-disrupted airflow at HKIA in easterly wind situations. For the first time, vortices associated with KH instability are observed in the RHI scan of the LIDAR. Vortex shedding is observed again, with the period of shedding being analyzed using the wind direction data from a runway anemometer. Jump-like features and mountain waves are also observed in the RHI scans as well. The occurrence of such features is in general consistent with the expectations from the parameters as calculated from the upper air wind and temperature profiles, such as Richardson number, Scorer parameter and Froude number. In addition, this paper suggests that the Scorer parameter could diagnose the background atmosphere favourable for the occurrence of stationary and transient waves at HKIA.

High resolution NWP simulations have been performed to study the possibility of reproducing such features. The simulations are a mixed success. Some features are more readily simulated, such as mountain waves and jump-like features. However, vortices associated with KH instability are not readily reproduced in the simulation. Vortex shedding can be simulated to a certain extent, with the shedding period basically reproduced, but the inbound flow in the vortex does not show up clearly in the simulation. More experiments would be conducted to find out the more appropriate combinations of parameterization schemes in order to be more successful in simulating these flow features.

References

Atkinson, B.W., 1981: Meso-scale Atmospheric Circulations. *Academic Press.* https://doi.org/10.1002/joc.3370020313

Chan, P.W., Lai, K.K., and *Li, Q.S.,* 2021: High-resolution (40 m) simulation of a severe case of low-level windshear at the Hong Kong International Airport—Comparison with observations and skills in windshear alerting. *Meteorological Applications 28,* https://doi.org/10.1002/met.2020

Deardorff, J.W., 1980: Stratocumulus-capped mixed layers derived from a three-dimensional model. *Boundary Layer Meteorology 18,* 495-527. https://doi.org/10.1007/BF00119502

Scorer, R.S., 1949: Theory of waves in the lee of mountains. *Q. J. R. Meteorol. Soc. 75,* 41–56. https://doi.org/10.1002/qj.49707532308

Smagorinsky, J., 1963: General circulation experiments with the primitive equations. *Monthly Weather Review 91,* 99-164. https://doi.org/10.1175/1520-0493(1963)091<0099:GCEWTP>2.3.CO;2

Vosper, S.B., 2000: Three-dimensional numerical simulations of strongly stratified flow past conical orography. *Journal of the Atmospheric Sciences 57,* 3716–3739. https://doi.org/10.1175/1520-0469(2000)057<3716:TDNSOS>2.0.CO;2

White, F.M., 1999: Fluid mechanics (4th ed.). *WCB/McGraw-Hill.* ISBN 978-0-07-116848-9

DOI:10.28974/idojaras.2026.3.5

IDŐJÁRÁS

Quarterly Journal of the HungaroMet Hungarian Meteorological Service
Vol. 130, No. 3, July – September, 2026, pp. 317–342

Spatial analysis of evapotranspiration and drought under climate change scenarios in the Qazvin region of Iran

Bijan Nazari[1,*]**, Arezoo Kazemi**[1]**, Maryam Dehghani Ahmadabadi**[2]**, Samaneh Ehsani Kolikand**[3]**, Elahe Kanani**[3]**,** and **Hamid Nazaripour**[4]

[1] *Department of Irrigation and Reclamation Engineering, Faculty of Agriculture, College of Agriculture and Natural Resources, University of Tehran, Karaj, Iran*

[2] *Department of Water Engineering, Faculty of Engineering, Payame Noor University of Tehran, Iran.*

[3] *Department of Water Sciences and Engineering, Imam Khomeini International University, Qazvin, Iran.*

[4] *Department of Physical Geography, University of Sistan and Baluchestan, Zahedan, Iran.*

**Corresponding author E-mail: binazari@ut.ac.ir*

(Manuscript received in final form on December 23, 2025)

Abstract— The simultaneous assessment of evapotranspiration and drought is imperative for adaptive water resource planning due to the growing challenges posed by climate change on agricultural production. A downscaling exercise was carried out using the SDSM model for three climate scenarios developed as part of the Sixth Assessment Report (CMIP6): an optimistic scenario (SSP126), a moderate scenario (SSP245), and a pessimistic scenario (SSP585). For model calibration and validation, long-term meteorological data from five stations were used, and drought conditions were assessed using the standardized precipitation index (SPI). Based on the validation results, the model demonstrated high accuracy for simulating temperature and reference evapotranspiration. However, precipitation simulations demonstrated moderate accuracy. Under all scenarios, annual temperatures increased, with the largest increase projected under SSP585. In spite of the fact that changes in precipitation did not reach statistical significance, it is likely that a moderate decline will occur by 2062, under SSP126. Under future climate conditions, there will be a decrease in precipitation in the southeast of the province, an intensified warming in Buin-Zahra, and an increase in evapotranspiration. It was noted that there were frequent severe droughts over the past years. Based on projections for the next decade, drought and wet periods are expected to alternate, with adverse effects expected in the southeast and Buin-Zahra regions. It is evident, from these findings, that sustainable water resource management, climate-adapted agricultural methods, and spatially targeted planning are urgently required to reduce the vulnerability of the province of Qazvin. Hence, adaptation policies should prioritise highly vulnerable areas based on the presented spatial analysis in order to enhance agricultural resilience to drought and climate change.

Key-words: CMIP6, evapotranspiration, temperature, climate change adaptation, standardized precipitation index

1. Introduction

Climate change and the increasing trend and magnitude of extremes in the past decades, particularly in arid and semi-arid regions, have become the most important environmental, economic, and social challenges worldwide (*Nazari et al.*, 2023, 2024). The fluctuations of temperature, rainfall, solar radiation, and relative humidity and other climatic variables directly affect the hydrological cycle and threaten the sustainability of water resources, food security, and agricultural yield. Evapotranspiration is the most significant pathway of water loss in the hydrological cycle and plays a critical role in estimating crop water requirements, irrigation planning, reservoir management, and evaluating the sustainability of groundwater resources (*Karimi et. al.*, 2028, *Dehghanisanij et al*., 2020; *Kanani et al*., 2022). Evapotranspiration reflects the energy balance and moisture status of the environment and is considered a very sensitive indicator of climate change. Higher temperatures, decreased relative humidity, increased longwave radiation, altered wind speed, and changed precipitation can directly increase the rate of evapotranspiration. Consequently, climate change is often first manifested in evapotranspiration and then emerges as reduced soil moisture, increased plant water stress, and eventually the onset of meteorological, agricultural, and hydrological droughts (*Nazari et al*., 2023). The interlinking between evapotranspiration and drought emphasizes that both should be evaluated together when studying climate change. Since increasing evapotranspiration increases the demand for water but decreases renewable water supply, understanding the spatial-temporal evolution of evapotranspiration provides critical insights into future drought tendencies. Hence, neglecting evapotranspiration in the assessment of droughts probably leads to a partial understanding of the hydrological cycle and misinformed decisions about water management (*Kanani et al*., 2025).

Several studies have looked at the effects of climate change on precipitation, evapotranspiration, and drought characteristics at local, regional, and global scales. Climate projections for countries within the MENA region demonstrate that, with a few exceptions, annual precipitation will decrease significantly, by about 15–20%, combined with increased reference evapotranspiration for nearly all countries. Changes will be most prevalent in North Africa; middle and eastern Iran; and parts of Syria, leading to increased frequency and intensity in existing water deficits, especially in countries such as Morocco (*Terink et al*., 2013). On the global level, long-term variability studies indicate that rising temperatures and increased atmospheric evaporative demand have caused an expansion in dryness and increased frequency of droughts since the 1970s, which has been especially apparent in Africa, the Middle East, southern Europe, North America, and parts of East and South Asia, and is also expected to continue through the 21st century (*Lhotka et al*., 2018, *Dai*, 2011). Continental-scale assessments using NASA's NEX-GDDP downscaled models indicate future severe droughts to potentially become increasingly widespread in frequency in the United States, particularly in the western states and during summer months, in response to changes in precipitation and temperature (*Ahmadalipour et al*., 2016). Basin-scale studies report analogous results. For instance, multi-model studies evaluating future changes in ETref in the Segura River Basin (southeastern Spain) point out a significant upward trend in ETref in accordance with most of the climate scenarios, particularly RCP8.5, with stronger increases in the upstream regions of the basin. Amongst the multi-model methods utilized, the Random Forest algorithm indicated the best accuracy in the reproduction of daily ETref (*Ruíz Álvarez et al*., 2021). Studies that have examined the climatic drivers of evapotranspiration change further highlight the dominating role of solar radiation, relative humidity, and minimum temperature. In the case of Zhejiang Province in China, for example, these three projected variables for 2011–2040 contribute most to future PET variability, showing marked seasonal and spatial differences according to the climate model used (*Xu et al*., 2014).

High-resolution climate modeling in mountainous headwater systems, such as the Upper Colorado Basin, suggests that despite increases in winter precipitation, higher fractions of evapotranspiration and reduced snowfall ratios result in overall reductions in annual runoff by approximately 6%. In addition, earlier timing of snowmelt and peak discharge events under these conditions is further evidence of increasing basin dryness under projected future climate conditions. This conclusion is based on work by *Rasmussen et al*. (2014). Similarly, application of the multivariate drought indices-MDI-and entropy-based analysis in Texas reveal that climate change is likely to expand high-risk drought zones and increase socio-economic vulnerability. Such studies not only map the combined risk of drought on spatial distributions but also quantify causal relationships between hydroclimatic drivers of drought occurrence by identifying the most dominant drivers of future drought hazards. These are based on the work done by *Rajsekhar et al*. (2015). Due to its geographical position and mostly arid to semi-arid climate, Iran is one of the more vulnerable territories regarding the impacts of climate change. There is evidence that the country's mean temperature increased by almost 2 °C within the last century, with large portions of the semi-arid zones having gradually been shifted toward drier conditions according to

Gholami et al. (2017). Furthermore, being among the key greenhouse gas emitting countries of the Middle East, Iran is directly exposed to the climatic consequences in a way that the changes manifest themselves in rising temperatures and declining precipitation, changes in seasonal rainfall, and more intensive droughts according to *Daneshvar et al*. (2019)**.**

Qazvin Province is one of the major agricultural hubs in Iran, which is located in an arid to semi-arid climate and presently faces acute challenges regarding available water resources. The province covers two major basins, Shahroud–Sefidrud and Shur River, and is very dependent on groundwater resources, with aquifers providing over 80% of the total water demand. This heavy reliance, coupled with the pressures of population growth, urban expansion, industrial development, and agricultural needs, has been associated with alarming declines in groundwater levels. The consequences include land subsidence, water quality degradation, agricultural water stress, and the weakening of natural ecosystems. Recent studies have pointed out even more severe threats to the future of water resources in Qazvin Province. *Ghorbani and Valizadeh* (2014) showed that under climate change, the first autumn frost and the last spring frost will be advanced, thereby reducing the frost period. In practice, this means an extended growing season and increased crop water needs. Moreover, *Mirsane et al.* (2011) have found that the crop water demand during 2010–2039 may increase by at least 30%, indicating a great impact of climate change on evapotranspiration and consequently the agricultural water management. Altogether, all of these pieces of evidence explain that climate change, besides altering precipitation and temperature regimes, significantly affects hydrological processes and water balance due to the increased evapotranspiration, thereby intensifying drought conditions at various levels. Therefore, a detailed and spatially explicit analysis of evapotranspiration and drought in various climate scenarios is necessary to enable planning for adaptation to future conditions. Such an analysis can be useful for identifying critical hotspots, developing agricultural water management strategies, adjusting cropping patterns, and proposing effective adaptation solutions. It is important to underline that analyzing these phenomena independently cannot give a comprehensive picture of future water stress.

Changes in one climatic component (e.g., temperature) exert direct and indirect impacts on others (e.g., evapotranspiration), ultimately influencing the severity and duration of drought. Up to date, the lack of an integrated spatial assessment, which identifies the high-risk regions with increased evapotranspiration and intensified drought, represents a major knowledge gap in water resource planning and climate adaptation policymaking. The main goal of this study is to perform the spatial analysis of evapotranspiration and drought for Qazvin Province in the context of different climate change scenarios and to analyze the interrelationship between these two important components. This study tries to bring about an overall picture of future changes through integrating climatic data, predictive modeling, and spatial indicators. Besides, region-specific and applicable adaptation strategies concerning drought resilience and sustainable water resource management are one of the key objectives of the present study.

Accordingly, to operationalize the above-mentioned objectives and to provide a clear framework for the analysis, this study addresses the following research questions**:**

- How will evapotranspiration spatial patterns change in the Qazvin region under different climate change scenarios?
- How will the frequency, severity, and spatial distribution of drought evolve under future climate conditions?
- What is the spatial relationship between changes in evapotranspiration and drought intensity across the study area?
- Which areas can be identified as high-risk hotspots due to the simultaneous increase in evapotranspiration and drought severity?
- How can the results support region-specific adaptation strategies for agricultural water management under climate change?

2. *Material and method*

2.1. Study area

Qazvin Province, with its area of approximately 15,800 km², is one of Iran's crucial regions in terms of economic, agricultural, and environmental importance. It borders the provinces of Alborz, Mazandaran, Gilan, Zanjan, Hamadan, and Markazi. This province is situated in an arid to semi-arid climatic zone with a long-term mean annual temperature of 12.4 °C and an average annual precipitation of 307.1 mm (*Fig. 1*). In this study, five synoptic and climatological stations, namely, Qazvin, Avaj, Buin Zahra, Takestan, and Moallem-Kelayeh, were used for the baseline period (1993–2020). The dataset included temperature, precipitation, relative humidity, solar radiation, and other variables required for evapotranspiration modeling and drought assessment. All data used were obtained from the Qazvin Province Meteorological Administration.

2.2. Climate change

Climate change, recognized as one of the most significant global challenges, is defined by the Intergovernmental Panel on Climate Change (IPCC) as long-term and, in some cases, irreversible alterations in the average state of the atmosphere. In recent years, the sixth phase of the Coupled Model Intercomparison Project (CMIP6) has been developed with the aim of enhancing the accuracy of climate projections and addressing the limitations of previous-generation models (CMIP5). In this study, to assess future climatic conditions in Qazvin Province, three radiative forcing scenarios – SSP126 (optimistic), SSP245 (intermediate), and SSP585 (pessimistic) – were employed, representing a wide range of socio-economic development pathways and greenhouse gas emission trajectories. Given the limitations of Global Climate Models (GCMs) in generating climate data with adequate spatial resolution, the use of statistical and dynamical downscaling techniques becomes essential. Accordingly, the Statistical Downscaling Model (SDSM), first introduced by *Wilby et al.* (2002), was applied as one of the most effective tools for climate downscaling and generating future scenario data.

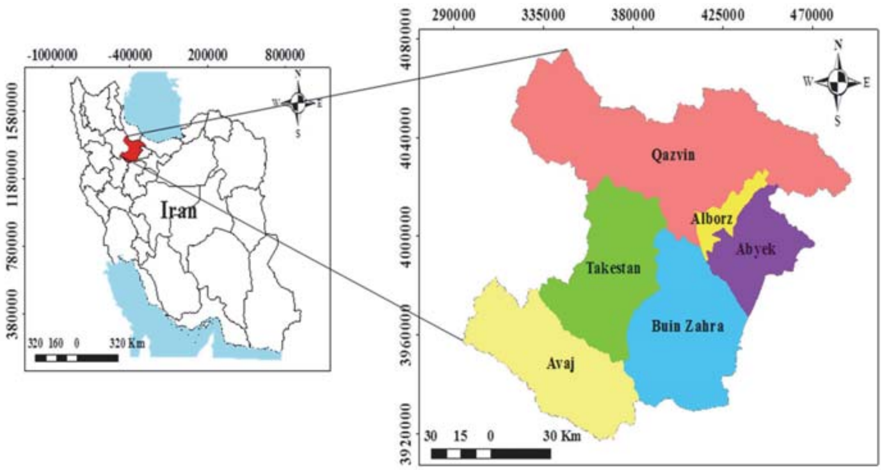

*Fig. 1***.** Location of the study area in Iran

The Statistical Downscaling Model (SDSM) was selected in this study due to its wide use and proven reliability in regional climate downscaling (*Phuong et al*., 2020; *Munawar et al*., 2022; *Sami et al*., 2024). SDSM allows flexible selection of predictor variables, incorporates rigorous quality control procedures (Dafouf, et al., 2025), and has been successfully applied in numerous studies to generate high-resolution climate scenarios for regions with complex topography (Abed, 2021). These features make it particularly suitable for assessing future climatic conditions in Qazvin Province.

This model facilitates the simulation of future climate conditions by enabling data normalization, quality control, and the selection of appropriate predictor variables. In this study, 70% of the historical dataset was allocated for calibration and the remaining 30% for validation of the SDSM model. Prior to model implementation, quality control procedures – including the removal of outliers, reconstruction of missing data, normality testing, and the Pettitt test for homogeneity – were conducted.

2.3. Simulation of precipitation, temperature, and evapotranspiration

In the simulation of climatic components, daily meteorological observations of synoptic stations in the province were considered, together with the NCEP reanalysis data and the outputs of GCMs under the three scenarios (SSP126, SSP245, and SSP585). The steps involved in the downscaling process using SDSM are data normalization, choosing suitable synoptic predictors, and the investigation of regression relationships between the local observations and upper-air pressure fields. Since the distribution of daily precipitation is not normal, a fourth-root transformation was applied to enhance the fit of the model. For the baseline period 1993–2020, the meteorological data from five stations, Qazvin, Avaj, Buin Zahra, Takestan, and Moallem-Kalayeh, were used in the downscaling temperature, precipitation, and evapotranspiration.

2.4. Drought

One of the most widely used meteorological drought indicators, the standardized precipitation index (SPI), was applied to monitor and analyze drought conditions. The index is calculated based on precipitation deviation from the long-term mean over a specified time scale, normalized by the standard deviation over the same period. SPI can be computed for several time scales, including 1, 3, 6, 9, 12, 24, and 48 months, each representing different types of droughts, ranging from short term to long term. Drought occurs when SPI values are continuously negative, and SPI less than –1 indicates a notable drought intensity. Classes of drought severity based on SPI are shown in *Table 1*. *Yousefi-Ramandi* (2012) illustrated that longer SPI time scales have stronger relationships with variations in reservoir water levels, groundwater storage, and surface flow, hence, being specifically important for basin-scale drought assessments.

Table 1. Classification of drought based on the SPI)

Drought class	SPI values
extremely wet	2 and above
severely wet	1.5 to 1.99
moderately wet	1 to 1.49
normal	-0.99 to 0.99
mild drought	-1 to -1.49
severe drought	-1.5 to -1.99
extreme drought	-2 and below

2.5. Data selection

Given the relevance of the record length of the precipitation for the time-series analyses, especially for trend detection and forecasting rainfall, as well as analyzing drought, this study has used monthly precipitation data from five stations with longer historical records in Qazvin Province. First, a common baseline period across all the stations was defined. Then, the quality control procedures involved the reconstruction of the missing data, removing outliers, and homogeneity and trend analysis within the dataset.

2.6. Assessment of climate model uncertainty

In simulations of climate, not all factors affecting a variable can be represented in a model, an approximation that inevitably introduces errors or uncertainties. The identification and quantification of these uncertainties are paramount in any assessment of model prediction reliability. A probabilistic model is considered appropriate if it can reproduce an accurate distribution with an acceptable level of certainty. The certainty of a distribution is commonly assessed by the width of the prediction interval. In the present study, model uncertainty was estimated using 95% confidence intervals. Model predictions, which were calculated from outputs using the posterior probability density function of parameters, excluded the most extreme 2.5% values at both ends as outliers. The resulting values determined the 95% confidence range, which was considered to reflect the model prediction uncertainty. With the objective of assessing overall model performance and uncertainty, a combined metric called the Uncertainty Performance Index (UPI) was used. This index combines two coefficients: P, representing the percentage of predicted data falling within the 95% confidence interval, and R, a normalized thickness factor of the confidence range. A higher value of UPI corresponds to better model reliability and less uncertainty, reflecting more desirable predictive performance

$$NUE_{CI} = \frac{P_{CI}}{R_{CI}}, \tag{1}$$

where NUE_{CI} denotes the normalized uncertainty performance, P_{CI} represents the percentage of predicted data (P) falling within the confidence interval (CI), and R_{CI} indicates the normalized thickness factor of the confidence interval (CI).

3. Results and discussion

3.1. Impacts of climate change on precipitation, temperature, and reference evapotranspiration

Fig. 2 shows the simulated precipitation, temperature, and reference evapotranspiration at Qazvin station (used here as representative) against observed values in the validation period (2009–2014). Because the daily precipitation is not normally distributed, a fourth-root transformation was applied in order to increase the fitness of the model. *Fig. 2a* shows the observed and simulated monthly precipitation patterns in the validation period. As with any kind of accumulation data, precipitation inherently bears high variability, discrete behavior, and a skewed distribution. Notwithstanding this natural heterogeneity, the overall annual precipitation pattern was successfully replicated with satisfactory accuracy by the model. From March to May, the peak precipitation occurs, and the pattern of this was well captured. In addition, the value of precipitation in July and August was correctly simulated around zero, which is reasonable in the semiarid region with dry summers. There is some mismatch between the observed and simulated precipitation in some months, particularly in March and April, due to its extreme and nonlinear nature. The fourth-root transformation reduced dispersion and aligned the simulated and observed data reasonably well. Given that one of the most challenging variables to simulate is precipitation, the capability to reproduce its seasonal pattern indicates the reliability of the model in studying the impacts of climate change on precipitation and drought of the region.

The successful simulation of monthly and annual precipitation patterns in Qazvin aligns with findings from other studies in semi-arid regions, demonstrating that statistical downscaling approaches, such as the Statistical Downscaling Model (SDSM), can effectively capture seasonal variability despite the high variability and non-normal distribution of rainfall (*Wilby et al*., 2012). Similar results were reported by *Tabari et al.* (2021), who found that SDSM accurately reproduced precipitation patterns in semi-arid regions and outperformed some other downscaling approaches in capturing extreme events. In addition, *Woyessa* (2024) highlighted that SDSM is particularly suitable for semi-arid basins due to its flexibility in predictor selection and rigorous quality control. The minor discrepancies observed in March and April are consistent with the inherent challenges in simulating extreme and nonlinear precipitation events, as noted in previous studies (*Rezaei et al*., 2014; *Ahmadalipour et al*., 2017). Overall, these comparisons with existing literature confirm the reliability of SDSM for assessing climate change impacts on precipitation and drought in the Qazvin region.

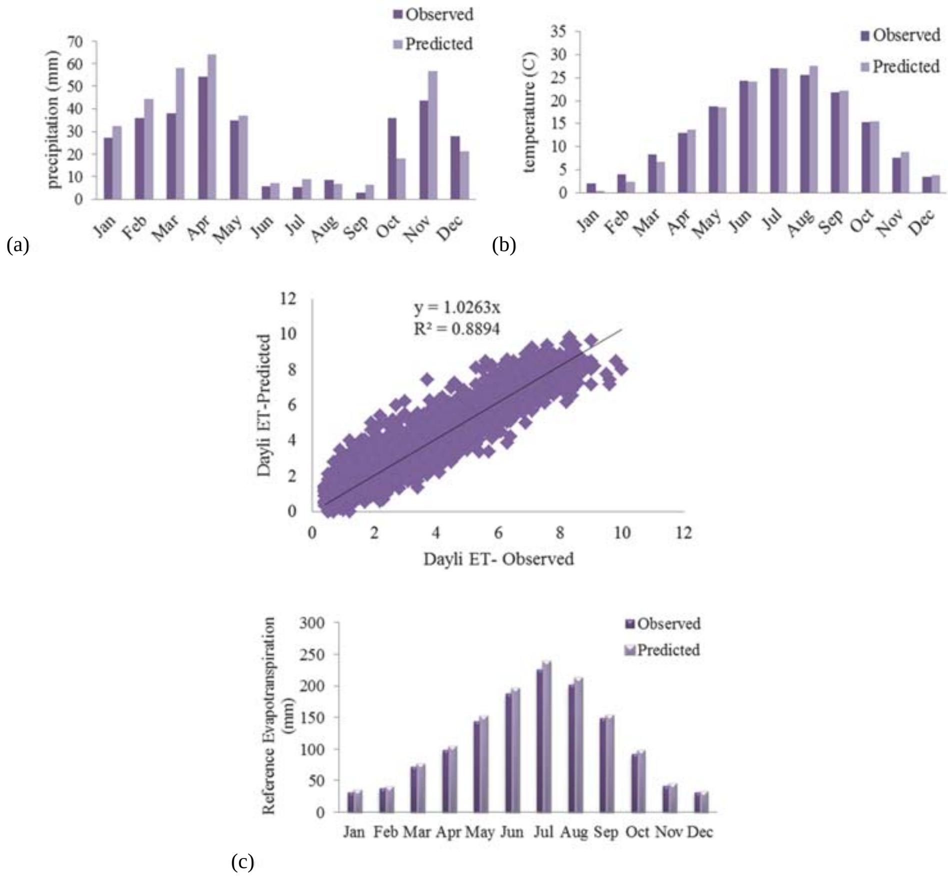

Fig.2. Monthly mean observed values compared with simulated values at Qazvin Meteorological Station for the validation period (2009–2014): (a) precipitation, (b) temperature, and (c) reference evapotranspiration (*ET_0*).

3.2. Temperature and reference evapotranspiration

Fig. 2b shows the observed and simulated monthly temperature patterns for the Qazvin station during the validation period (2009–2014). As can be seen, the model satisfactorily simulated the annual trend of temperature increas e –from the end of January up to the peak of summer (July and August) – and then its decline at the end of the year. The maximum temperatures of both datasets occurred during July and August, with an approximate value of 30 °C, and the minimum temperature occurred during December and January. The differences between the observed and simulated values varied usually from 1 to 2 °C, indicating a good fitness of the model. In fact, temperature is one of the most stable climatic variables; therefore, such high performance by the model is expected. This accurate representation signifies that the model is reliable enough for future scenario analyses, investigating temperature changes, and assessing their impacts on evapotranspiration and drought indices. *Fig. 2c.* shows the monthly variations of the simulated versus the observed reference evapotranspiration, ET_0. The model simulated the monthly pattern of ET_0 with a very high accuracy. The pattern starts growing from February and March toward the warm months to reach its peak in July and August at about 250–280 mm and fits well with the climatic behavior of the region. Considering that ET_0 is primarily driven by temperature, solar radiation, wind speed, and relative humidity, all of which are satisfactorily generated by the model, the close agreement between the observed and the simulated ET_0 is expected. Small discrepancies (less than 5%) are mostly related to short-term fluctuations in relative humidity and wind variations, which might not fully be grasped by the model. In any case, high accuracy in ET_0 is an important added value since ET_0 is a key variable in estimating crop water requirements, water balance studies, and agricultural drought modeling. Thus, this model would be highly applicable for climate change scenario analyses.

The SDSM model accurately reproduced the annual temperature pattern in Qazvin, with differences of only 1–2 °C and a summer peak around 30 °C, reflecting the inherent stability of temperature. Similar performance has been reported in other semi-arid regions. For instance, in the Vu Gia Thu Bon Basin, Vietnam, SDSM captured seasonal patterns and extremes well, with NSE > 0.8 and projected maximum and minimum increases of 2.67–3.9 °C and 1.24–1.96 °C under RCP8.5, respectively (*Phuong et al.*, 2020). In the Jhelum Basin, Himalaya, SDSM simulated daily maximum and minimum temperatures with low MAE and RMSE (KGE = 0.67–0.71), reproducing predicted warming of 2.37–4.66 °C (max) and 2.47–4.52 °C (min) under RCP4.5/8.5 and seasonal patterns including stronger winter and pre-monsoon warming. (*Munawar et al.*, 2022). These comparisons confirm that SDSM consistently reproduces seasonal temperature patterns and extremes in semi-arid regions, with accuracy comparable to that observed in Qazvin.

3.3. Evaluation of distribution and median differences

Non-parametric tests, such as the K-S and Wilcoxon tests, were carried out to investigate the distribution and median differences between observed and simulated data. The test results for these three climatic variables, as tabulated in *Table 2*, reveal that all the KS test statistics are below the critical value of 0.665. Also, based on the P-value obtained from the Wilcoxon test, all are above the 0.05 significant level. Thus, both tests state that no significant difference exists between historical observations and model-generated data during the validation period. These results indicate that the model's predictions are reliable and acceptable.

Table 2. Results of the Wilcoxon and Kolmogorov-Smirnov non-parametric tests for simulated temperature, precipitation, and reference evapotranspiration (*ET_o*) at a 0.05 significance level

Statistical parameter	**Precipitation**	**Temperature**	**Reference evapotranspiration**
Wilcoxon (Pvalue)	1.0	0.724	0.84
Kolmogorov-Smirnov	0.083	0.25	0.166

For model validation and a more detailed assessment of simulation errors, the statistical metrics including mean absolute error (MAE), root mean square error (RMSE), Nash–Sutcliffe efficiency (NSE), and the coefficient of determination (R^2) were employed. The results are presented in *Table 3*.

Table 3. Comparison of simulated precipitation and reference evapotranspiration (*ET_o*) with observed values during the validation period (2009–2014)

Statistical parameter	**Temperature (°C)**	**Precipitation (mm/month)**	**Reference evapotranspiration (mm/month)**
MAE	0.84	7.80	5.40
RMSE	1.10	9.90	6.40
R^2	0.90	0.81	0.90
NSE	0.98	0.63	0.99

The results show satisfactory performances of the model in the simulation of precipitation, *ET_o*, and temperature. Regarding this, the MAE values for *ET_o*, precipitation, and temperature were found to be 5.46 mm, 7.8 mm, and 0.84 °C, respectively, indicating relatively low errors at the monthly scale. The RMSE was 6.4 mm for *ET_o*, 9.9 mm for precipitation, and 1.1 °C for temperature, confirming these findings on the goodness of the simulations. The R^2 was 0.9 for *ET_o* and temperature and 0.81 for precipitation, showing good agreement between simulated and observed values. Also, the NSE values were 0.99 for *ET_o*, 0.98 for temperature, and 0.63 for precipitation. This shows a high model skill regarding the reproduction of *ET_o* and temperature trends and medium accuracy for precipitation. In general, the validation results indicated that the model provides a reliable and robust representation of hydrological processes of the region and is suitable for further scenario analyses.

3.4. Analysis of annual temperature and precipitation trends in Qazvin using the Mann–Kendall test and Sen's slope

3.4.1. Temperature

In order to investigate the trends of annual mean temperature in Qazvin, the Mann-Kendall test and Sen's slope were used, as shown in *Table 4*. It can be seen from the results that there is a significant increasing trend in annual mean temperature during the period 1993–2060 in all three SSP scenarios, namely SSP126, SSP245, and SSP585. The slope was found to be steeper under SSP585, reflecting strong warming under high greenhouse gas emission conditions. This indicates that, over time and with increased greenhouse gas concentrations, the mean temperature is projected to increase gradually and at significant rates. During the baseline period, from 1993 to 2014, there was a slight increase in temperature; however, it was not significant because of the relatively short period and thus smaller natural variability. In general, these results clearly confirm the warming trend in Qazvin for the future climate scenarios and emphasize the fact that the magnitude of temperature increases would be more pronounced under higher emission pathways.

These findings are consistent with numerous studies conducted in semi-arid and arid regions, which have reported significant upward trends in annual mean temperature using non-parametric trend detection methods such as the Mann–Kendall test and Sen's slope estimator. For example, *Ahmadalipour et al*. (2017)1 identified significant warming trends across dry regions using climate model projections, with stronger slopes under high-emission scenarios. Similarly, *Manohar et al.* (2018) reported increasing temperature trends in semi-arid regions, emphasizing that temperature rise intensifies hydrological stress and alters water balance components. Overall, the agreement between the present results and previous studies confirms the robustness of the detected warming trend in Qazvin and reinforces the conclusion that future temperature increases will be more pronounced under higher emission scenarios, with important implications for evapotranspiration enhancement and drought intensification.

Table 4. Mann-Kendall test results and Sen's slope for the annual mean temperature of Qazvin

Statistical period	**Scenario**	**P-value**	**Z**	**Trend slope**
1993–2060	SSP126	*0.0001	3.7	0.008
	SSP245	*0.0001	3.6	0.008
	SSP585	*0.0000	4.5	0.009
1993–2014	baseline period	0.0900	1.2	0.030

* Significant at the 5% level

Fig. 4. illustrates the modeled monthly average temperatures under the considered scenarios for 2015–2060 with respect to the baseline period, which is representing the available data from 1993 to 2014 for each station. All the modelled scenarios indicated that the minimum temperature increase among the study stations will be about 0.5 °C until 2060. The greatest rises in temperature will occur during the warm months, and the maximum increase concerning the baseline will happen in August and will be over 1.2 °C.

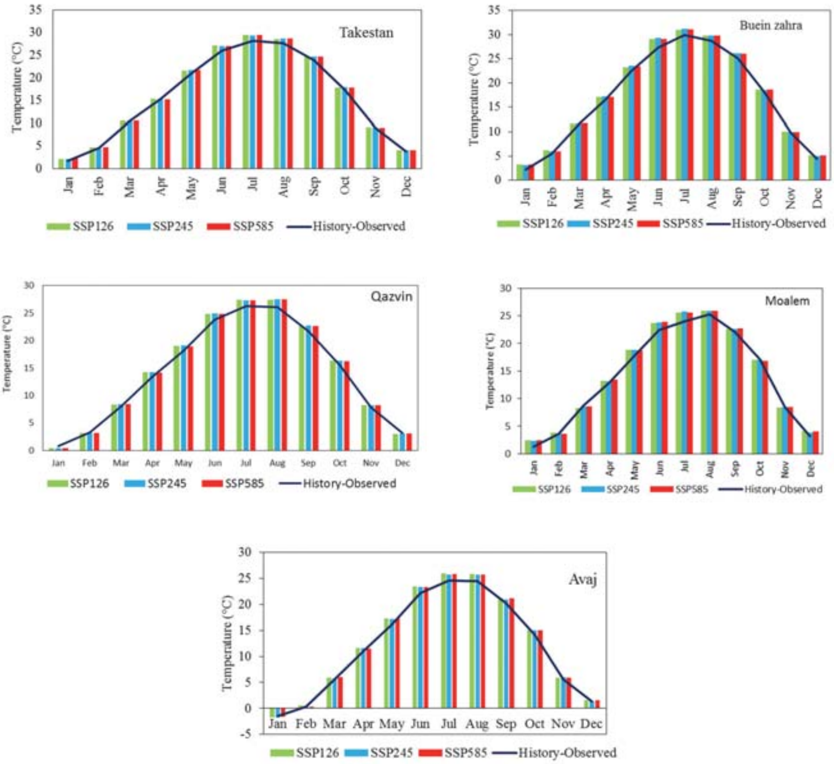

Fig. 4. Trends of monthly mean temperature under the studied scenarios in the future climate compared to the baseline period.

3.4.2. Precipitation

The results show that in all three scenarios, SSP126, SSP245, and SSP585, there is no statistically significant trend at the 5% level of significance during the period 2015–2062. In other words, the future annual precipitation under these scenarios does not appear to increase or decrease clearly, with no definite projection of precipitation change available. Similarly to this, precipitation also varies insignificantly during the baseline period, thus depicting that on a shorter timescale, annual precipitation remained fairly stable, and natural interannual variability may be more dominant than the long-term trend. Therefore, unlike mean temperature showing a clear upward trend, annual precipitation does not exhibit substantial or consistent changes in the future. This may impose potential risks for water resource management due to the fact that random fluctuations in precipitation could impact agriculture and water availability without providing any reliable long-term trend. The results are presented in *Table 5*.

Table 5. Mann-Kendall test results for annual mean precipitation data

Statistical period	Scenario	P-value	Z
2015–2062	SSP126	0.7	-0.60
	SSP245	0.1	0.90
	SSP585	0.5	-0.02
1993–2014	baseline period	0.7	-0.50

* Significant at the 5% level

Fig. 5 presents the projected change in precipitation values for the three scenarios (SSP126, SSP245, and SSP585) with respect to the baseline period. Overall, all three scenarios show a general expected decrease in mean precipitation when compared to the baseline; however, as indicated above, this decrease is not statistically significant. More importantly, the projected increase in precipitation over February and March from the baseline indicates that during these months (late winter), most crops within the region may have their requirements substantially satisfied with the present precipitation levels.

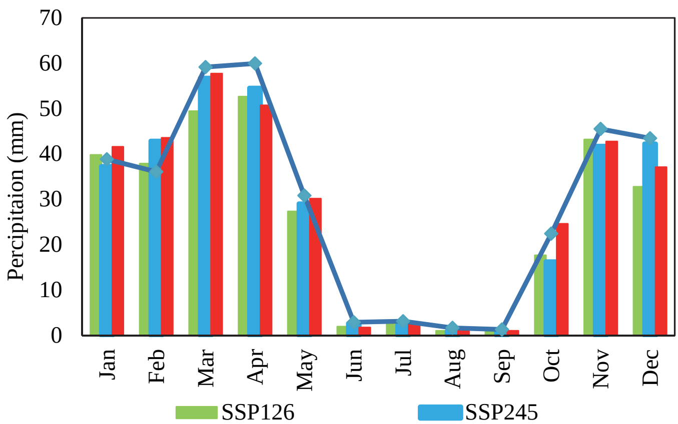

Fig. 5. Trends of mean monthly total precipitation at Qazvin station for 2015–2062 under the studied scenarios compared to the baseline period (1993–2014).

The simulated annual precipitation based on the outputs of the studied scenarios for the years 2020 to 2062 is presented in *Fig. 6*.

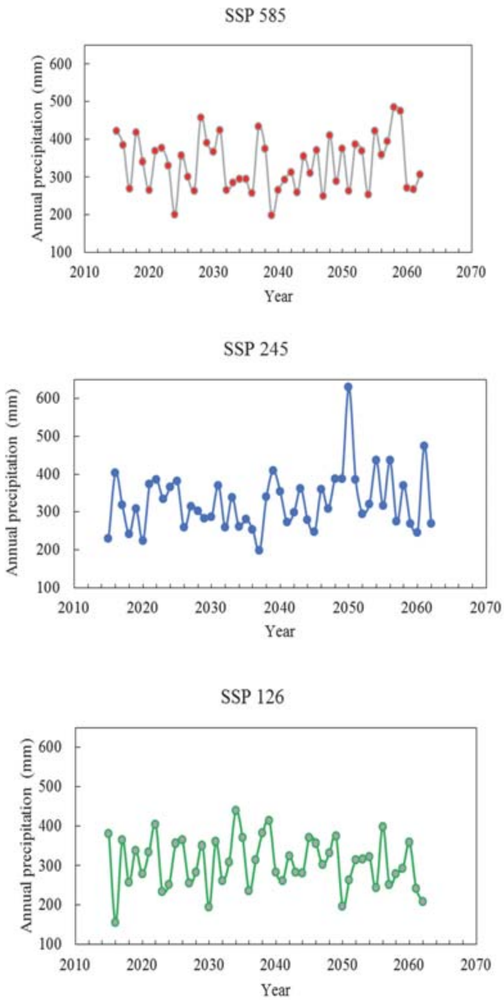

Fig. 6. Simulated annual total precipitation for the period 2015–2062 based on the Sixth Assessment Report climate scenarios.

3.5. Comparison of SSP scenario predictions with observed temperature and precipitation in Qazvin (2015–2020)

As the simulation of climate model scenarios started in 2015, the simulated results were compared with observational data for the period 2015–2020 when both datasets were available to examine the accuracy of models. Based on the different statistical indicators provided in *Table 6*, the temperature simulations with the highest accordance are with the predictions of the SSP245 scenario. The SSP245 is a moderate-to-high radiative forcing pathway with medium future CO_2 emissions, and based on that pathway, the temperature is expected to increase by about 4°C by 2100. According to error and performance indices, MAE, RMSE, NSE, and R^2 for SSP245 are better than for the other scenarios. Also, according to the P-value of the Wilcoxon test, which is close to 1 (0.96), there is no significant difference between simulated and observed data in this short period. The results of the Kolmogorov-Smirnov test are below the critical value for all three scenarios and confirm that the distribution of simulated data does not significantly deviate from the observed one. Accordingly, this analysis shows that for the short-term period 2015–2020, the SSP245 climate scenario has given the best temperature prediction. The model has been able to reproduce annual temperature variability in Qazvin. Thus, this confirms that it is suitable for long-term temperature trend analysis and for the evaluation of different future climate scenarios.

Table 6. Comparison of simulated temperature values under the studied scenarios with observed temperatures for the period 2015–2020

Temperature	**SSP126**	**SSP245**	**SSP585**
MAE	0.92	0.81	0.98
RMSE	1.08	1.02	1.11
NSE	0.99	0.99	0.98
R^2	0.98	0.99	0.98
Wilcoxon (P-value)	0.74	0.96	0.50
Kolmogorov-Smirnov	< critical value	< critical value	< critical value

Previous studies consistently highlight the suitability of intermediate emission scenarios such as SSP245 (or RCP4.5) for long-term temperature analysis. In Morocco, RCP4.5 projections for 2025–2100 indicated an average warming of about 1.78 °C, with short-term validation confirming model reliability for climate adaptation planning (*Kalita et al*., 2023). In the Himalayan region, RCP4.5 successfully captured pronounced winter warming (~2.47 °C) with high validation performance, supporting its use in long-term hydrological impact assessments (*Munawar et al*., 2022). Similarly, studies in India reported that SSP4.5-based simulations reproduced temperature-driven runoff reductions up to 2050 with high agreement to observations, demonstrating its robustness for evaluating future water-stress conditions. Collectively, these findings suggest that

SSP245 provides a balanced and realistic framework for climate impact assessments in semi-arid regions such as Qazvin (*Abed*, 2021).

Amongst the statistical indicators in *Table 7*, the observed precipitation in the period of 2015–2020 had the highest agreement with simulated values of the SSP126 scenario. The SSP126 pathway includes a low radiative forcing pathway that is supposed to provide an approximate value of radiative forcing at 2.6 W/m² by 2100. The projections under this pathway showed that the mean annual precipitation in the Qazvin province might decrease by at least 10% at the end of 2062 compared to the base period. Further confirmation of the model accuracy indices shows that SSP126 has lower MAE and RMSE values than the other scenarios. Its R2 and NSE values also stand at 0.90, showing the high accuracy of the model in reproducing precipitation data. The results of the Wilcoxon and Kolmogorov-Smirnov tests do not indicate a statistically significant difference between simulated and observed values. Therefore, such results confirm that for the short-term period of 2015–2020, the SSP126 scenario can provide the most reliable precipitation predictions, and the model will be able to reproduce the annual variations in Qazvin precipitation in an acceptable mode. Such findings also highlight a probable reduction in the mean precipitation in the future and emphasize the need to apply proactive water resources planning in response to climate change.

Table 7. Comparison of simulated precipitation values under the studied scenarios with observed precipitation for the period 2015–2020

Precipitation	**SSP126**	**SSP245**	**SSP585**
MAE	4.80	9.52	10.22
RMSE	6.39	13.77	15.91
NSE	0.90	0.52	0.36
R^2	0.90	0.59	0.62
Wilcoxon (P-value)	0.30	0.72	0.50
Kolmogorov-Smirnov	< critical value	< critical value	< critical value

3.6. Spatial analysis of climate change scenarios

In this section, precipitation and temperature changes of the studied future period, 2020–2060, relative to the baseline period, 1993–2020, were estimated and analyzed using spatial interpolation methods. The maps were prepared according to the annual averages of the statistical periods to illustrate clearly the spatial variability of precipitation and temperature. The results showed that under future climate conditions, the minimum precipitation across the province will be reduced. As discussed in the previous section, Qazvin's precipitation pattern is in the best agreement with the SSP126 scenario predictions. Therefore, the spatial mapping of precipitation changes was performed based on SSP126 with respect to the baseline period. It was observed that precipitation will be reduced over most areas of the province. The reduction is at its maximum in the southeastern area. This region will also witness more intensive drought conditions (*Fig. 7*).

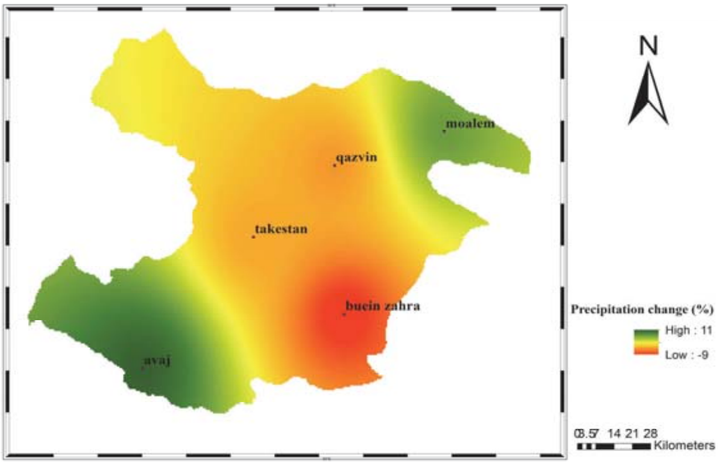

Fig. 7. Predicted precipitation changes under the SSP126 scenario for the future climate compared to the baseline period.

Spatial analysis of annual average temperature also shows that in both the baseline period and future climate conditions, the maximum temperatures occur in the Bouin-Zahra area. Moreover, the higher projected temperature rise in future climate conditions relative to other parts of the province underlines the fact that this area will be a focal point of warming. In general, the spatial analysis results imply that the climate of Qazvin Province in the future will be characterized by lower precipitation and higher temperatures. The identified point confirms that water resources management and climate change adaptation plans are required to focus with more attention and emphasis on the southeastern parts of the province and on the Bouin-Zahra area, due to the intensity of changes over these areas. *Fig. 8* presents the spatial distribution of annual average temperatures corresponding to the baseline period and to the studied scenarios for the future climate conditions. From this figure, it is clear that the highest temperatures for Qazvin Province occur over the Bouin-Zahra area during both the base period and under future climate conditions, with the highest rate of warming projected over this area.

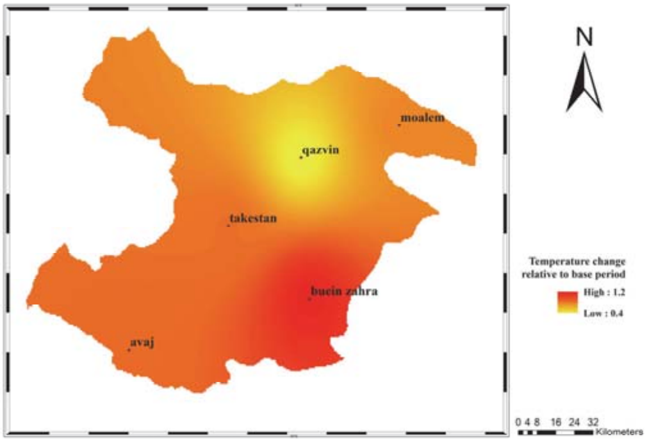

Fig. 8. Changes in annual mean temperature under the SSP245 scenario for the future climate compared to the baseline period mean temperature.

The spatial distribution of daily reference evapotranspiration (*ET₀*) during the baseline period and the future period under SSP126, SSP245, and SSP585 scenarios is presented in *Fig. 9*. The highest *ET₀* values during the baseline period were observed in Bouin-Zahra and Takestan, and this pattern persists under future climate conditions. However, reference evapotranspiration also increases in other regions of the province, which can be attributed to the projected rise in temperature.

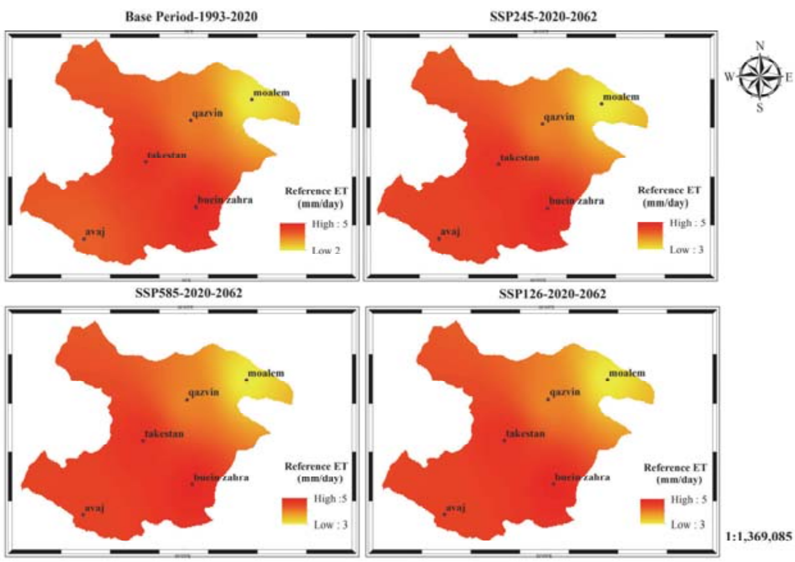

Fig. 9. Spatial distribution of daily mean reference evapotranspiration for the baseline period and future climate (2020–2062) under the studied scenarios.

3.7. Assessment of uncertainty in climate models

The analysis of the simulation results showed that temperature projections under the SSP245 scenario have the lowest uncertainty compared with other scenarios. As noted earlier, the statistical indices also confirmed that this scenario has the least error in the estimation of temperature, meaning it will provide more reliable temperature predictions. Contrarily, the simulated precipitation under the SSP126 scenario has the least uncertainty among all scenarios, and statistical indices confirm this scenario produces the most accurate precipitation estimates. Overall, the comparison indicates that uncertainty in precipitation projections is higher than for temperature, probably due to the more stochastic nature and higher variability over both short and long timescales.

3.8. Spatial analysis of drought under climate change conditions

Previous studies conducted in Qazvin Province have indicated that SPI has better spatial correlation compared to other indices for drought mapping. *Moradi* (2012) and *Naserzadeh et al.* (2012) had focused on this issue. Thus, SPI was adopted for the purpose of drought analysis in this study. It is worth stating here that the SPI at 12 months is quite appropriate for reflecting groundwater storage and river flows and is actually an effective indicator for hydrological drought. SPI analysis in recent years (from 2021 onward) indicates severe drought in this region. According to model outputs, the water resources in the province face critical conditions. Since meteorological and agricultural droughts usually precede hydrological droughts, a notable reduction in soil moisture has been recorded, raising vulnerability for rainfed agriculture. This accentuates the urgent need for sustainable water resource management policies and sharpened sensitivity in the implementation of land development projects. *Table 8* shows the drought and wet year frequency of each station for the study period. On average, the frequency of dry and wet years is almost equal (44.5% and 45.8%, respectively). In other words, hydrological drought and wet situations are almost in balance, but this condition reflects the vulnerability of the province's water resources because the natural system has limited capability for recovery against water scarcity. These results again highlight the necessity of implementing strict and sustainable policies to conserve and develop both surface and groundwater resources within Qazvin Province. Previous studies in Qazvin Province have shown that the standardized precipitation index (SPI) provides stronger spatial coherence for drought mapping compared to other indices, supporting its selection in this study (*Asgari et al.*, 2014). In particular, SPI at a 12-month time scale is widely recognized as an effective indicator of hydrological drought, as it reflects long-term precipitation deficits affecting groundwater storage and river flows. Similar applications of SPI-12 in semi-arid regions have demonstrated its reliability for identifying hydrological drought dynamics.

Table 8. Frequency (%) of drought and wet years at the stations during the study period based on the 12-month SPI (SPI-12)

Station	Statistical Period	Drought frequency (%)	Wet period frequency (%)
		SPI>0	SPI<0
Avaj	1997-2022	46.1	45.8
Buin Zahra	2006-2022	40.5	46.8
Moallem Kalaye	2002-2022	41.6	48.8
Qazvin	1993-2022	46.9	45.0
Takestan	2004-2022	47.3	43.0

The SPI for 2023–2062, according to the outputs of the AR6 climate scenarios, is shown for Qazvin Station (as an example) in *Fig. 10*. It shows that, under the SSP126 scenario, drought conditions remain until the end of 2025, followed by a period of moderate wet conditions. For the SSP585 scenario, the recent drought has continued until the end of 2027 and is then followed by a normal period. Under the SSP245 scenario, a normal period starts at the end of 2023 and continues until early 2026; after this, a moderate drought occurs until 2027. Spatially summarizing these results, *Fig. 11* presents the mapping of the 12-month average SPI under the studied scenarios for the next decade (2024-2034). This map outlines the expected spatial patterns of drought and wet conditions across the province.

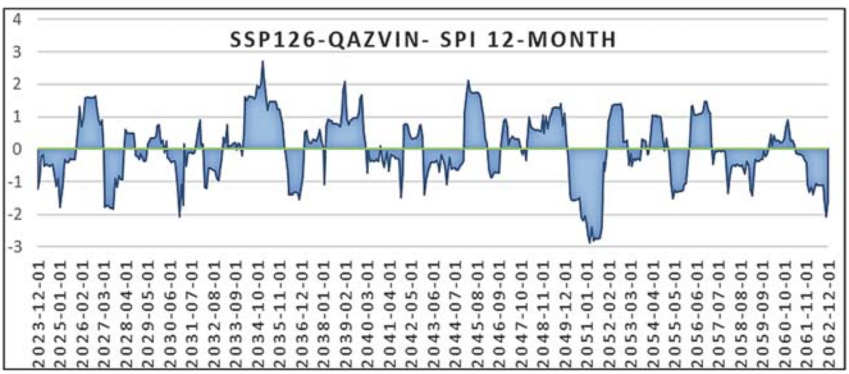

Fig.10. SPI-12 values for Qazvin station for the future period 2024–2062, based on CMIP6 scenario outputs.

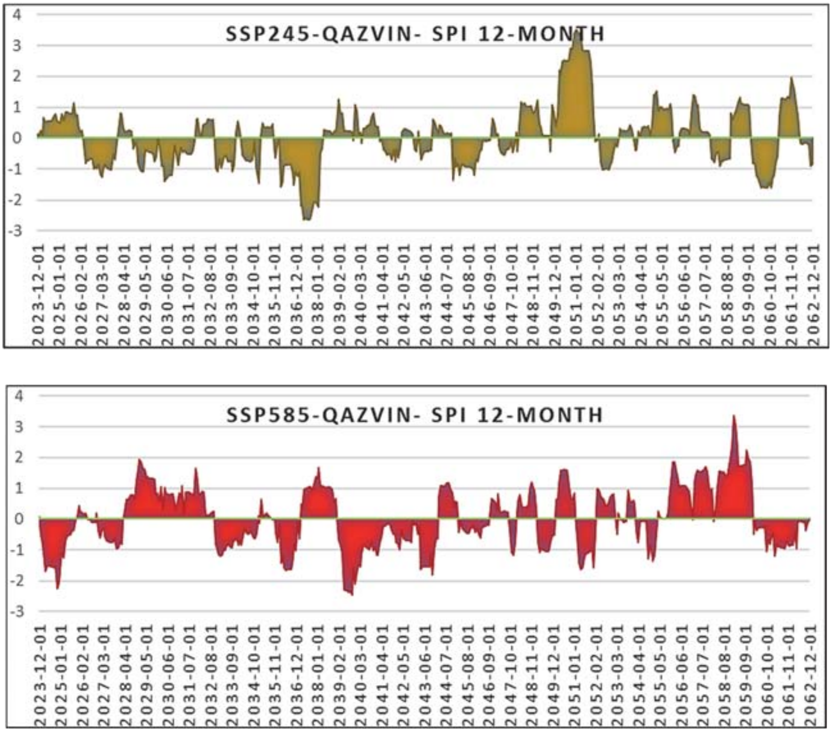

Fig. 10. Continued

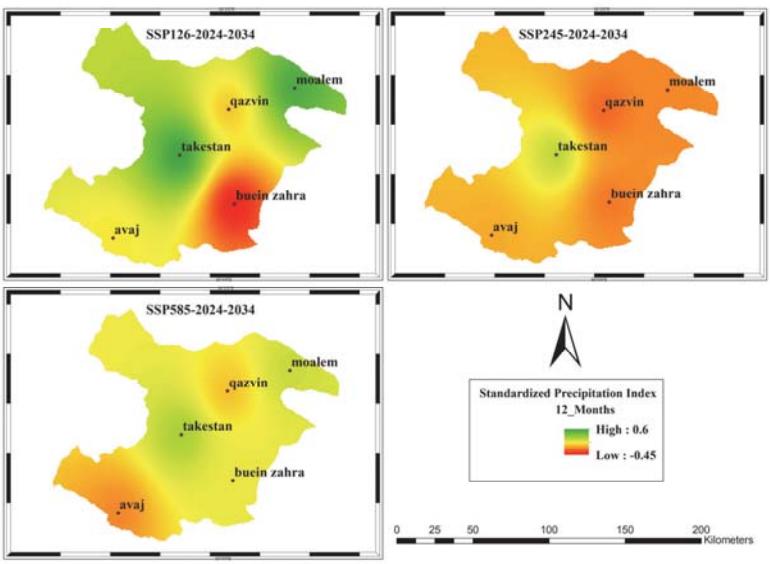

Fig. 11. Spatial distribution of the annual average SPI-12 values in Qazvin Province for the future climate based on SSP126, SSP245, and SSP585 scenario outputs (2024–2034)

4. Conclusion

According to the findings of this study, Qazvin Province is likely to experience a gradual and significant increase in temperature, along with a relative decrease in precipitation during the course of future climate change. Across all SSP scenarios (SSP126, SSP245, and SSP585), annual mean temperatures are trending upwards, especially under SSP585, which reflects a stronger warming under high greenhouse gas emissions. In contrast, changes in annual precipitation are not statistically significant, although it is possible to experience a reduction of approximately 10% in average precipitation. Based on a spatial analysis of the changes, it appears that the southeastern sector of the province and the Bou'in-Zahra region will be most affected by the reduced precipitation and the concentrated warming. Evapotranspiration is anticipated to increase across all areas, increasing the demands on water resources. Rainfed agriculture is at risk due to the 12-month standardized precipitation index's (SPI) severe drought events and alternating periods of drought and wet conditions, highlighting the vulnerability of surface and groundwater resources. In light of hydrological variability, forecasting precipitation is more uncertain than forecasting temperature, which highlights the importance of flexible planning and risk management.

These findings suggest the following measures for reducing vulnerability and enhancing resilience:

- Manage water resources sustainably by increasing the storage capacity of surface and groundwater, reducing water losses, and allocating water efficiently for agricultural and domestic uses.
- Promote climate-smart agriculture, cultivate low-water-use crops, and reduce the reliance on rainfed agriculture in vulnerable areas.
- Planning focused on adaptation and water resource management for the southeastern region and Bou'in-Zahra, which are expected to be most impacted by climate change.
- Maintain continuous monitoring and assessment by utilizing climate prediction models and drought indices for the purpose of periodically updating policies and programs related to water and agriculture.
- To enhance socioeconomic resilience, farmers and water users need to be trained in order to mitigate the economic and social impacts of droughts and climate change.

By implementing these measures, the province can increase its resilience to future droughts, increase its sustainability in agricultural production, alleviate pressure on water resources, and enhance its ability to adapt to climate change.

References

Abed, S. S., 2021: Future climate projections in Algeria using statistical downscaling model. *Research Square 1-29*. https://doi.org/10.21203/rs.3.rs-627355/v1

Ahmadalipour, A., Moradkhani, H., and *Svoboda, M.,* 2017: Centennial drought outlook over the CONUS using NASA-NEX downscaled climate ensemble. *International Journal of Climatology 37(5),* 2477-2491. https://doi.org/10.1002/joc.4859

Asgari, H., Mohsenipour, M., Shahid, S., Hadipour, S., Shafieifar, M., and *Roushenas, P.,* 2014: Spatio-temporal characteristics of droughts and drought trends in Qazvin Province of Iran. *Research Journal of Applied Sciences, Engineering and Technology 8(11),*1299-1311. https://doi.org/10.19026/rjaset.8.1100

Dafouf, S., Lahrach, A., Tabyaoui, H., and *Benaabidate, L.,* 2025: Future Evolutions of Precipitation and Temperature Using the Statistical Downscaling Model (SDSM), Case of the Guir and the Ziz Watershed, Morocco. *Earth. 6(1),*4. https://doi.org/10.3390/earth6010004

Dai, A., 2011: Characteristics and trends in various forms of the Palmer Drought Severity Index during 1900–2008. *Journal of Geophysical Research: Atmospheres. 116(12)* https://doi.org/10.1029/2010JD015541

Daneshvar, M. R. M., Ebrahimi, M., and *Nejadsoleymani, H.,* 2019: An overview of climate change in Iran: Facts and statistics. *Environmental Systems Research, 8(1),* 1–10. https://doi.org/10.1186/s40068-019-0135-3

Dehghanisanij, H., Kanani, E., and *Akhavan, S.,* 2020: Evapotranspiration and components of corn (Zea mays L.) under micro-irrigation systems in a semi-arid environment. *Spanish Journal of Agricultural Research, 18,* e1202. https://doi.org/10.5424/sjar/2020182-16814

Gholami, V., Jolandan, M. A., and *Torkaman, J.,* 2017: Evaluation of climate change in northern Iran during the last four centuries using dendroclimatology. *Natural Hazards 85(3),* 1835–1850. https://doi.org/10.1007/s11069-016-2667-4

Ghorbani, K., and *Valizadeh, E.* 2014: Studying frost and chilling dates affecting agriculture under climate change (Case study: Mashhad, Tabriz, Qazvin). *Journal of Water and Soil Conservation 21(4),* 197–211. (In Persian)

Kalita, R., Kalita, D., and *Saxena, A.,* 2024: Future projections of precipitation and temperature extremes at Sohra (Cherrapunji) using Statistical Downscaling Model. *Mausam 75(1),* 181-190. https://doi.org/10.54302/mausam.v75i1.6081

Kanani, E., Dehghanisanij, H., and *Akhavan, S.,* 2022: Variation in actual corn (Zea mays L.) evapotranspiration and crop coefficients under different point-source irrigation systems in a semiarid region. *Theoretical and Applied Climatology 148(1),* 303–315. https://doi.org/10.1007/s00704-022-03932-w

Kanani, E., Nazari, B., and *Dehghanisanij, H.,* 2025: A holistic assessment of water resources and management in the Zarrineh River sub-basin using *Water Accounting Plus. Scientific Reports 15,* 11725. https://doi.org/10.1038/s41598-025-XXXX-X

Karimi, V., Karami, E., and *Keshavarz, M.,* 2018: Climate change and agriculture: Impacts and adaptive responses in Iran. *Journal of Integrative Agriculture 17(1),* 1–15. https://doi.org/10.1016/S2095-3119(17)61794-5

Lhotka, O., Kyselý, J., and *Farda, A.,* 2018: Climate change scenarios of heat waves in Central Europe and their uncertainties. *Theoretical and Applied Climatology 131(3),* 1043–1054 https://doi.org/10.1007/s00704-016-2031-3.

Manohar, M. L., Sau, B. L., Jitendra Patidar, J.P., and *Abhishek Patidar, A.,P.,* 2018: Climate change and groundwater: impact, adaptation and sustainable. *International Journal of Bio-resource and Stress Management 9(3):* 408-415. https://doi.org/10.23910/IJBSM/2018.9.3.3C0671b

Mirsane, M., Sohrabi-Molayousef, T., Massah-Bavani, A., and *Bazrafshan, J.,* 2011: Assessment of uncertainties in AOGCM models and climate downscaling methods for simulating crop water requirements: Case study of Qazvin Plain. *In Proceedings of the 4th Iranian Water Resources Management Conference. Tehran.* https://civilica.com/doc/116974

Moradi, S., 2012: Drought monitoring based on precipitation-based indices in Qazvin Province (Master's thesis). *Faculty of Humanities, University of Zanjan, Zanjan, Iran.* (In Persian)

Munawar, S., Rahman, G., Moazzam, M. F. U., Miandad, M., Ullah, K., Al-Ansari, N., and *Linh, N. T. T.,* 2022: Future climate projections using SDSM and LARS-WG downscaling methods for CMIP5 GCMs over the transboundary Jhelum River Basin of the Himalayas Region. *Atmosphere 13(6),* 898. *https://doi.org/10.3390/atmos13060898*

Naserzadeh, M. H., and *Ahmadi, A.,* 2012: Evaluation of meteorological drought indices for drought assessment and spatial zoning in Qazvin Province. *Applied Researches in Geographical Sciences 12(27),* 141–162. (In Persian)

Nazari, B., Kanani, E., and *Sepehri, S.,* 2023: Assessment of water productivity improvement strategies using a system dynamics approach*. Applied Water Science 13(12),* 240. https://doi.org/10.1007/s13201-023-02044-8

Nazari, B., Kanani, E., and *Sepehri, S.,* 2024: A new perspective in assessing real water saving resulting from irrigation technology interventions. *Journal of Water Resources Planning and Management 150(9),* 04024033. https://doi.org/10.1061/JWRMD5.WRENG-6479.

Phuong, D. N. D., Duong, T. Q., Liem, N. D., Tram, V. N. Q., Cuong, D. K., and *Loi, N. K.,* 2020: Projections of future climate change in the Vu Gia Thu Bon River Basin, Vietnam by using statistical downscaling model (SDSM). *Water 12(3),* 755. https://doi.org/10.3390/w12030755

Rajsekhar, D., Singh,V. P., and *Mishra, A. K.,* 2015:Integrated drought causality, hazard, and vulnerability assessment for future socioeconomic scenarios: An information theory perspective*. J. Geophys. Res. Atmos. 120,* 6346–6378. https://doi.org/10.1002/2014JD022670.

Rasmussen, R., Ikeda, K., Liu, C., Gochis, G., Clark, M., Dai, A., Gutmann, E., Dudhia, J., Chen, F., Barlage, M., Yates, D., and *Zhang, G.,* 2014: Climate change impacts on the water balance of the Colorado headwaters: High-resolution regional climate model simulations*. Journal of Hydrometeorology (13),* 1091-1116. https://doi.org/10.1175/JHM-D-13-0118.1

Rezaei, M., Nohtani, M., Moghaddamnia, A., Abkar, A., and *Rezaei, M.,* 2014: Performance Evaluation of Statistical Downscaling Model (SDSM) in Forecasting Precipitation in two Arid and Hyper arid Regions. *Water and Soil 28(4),* 836-845. https://doi.org/10.22067/jsw.v0i0.23119

Ruíz Álvarez, M., Gomáriz Castillo, F., and *Alonso Sarría, F*., 2021: Evapotranspiration response to climate change in semi-arid areas: Using random forest as a multi-model ensemble method. *Water 13(2),* 222. https://doi.org/10.3390/w13020222

Sami, S. S., Ali, A. A., and *Jalal, A. D. J.,* 2024: An application of the statistical downscaling model (SDSM) to simulate precipitation data in the Iraqi Western Desert*. AIP Conference Proceedings 3009, No. 1,* 030113*. AIP Publishing LLC*. https://doi.org/10.1063/5.0197996

Tabari, H., Paz, S. M., Buekenhout, D., and *Willems, P.*, 2021: Comparison of statistical downscaling methods for climate change impact analysis on precipitation-driven drought*. Hydrology and Earth System Sciences 25(6),* 3493-3517. https://doi.org/10.5194/hess-25-3493-2021

Terink, W., Immerzeel, W. W., and *Droogers, P.,* 2013: Climate change projections of precipitation and reference evapotranspiration for the Middle East and North Africa until 2050*. International Journal of Climatology 33(14),* 3055-3072. https://doi.org/10.1002/joc.3650

Wilby, R. L., Dawson, C. W., and *Barrow, E. M.,* 2002: SDSM—A decision support tool for the assessment of regional climate change impacts. *Environmental Modelling and Software 17(2),* 147–159. https://doi.org/10.1016/S1364-8152(01)00060-3

Woyessa, Y. E. 2024: Assessment of climate change impact and comparison of downscaling approaches: a case study in a semi-arid river basin*. Proceedings of International Association of Hydrological Sciences 385,* 97-102. https://doi.org/10.5194/piahs-385-97-2024

Xu, Y. P., Pan, S., Fu, G., Tian, Y., and *Zhang, X.*, 2014: Future potential evapotranspiration changes and contribution analysis in Zhejiang Province, East China. *Journal of Geophysical Research: Atmospheres 119(5),* 2174-2192. https://doi.org/10.1002/2013JD021245

Yousefi-Ramandi, R., 2012: Analysis of wet and dry periods in Qazvin Province using drought indices to determine the most appropriate drought indicator (Master's thesis). *Faculty of Geographical Sciences, Kharazmi University, Tehran, Iran.* (In Persian)

Zarrin, A. and *Dadashi-Roudbari, A.,* 2023: Evaluation of CMIP6 models in estimating temperature in Iran with emphasis on equilibrium climate sensitivity (ECS) and transient climate response (TCR). *Iranian Journal of Geophysics 17(1),* 39–56. https://doi.org/10.30499/ijg.2022.344862.1430

INSTRUCTIONS TO AUTHORS OF *IDŐJÁRÁS*

The purpose of the journal is to publish papers in any field of meteorology and atmosphere related scientific areas. These may be

- research papers on new results of scientific investigations,
- critical review articles summarizing the current state of art of a certain topic,
- short contributions dealing with a particular question.

Some issues contain "News" and "Book review", therefore, such contributions are also welcome. The papers must be in American English and should be checked by a native speaker if necessary.

Authors are requested to send their manuscripts to

Editor-in Chief of IDŐJÁRÁS
P.O. Box 38, H-1525 Budapest, Hungary
E-mail: journal.idojaras@met.hu

including all illustrations. MS Word format is preferred in electronic submission. Papers will then be reviewed normally by two independent referees, who remain unidentified for the author(s). The Editor-in-Chief will inform the author(s) whether or not the paper is acceptable for publication, and what modifications, if any, are necessary.

Please, follow the order given below when typing manuscripts.

Title page should consist of the title, the name(s) of the author(s), their affiliation(s) including full postal and e-mail address(es). In case of more than one author, the corresponding author must be identified.

Abstract: should contain the purpose, the applied data and methods as well as the basic conclusion(s) of the paper.

Key-words: must be included (from 5 to 10) to help to classify the topic.

Text: has to be typed in single spacing on an A4 size paper using 14 pt Times New Roman font if possible. Use of S.I. units are expected, and the use of negative exponent is preferred to fractional sign. Mathematical formulae are expected to be as simple as possible and numbered in parentheses at the right margin.

All publications cited in the text should be presented in the *list of references*, arranged in alphabetical order. For an article: name(s) of author(s) in Italics, year, title of article, name of journal, volume, number (the latter two in Italics) and pages. E.g., *Nathan, K.K.,* 1986: A note on the relationship between photo-synthetically active radiation and cloud amount. *Időjárás 90,* 10–13. For a book: name(s) of author(s), year, title of the book (all in Italics except the year), publisher and place of publication. E.g., *Junge, C.E.,* 1963: *Air Chemistry and Radioactivity.* Academic Press, New York and London. Reference in the text should contain the name(s) of the author(s) in Italics and year of publication. E.g., in the case of one author: *Miller* (1989); in the case of two authors: *Gamov* and *Cleveland* (1973); and if there are more than two authors: *Smith et al.* (1990). If the name of the author cannot be fitted into the text: *(Miller,* 1989); etc. When referring papers published in the same year by the same author, letters a, b, c, etc. should follow the year of publication. DOI numbers of references should be provided if applicable.

Tables should be marked by Arabic numbers and printed in separate sheets with their numbers and legends given below them. Avoid too lengthy or complicated tables, or tables duplicating results given in other form in the manuscript (e.g., graphs). *Figures* should also be marked with Arabic numbers and printed in black and white or color (under special arrangement) in separate sheets with their numbers and captions given below them. JPG, TIF, GIF, BMP or PNG formats should be used for electronic artwork submission.

More information for authors is available: journal.idojaras@met.hu

Published by the HungaroMet Hungarian Meteorological Service

Budapest, Hungary

ISSN 0324-6329 (Print)

ISSN 2677-187X (Online)